Alma Mater Studiorum · Università di Bologna

SCUOLA DI SCIENZE
Dipartimento di Fisica e Astronomia
Corso di Laurea in Fisica del Sistema Terra

Comprehensive Investigation of an Arctic Rain On Snow Event: Impacts on the Chemical and Physical Properties of the Seasonal Snowpack in Svalbard

Relatore:
Prof. Federico Porcù

Correlatore:
Dott. Andrea Spolaor

Correlatore:
Dott. Federico Scoto

Presentata da:
Matteo Monzali

Sessione 2023
Anno Accademico 2021/2022

Abstract

The cryosphere is a vital component of the Earth system. It comprehends all the frozen water bodies on our planet, and results crucial when talking about climate and climate change. Polar regions are essential since the phenomenon of polar amplification makes them very sensitive to small changes in global mean air temperature.

One of the most studied polar areas is the Svalbard archipelago, located at around 81 °N. There, the town of Ny-Ålesund hosts many polar research groups, so that many data are available for that specific area.

Rain On Snow (ROS) events are a particular kind of weather event with rain falling over the snowpack during winter months. Their frequency is expected to increase with climate change, but due to their past uncommonness, they are still not well studied. The effects of these events are various as they influence different components of the cryosphere, from the snowpack to the sea ice, but many are still not known or well characterized.

The aim of this work is to collect data from many different sources, to carry out a comprehensive analysis of a ROS event that happened in Ny-Ålesund during March 2022, including its genesis and its consequences. The different sources include data from automatic weather stations, two reanalyses, satellite, and manual samples of the snowpack, so that many aspects of the cryosphere are considered.

The results showed that the air mass originated from the Gulf of Mexico and was transported to Svalbard by a particular geopotential configuration. No significant amount of anthropogenic compounds has been found from the chemical analyses, while remarkable effects both on the snow and sea surface temperature have been noted, as well as an important decrease in the sea ice.

Thanks to these results, aimed research could be undertaken to study specific effects, so that the consequences of ROS events can be well characterized, in the perspective of their increasing frequency in the future.

Abstract

Italian version

La criosfera è una componente vitale del sistema Terra. Comprende tutti i corpi contenenti ghiaccio sul nostro pianeta, e risulta cruciale quando si parla di clima e di cambiamento climatico. Le regioni polari sono essenziali dato che il fenomeno dell'amplificazione polare le rende molto sensibili a piccole variazioni nella temperatura atmosferica globale media.

Una delle aree polari più studiate è l'arcipelago delle Svalbard, situato a circa 81 °N. Lì, la città di Ny-Ålesund ospita molti gruppi di ricerca polare, così che ci sono molti dati disponibili per quell'area.

Gli eventi di pioggia su neve (Rain On Snow, ROS) sono degli eventi particolari dove si ha pioggia che precipita sul manto nevoso nei mesi invernali. Ci si aspetta che la loro frequenza aumenti con i cambiamenti climatici, ma a causa della loro rarità nel passato, non sono ancora ben studiati. Gli effetti di questi eventi sono vari dato che influenzano componenti diverse della criosfera, dal manto nevoso fino al ghiaccio marino, ma diversi di questi effetti non sono ancora conosciuti o comunque ben caratterizzati.

Lo scopo di questa tesi è quello di raccogliere dati da diverse fonti, così da realizzare un'analisi completa della genesi e delle conseguenze di un evento ROS avvenuto a Ny-Ålesund nel Marzo 2022. Le sorgenti di dati includono dati da stazioni meteo automatiche, da due rianalisi meteorologiche, da satellite e da campioni di manto nevoso, così da considerare diversi aspetti della criosfera.

I risultati hanno mostrato che la massa d'aria ha avuto origine nel Golfo del Messico, ed è stata trasportata fino alle isole Svalbard da una particolare configurazione del geopotenziale. Dalle analisi chimiche non è stato trovato un aumento significativo di composti antropogenici, mentre sono stati notati effetti significativi sulla temperatura della neve e della superficie marina, così come un'importante riduzione della concentrazione di ghiaccio marino.

Grazie a questi risultati, si potranno intraprendere ricerche per studiare specifici effetti, così che le conseguenze degli eventi ROS possano essere ben caratterizzate, nella prospettiva che la loro frequenza aumenti nel futuro.

Contents

Chapter 1

Introduction

The cryosphere, that is the component of the Earth's surface containing frozen water, is a vital component of the Earth system. It plays a significant role in shaping several climatic processes by interacting with other components including the atmosphere, the ocean, the biosphere, and the geosphere. Its influence extends beyond its immediate surroundings and has a substantial impact on global climate patterns and sea level rise. Therefore, a better understanding of the cryosphere and its relationship with other Earth system components is essential for predicting and mitigating the effects of climate change.

Some of the cryosphere components, such as sea ice, interact with the ocean, preventing the heat exchange with the lower atmosphere, influencing ocean circulation patterns, and therefore affecting global climate. Moreover sea ice provides a unique habitat for a variety of polar species, including polar bears, seals, or smaller organisms such as bacteria and algae. [1]

The recent climate change, attributable to anthropic activities, mainly combustion of fossil fuels, poses new challenges to the Earth's ecosystem, as well as to the human population. In response to increased carbon dioxide concentrations, major effects of climate changes include an increase in global average temperatures and a modification of the water cycle [2]. Due to the so-called "polar amplification", the effects of climate change are particularly visible in the polar regions and especially in the Arctic [3]. The main proposed reason can be found in a process called *ice-albedo feedback*, that is one of the most important feedback processes in the Earth system, involving the cryosphere and the Earth's radiation budget. As the global temperatures rise due to climate change, ice and snow melt faster eventually exposing lower albedo surfaces such as soil or ocean (whose albedo can be as low as 6%) and the overall polar regions albedo decreases. A lower albedo increases the amount of absorbed radiation and helps in further increasing the atmospheric temperature. Due to this mechanism, the Arctic is now warming almost four times faster than the rest of the world since 1979 [4], making it the first place where the climate change and its effects becomes significantly visible.

These changes have other profound effects in the Arctic regions, including the thawing of permafrost, changes in precipitation patterns, and shifts in the distribution of plant and animal species. A particular kind of event, where rain falls on the snowpack on the winter season, called Rain on Snow event, is becoming more and more common in the Arctic region, due to changes in precipitation patterns and changes in seasonal temperatures.

This thesis aims to contribute to our understanding of one of these events, happened in the Svalbard archipelago in March 2022. By investigating this event in detail and through many different datasets, this work aims to expose underlying driving mechanisms of the event genesis as well as the impacts on the local environment. In this chapter, a detailed framework will be set up, starting with an introduction on the Svalbard archipelago and its climate. Afterwards, informations regarding snow and the snowpack will be presented, as well as informations concerning the arctic meteorology, and lastly introducing two peculiar arctic phenomena, including the Rain on Snow event.

1.1 Svalbard archipelago

Svalbard archipelago is located in the Arctic Ocean and expands from 74° to 81°N, midway between the Norwegian northern coast and the North Pole. It falls under the sovereignty of Norway, but it is considered an incorporated area, meaning that it is governed by an appointed governor designed by the Norwegian government.

The largest island is called Spitsbergen (*pointed mountains* in Dutch), whose major settlements are Longyearbyen and Ny-Ålesund (Figure 1), with the latter completely dedicated to scientific research nowadays. The archipelago was discovered in 1596 by the Dutch explorer Willem Barents, and in a few years they became the favorite destination for hunt expeditions, since walruses and whales were common around the islands. After an intense hunting activity carried by several countries both on land and in sea, by the 1890s the archipelago had become a tourist destination and a first base for the Arctic exploration. Moreover, coal deposits were found, and minings started both from Norwegians and British companies, as in Figure 2.

As the commercial interests started to grow and the competition for the control of the many available goods increased, around 1910 different countries started to claim the Svalbard territory. Finally, after WW1, the Svalbard Treaty was signed, placing the archipelago under the Norway sovereignty, that however allows the other signatory countries to access the islands' goods. After WW2, Ny-Ålesund was established as a research outpost, and slowly the mines all around the islands were abandoned, leaving many ghost cities, such as Pyramiden [6].

Ny-Ålesund (from the city Ålesund, Norway), located on Spitsbergen island, is now a research outpost for many research centers from all over the world, including Italy, that runs the Arctic observatory "Dirigibile Italia", run by CNR-ISP (National

Figure 1: **Map of Svalbard.** The southern island is called Bjørnøya (Bears' island), while the main one, Spitsbergen (pointed mountains), is the one on the left. Longyearbyen and Ny-Ålesund, where the Dirigibile Italia station is located, are indicated with a red dot.

Figure 2: **Transport of coal from the mine to the harbour.** Picture dated 1926-1933, taken by Walter Göpfer and donated to the Svalbard Museum [5].

Council of Research - Institute of Polar Science).

The station was opened in 1997 and is an essential infrastructure for the Italian polar research, as well as the international polar research, as it is involved in many international researches [7].

Svalbard climate and geography

Being Svalbard an archipelago located at high latitudes, the overall climate is mainly polar, although it is also influenced by the warm West Spitsbergen Current, the northernmost branch of the North Atlantic Current (NAC), whose effects are mainly visible on the southern and western coasts. Thanks to the NAC, winter temperatures are quite mild, up to 20 °C higher than other locations at similar latitudes. According to the Köppen climate classification [8], the Svalbard climate is a Tundra Climate (classification ET), a subtype of the polar climate [9]. In this type of climate the mean monthly temperature never exceeds 10 °C, but at least in one month the average temperature results above freezing (0 °C), implying snow melting during summer. The effects of the NAC are usually visible on the west coastline of the archipelago, that is usually free of ice and hence navigable most of the year. The north-eastern coast instead is blocked by sea ice during winter (Figure 3a) [10]. Minor temperature differences are present between the northern territories and the southern ones, mainly due to the NAC exposure and the latitudinal extent of the archipelago [11]. Most of the interior territory is covered by mountains, so that, compared to the coast, the inland temperatures show less seasonal variations. As a result, many glaciers exist on Svalbard, that last over summer and are visible from satellite images (Figure 3b). Anyway most of them have a negative mass balance, meaning that they lose more ice mass during summer than the one they accumulate over winter.

Thanks to the presence of urban settlements, Svalbard has a quite long meteorological data series, starting from 1911, when the first permanent weather station was established in Green Harbour, about 37 km South-West of Longyearbyen [12] [13].

The temperature time trends aquired over the last century (Figure 4) have shown that the Arctic is one of the most sensible areas to climate change.

Comparing nowadays temperature data to the first records available, a significant rise of the mean temperatures in the region can be seen. Table 1 shows air temperatures from [13], where two 30-years climatological periods have been considered, in order to make a time comparison. During the first period, from 1961 to 1990, the annual mean temperature recorded at the Svalbard Airport in Longyearbyen was -6.7 °C, while during the second period, from 1981 to 2010, it had rised to -4.3 °C, resulting in an increase of 2.4 °C. At the same station the increase in the last 100 years reaches almost 1.2 °C per decade [13]. In addition, all the other stations present a similar warming trend, both in the annual and seasonal averages. Anyway, the warming rate can also depend on the location, since orographic and oceanic factors can vary their contributions significantly.

Regarding the precipitation, as for the temperature, the annual averages vary markedly in the archipelago, depending on the location of the weather station. At the Svalbard Airport the annual mean is, for both the periods 1961-1990 and 1981-2010 around 190 mm/year, while for example in Ny-Ålesund it changed from 385 mm/year

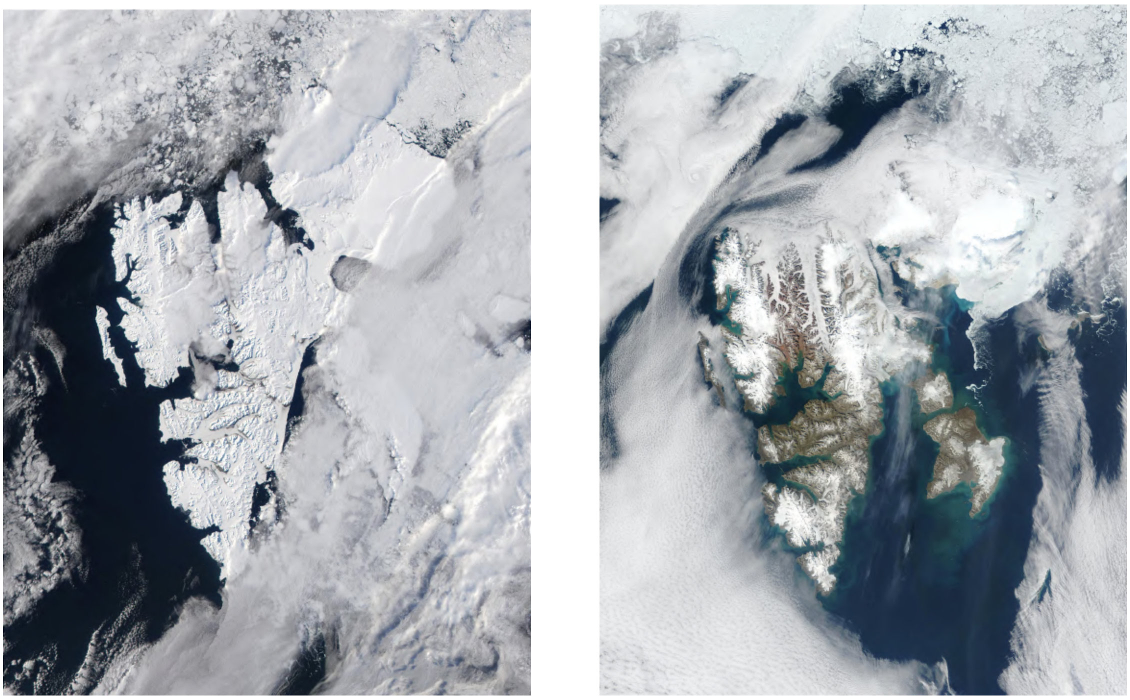

(a) **Satellite view of Svalbard during winter.** The image was taken on 7 June 2001. It is visible how the entire surface of the archipelago is completely covered in snow. On the north-east coast a lot of sea ice is present.

(b) **Satellite view of Svalbard during summer.** The image was taken on 12 August 2002. The presence of snow has decreased considerably, as well as the extension of the sea ice. Anyway, some glaciers are visible and resist through the summer.

Figure 3: Satellite view of Svalbard during winter and summer respectively. Obtained by an RGB composite of different channels from MODIS satellite. Source NASA.

to 427 mm/year. In fact, it seems from observation that total annual precipitation has increased by 14% northern of 60°N over the last century [15].

These trends in temperature have many other effects, both on the physical and biological domains. For example, the first snow-free day is usually defined as the day of the Julian year when the snow cover goes under a certain threshold for a certain area. For many regions, this day is coming earlier and earlier in the year [16]. On the biological side, plants and animals are usually synchronized with seasonal cycles. Therefore, changes in processes timings can affects their bio-rhythms. For example the phases that determine the life cycles of the plants, called phenological phases, are mostly affected by changes in temperature and therefore climate change can affect them [17]. Primary production is the process where organic compounds are synthetized, mainly through photosynthesis, starting from carbon dioxide, CO_2. In the ocean, the majority of the photosyntesis is done by phytoplankton, that are microscopic algae, and some bacteria [18]. In the Arcitc, these organisms are not operating during the dark and cold winters, but become active when the solar radiation starts to penetrate the sea surface and temperature rises. Above-average temperatures can therefore activate

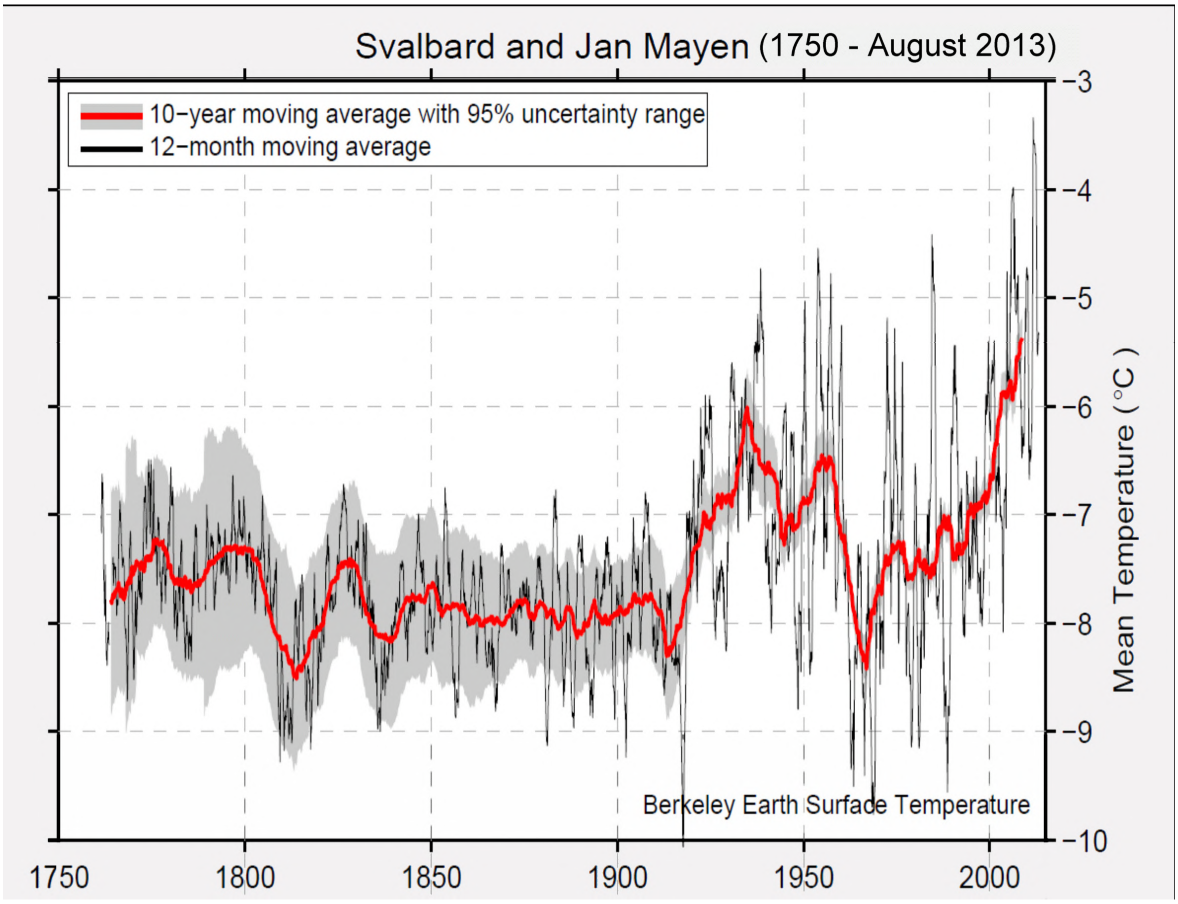

Figure 4: **Temperature time series as anomalies relative to the 1951-1980 average for Svalbard and Jan Mayen**, adapted from `https://berkeleyearth.org/` [11]. Temperatures before 1911 were retrieved through interpolation with other stations [14].

an earlier primary production [19], with effects on the reserve of resources that these organisms use [20].

Station	1961-1990					1981-2010				
	Annual	Winter	Spring	Summer	Autumn	Annual	Winter	Spring	Summer	Autumn
Ny-Ålesund	-6.3	-13.8	-9.8	3.4	-5.3	-5.2	-12	-8.5	3.8	-4.4
Svalbard Airport	-6.7	-15.1	-10.8	4.2	-5.2	-4.6	-11.7	-8.3	5.2	-3.5
Hopen	-6.4	-13.4	-9.9	1.3	-3.8	-4.3	-9.9	-7.6	2.3	-1.9
Bjørnøya	-2.4	-7.6	-4.8	3.5	-0.5	-0.9	-5.1	-3.4	4.4	0.6

Table 1: Annual and seasonal temperature means for four different stations in Svalbard, and for two different 30-years climatologic periods. The increase of the mean temperature is evident for all the means and all the four stations. Adapted from [13].

1.2 Snow and the snowpack

Snow is an crucial component of the cryosphere during winter, as it globally represents the second largest interface between the atmosphere and the Earth's surface [21]. Due to this major interaction, snow dynamics and its response to external events are essential for a deeper comprehension of the climatic system, its past variability, and its future conditions..

Snow is defined as a material composed of ice crystals, that is water in crystalline phase. Ice crystals form in the clouds, where the air temperature reaches low enough values to make the water vapor or the water droplets freeze, through the help of particles called *ice condensation nuclei*.

The albedo of a material is defined as the fraction of reflected radiation out of the total incoming solar radiation. It can range from 0 to 1 (or from 0% to 100%), that respectively represent a completely black and a completely reflective object. Snow albedo can significantly vary depending on its characteristics. Fresh snow can have albedo values up to 90%, while aged or very dirty snow can have values as low as 20% [22]. Due to this reason, the snow cover and the snow properties are very close connected to the radiation budget of a certain area and of the whole globe, since can reflect and absorb different amounts of radiation. The snow cover extent is predominantly affected by air temperatures. Higher temperatures increase snow melting, reducing the snow-covered areas and exposing darker substrates to the solar radiation. Indeed, snow cover is critical for the radiative balance not only for its intrinsic high albedo, but because it usually covers areas with relatively low albedo. Trees for example usually do not reach values of 20% [22].

Compounds stored in the snow can strongly influence its radiative behavior and its albedo. Black carbon for example is an fine aerosol, usually belonging to the PM2.5 category (aerosols with diameter less then 2.5 µm), and it is mainly generated by combustion. As the name suggests, this compounds results black in color, and when it deposits on the snow, it lowers its albedo and subsequently warming it, making it melt faster than normal.

The term *snowpack* usually refers to the snow accumulated with different snowfall that persists on the ground or on any surface for a prolonged period of time [23]. It is called *seasonal* when it last less than a year, melting during late spring or summer. During the cold season each snowfall creates a different and usually recognizable layer in the snowpack, containing all the characteristics of that snowfall.

After the deposition, a process called *snow metamorphism* takes place. Since the seasonal snowpack temperatures usually oscillates around the triple point of water, 273.16 K, many thermodynamical processes can occur, drastically changing the snow physical properties. These changes are called snow metamorphism [24].

Snow compaction is a snow metamorphism process that helps in increasing the snow layers densities, and it occurs through three major processes [24]. Under the action of the wind, snow drift rounds the snow grains through collision and sublimation. This process can increase up to three times the snow density once the rounder grains are deposited again on the surface. Through heat exchanges and vapor diffusion, the ice crystals are transformed and become more granular, increasing the snow layer density. Lastly, the layers below in the snowpack suffer the pressure from the overlying layers weight, making the snow grains break, deform, and melt, therefore compacting and incresing the density. These processes are usually clearly visible in snow height time series, as just after a heavy snowfall, in a few hours or days, the accumulated height decreases.

The formation of ice crusts is important for heat transfer processes in the snowpack. When liquid water is deposited on the snow surface, it can freeze into ice if the surrounding temperatures reach low enough values. In this case the ice creates a layer that can be found either on the surface or in depth, if the liquid water was able to penetrate the snowpack in time [25].

Then, usually in spring, when the air temperatures increases above 0 °C, the snowpack warms up, quickly becomes isothermal at 0 °C, and starts to melt, until it eventually disappear in a shorter time than the one needed to build up [21]. In case the snowpack doesn't melt over summer, it becomes *firn* (from the Swiss, "from the year before"), that is a peculiar kind of snow, more compact due to metamorphism.

Finally, when the firn reaches a specific depth, called *close-off depth*, at which the pores between the snow crystals are fully isolated, it transform into ice through a process called *sintering*, making the density increase. The firn-to-ice transition depth can vary from few meters for mid-latitudes glaciers up to hundred of meters in the Antarctic Plateau. Anyway, only the seasonal snowpack will be analysed in this work, as it is more thermodynamically unstable with respect to firn or ice, and therefore very sensitive to specific weather events.

All these presented processes can be included in a snowpack mass balance equation:

$$\frac{dM}{dt} = P + E_{subl} + E_{evap} - R \tag{1.1}$$

where P is the solid or liquid precipitation rate, E are the sublimation or evaporation rates, and R is the runoff rate. However, the mass balance is influenced by many other external factors.

Both the small-scale topography and the large-scale one influence the snow mass balance. If the area is located leeward with respect to a big obstacle as a mountain range, the amount of snow that is deposited on the ground can strongly diminish, while on the windward site snow accumulation is increased. Another crucial factor is the surface inclination, that can prevent the accumulation due to gravity, and favorish runoff of melting water .

Vegetation is another influencing factor, that acts intercepting the solid precipitation and trapping it on the tree crown. When the snow load on the tree exceeds a certain threshold, or is moved by the wind, the snow is released to the ground, a process called snow unloading. Nevertheless, since Svalbard flora is mainly composed of non-vascular plants, such as mosses and lichens, vegetation effects are negligible [26].

Wind can also affect the snow deposition through the phenomenon of blowning snow. The term refers to the snow lifted by the wind and transported to other areas, leaving some zones with less snow and accumulating it on others. The effect is particulary important where wind intensity is usually high, over open windy flat regions, and also in proximity of obstacles, such as boulders or mountain slopes [24], where snow accumulates on the windward side.

The snowpack is also an important reservoir of water, accumulated in a long interval of time and released in a brief period when it melts. This significant amount of water is usually released into the ground or on the surface by runoff. During melting, all the contaminants and aerosols accumulated and stored for several months in the snowpack are generally released in a few weeks, implying high concentrations that lead to different geochemical processes with respect to the winter season.

Svalbard surface is covered from 60% to 100% by seasonal snow, as the majority of the snow cover disappears in summer, except for glaciers on the mountains. This work will concentrate on seasonal snow on land deposited over a flat area close to Ny-Ålesund, Svalbard. In the framework of the ongoing climate change, a comprehensive analysis of the evolution of the seasonal snow cover can provide vital informations to to better understand current changes in the Arctic climate and to monitor the environmental health of the Arctic ecosystem.

1.2.1 Snow physics

Physical properties such as snow temperature, liquid water content, or the shape of the snow grains, can provide meaningful informations about the snowpack conditions and about the meteorological events that played a significant role in building and shaping the individual layers throughout the snow season.

Physical properties of the snow

Snow physical properties are all the characteristics of snow that can be measured, such as its temperature, its density, or its hardness. The existence of different types of snow have been noticed for a long time, due to interests outside the scientific community. In fact, the interaction between nordic population and snow, lead them to classify this material in order to better describe it in different conditions. Populations such as Sami (located in Scandinavia) developed around 180 different words to describe vary snow or ice conditions. All these words can be associated to different states of the snow, and therefore to different physical properties of it. For example, in the Sami language, *Vahca* refers to the new snow, to which bad travel conditions but easy animal trace following are associated. *Geardnui* refers to a thin ice crust created when rain freezes, *Sievlla* refers to very wet snow where it is very hard to walk in, and so on [27].

After many years, the "International Classification for Seasonal Snow on the Ground" was published in 2009, under the UNESCO International Hydrological Programme [28], and it is now considered the starting reference for snow research. According to snow science, the most important snow physical properties are the following.

- Grain shape: the shape of the snow grains are divided into different categories, each one identified by a symbol and a code. The category is defined depending on the shape and the type of the snow or ice. Some shapes are Precipitation Particles, Rounded Grains, Faceted Crystals. The shape is experimentally determined with a magnifying glass by similarities with a *crystal card.*

- Grain size [mm]: six different categories exist depending on the size, from less that 0.2 mm up to more than 5 mm.

- Snow density [kg m^{-3}]: mass per unit volume, usually determined through the weight of a sample of known volume.

- Snow hardness: The snow hardness is defined with a six-steps scale, following the international Hand Hardness Index (HH-index) [28]. The HH-index goes from 1 to 6 and it is measured based on which object can easily penetrate a certain snow layer, as shown in Table 2.

Definition	**HH index**	**Object Penetrating**	**Code**
Very soft	1	Fist	F
Soft	2	4 fingers	4F
Medium	3	1 finger	1F
Hard	4	Pencil	P
Very hard	5	Knife blade	K
Ice	6	Ice	I

Table 2: Hand Hardness Index: the object that can easily penetrate the snow layer defines the hardness index.

- Snow water equivalent [mm]: defined as the total amount of water, usually measured in mm, that the snow would create if completely melted. It can be approximated by the formula [29]

$$\text{SWE } [mm] = \text{H } [cm] \cdot \frac{d\ [kg/m^3]}{100} \tag{1.2}$$

  where H is the height of a certain snow layer and d is its density. The factor of 1000 is needed for units conversion.

- Snow temperature [°C]: snow temperature, measured in °C.
- Impurities [%]: mass fraction of impurities in the snow, usually recorded only when they influence the physical properties of it, such as when dust, sand, or soot are present.
- Layer thickness [cm]: thickness of a layer of uniform snow, taken perpendicular to the ground surface.

We can lastly define two snow macrocategories: dry and wet snow, where each one implies a different type of snow metamorphism. Dry snow refers to the snow that does not contain liquid water, that completely freeze when the temperature is below $0\,^{\circ}\mathrm{C}$. Wet snow refers instead to the one that contains liquid water, when the snow temperature is around $0\,^{\circ}\mathrm{C}$. In the first case exchanges from and to the liquid phase can be neglected, while in the latter case exchanges between all the three water phases have to be considered. These changes can be mainly investigated by measuring the mixing ratio between the three phases, ice, liquid water, and air. This mixing ratio can be easily studied through the snow density. Low density implies a great amount of air between the snow grains, and probably no presence of ice. As the density increases the relative amount of air decreases as the snow grains compact, and even higher densities may suggest the presence of ice. Snow density can range from about $50\,\mathrm{kg\ m^{-3}}$ to $550\,\mathrm{kg\ m^{-3}}$ (note that ice density is about $917\,\mathrm{kg\ m^{-3}}$, and water density about $1000\,\mathrm{kg\ m^{-3}}$).

Temperature profile of the snowpack

The temperature profile of the snowpack is defined as the vertical distribution of snow temperature at a certain time. The temperature profile usually includes the surface temperature T_{surf} and the ground temperature T_{ground}.

The heat exchanges of the snowpack mainly occur at the two boundary regions, the surface layer and the ground layer. The surface layer is the main actor of the interations between the snowpack and the atmosphere, while the ground layer is responsible for the interactions between the snowpack and the soil or permafrost. These two regions encompass the major heat fluxes influencing the snow temperature profile. Other heat exchanges can happen when particular events, that act as sources and sinks of heat, take place. Snow transformations such as freezing or melting can respectively release or absorb heat, influencing the nearby snowpack. Other events that include water percolating in the snowpack, such as rain or melting, can additionaly warm up the lower bottom layers.

In flat, homogeneous regions, the temperature vertical profile of the snowpack usually doesn't change so much in the horizontal direction, but it can be considerably affected by changes in the topography or in the vegetation. For example the presence of trees or rocks can greatly influence the heat exchanges in the two boundary layers.

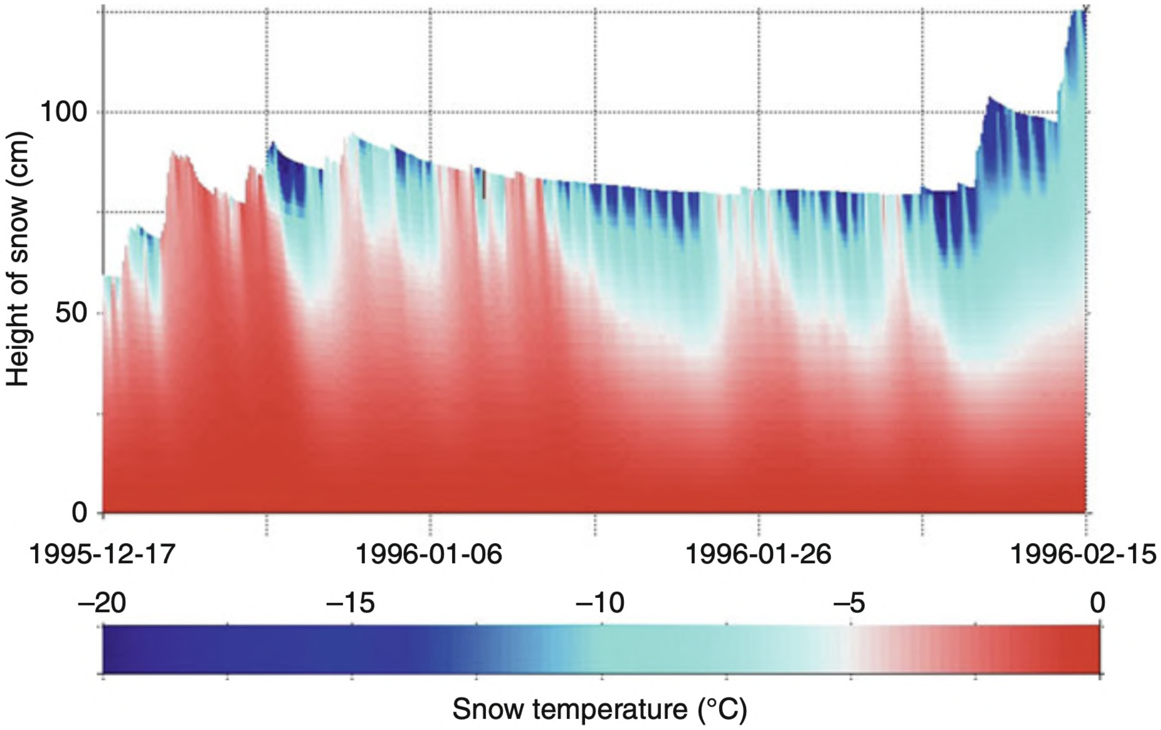

Figure 5: **Temperature profile time series.** Picture created from the SNOWPACK model, adapted from [30].

From the evolution of the temperature profile different events can be identified, such as particulary warm or cold air temperatures that propagate in the snowpack from the surface. For example, the melting season is usually identified when the profile becomes isothermal at 0 °C, around late spring.

The temperature profile can be experimentally measured using thermometers. If possible, measurements should be spatially denser at the surface, since it is the region where most of the processes take place. There are two major methods to measure the temperature profile [30]. The first method requires to dig a snowpit, that is a vertical trench dug in the snow, so that flat vertical snow plane is exposed to the air. If the sun light is present, the snowpit needs to be shadowed so that it doesn't warm up. Then, probe thermometers are inserted horizontally in the snowpack at certain height, and the measured temperature recorded. The second method, that allows a way higher temporal resolution, requires the use of automatic sensors. When the ground is completely free of snow, a pole is installed on a preferably flat site, free of obstacles, and far from any inhomogeneities. On the pole several snow thermometers are placed at different heights, so that when the snowpack covers them, each one measures the temperature at a different depth, with a high temporal resolution.

1.2.2 Snow chemistry

Many different elements are present in the atmosphere, due to natural and antropogenic processes. These water-soluble ions and trace elements (defined as those elements whose concentration is very low, usually less than 100 ppm), have a major role in atmospheric processes, from cloud formation to radiation budgets. When ice crystal form through cloud microphysics processes, many of these species are collected into the crystal (or even act as condensation nuclei for the crystal), and they end up being part of the snow and therefore affect its properties. Otherwise, these compounds can deposit on the surface through dry deposition, still affecting radiative properties.

For example, black carbon (BC), mainly present in soot, can decrease the snow albedo hence influencing the radiation budget of snowy areas. The change in the snow surface reflectivity due to BC deposition can eventually trigger early melting of the snowpack.

Many ionic species, that are elements in form of ions, usually ionized due to dissolution, come from natural sources. At the interface between the sea and the atmosphere, wind creates waves and foam that contains many marine compounds, that through bursting bubbles, are released into the air. Through this process, abiotic ions such as Cl^- and Na^+ are released into the atmosphere and eventually transported to other locations through wind, and settled on the ground by wet or dry deposition. Primary production products such as MSA are called biotic since they originate from biological processes occuring in the ocean and are subsequentially transported on the land as sea spray. So when primary production is active, an increase of these products, together with Cl^- and Na^+ is expected as result of ocean-to-land air mass transportation [18]. Other elements, such as Al, Fe, and other metals, are generally grouped in the *crustal* category, as they mainly come from soil and rocks. They make up the crustal dust, that mainly originates from the wind erosive action or landslides. These elements, including most of the metals, are generally categorized as trace elements [31]. Anyway, several trace elements have also source in anthropogenic activities, such as combustion of fossil fuels, agriculture, and industries. The transport of these compounds occurs in the same way of the natural ones, so that sometimes it results hard to discriminate the sources. Analysing many different compounds, it is possible to estimate if they come from natural or anthropogenic sources.

Water stable isotopes such as Oxygen and Hydrogen isotopes are another important proxies commonly measured in snow and ice samples, through which past temperatures can be retrieved. The most import isotope ratio is the δ^{18}O, that is defined through the concentration of two stable oxygen isotopes, ^{18}O and ^{16}O,

$$\delta^{18}\mathrm{O} = \left(\frac{\left(\frac{^{18}\mathrm{O}}{^{16}\mathrm{O}}\right)_{sample}}{\left(\frac{^{18}\mathrm{O}}{^{16}\mathrm{O}}\right)_{std}} - 1 \right) \cdot 1000‰$$

Since the deposition on ice of the heavier ^{18}O depends on the global temperature, measuring its ratio with the most abundant isotope ^{16}O, allows the retrieval of temperature in the past.

1.3 Arctic Meteorology

Polar regions are gaining interest in the recent years due to their major role in the climatic system and the big sensibility to climate changes and global warming. However, these regions are surely among the most unaccessible areas in the world, as much as they are unhospitable for human life. As a result, very few meteorological station exist in the poles, especially in the Antarctic continent. In fact, these station usually require periodic maintenance that is challenging to provide in harsh climatic conditions. The Svalbard archipelago indeed, due to its easier accessibility, is a more favourable place, and more data are available with respect to Antarctica. More meteorological stations are installed, and even daily radiosoundings are done in ceirtain areas.

Puntual instruments include modern Automatic Weather Stations (AWS), that are weather stations that can be placed in remote sites, built to avoid regular maintenance. These stations include the instruments to measure the most common meteorological variables, including temperature, wind speed and direction, humidity and pressure. They usually include a power supply, such as solar panel or wind turbines, to be completely autosufficient. Similarly, to collect data in the ocean, weather buoys are available.

Remote sensing is one of the major data supplier for the land, the atmosphere, and the ocean, as they allow data collection on wide regions at the same time. Particular orbits, called polar orbits, allow a good revisit period for polar regions, and are the main configuration used for polar data retrieval. As more and more satellite are being launched in orbit, more and more data will be available in the future.

Anyway, these instruments provide data confined either spatially (fixed-location weather stations) or temporally (due to satellite revisit period), and hence bring the risk not to collect data for a specific meteorological event. In order to fill this gap, reanalysis data are usually used. Reanalyses allow the retrieval of data with a good spatial and temporal resolution and no gap. In this way, all the meteorological events that you may want to study, if detected by the reanalysis, are available. The reanalysises produce their data based both on models and real data, and they will be further discussed in section 2.3.1.

With all these weather data, the arctic meteorology has been studied and its major features have been identified by previous studies. As said, this work will focus on a particular kind of event, called Rain on Snow (ROS) event, happened in March 2022 on the Svalbard archipelago. More details about these kind of events are described in Section 1.3.2.

1.3.1 Major synoptic structures

In order to understand how the March 2022 event generated, how it developed, and how it affected different components of the cryosphere, a study of the major arctic synoptic structures must be conducted. In the following pages, characteristics of the arctic meteorology are described.

Polar Vortex

The major tropospheric synoptic structure at high latitudes is the polar vortex, that is an approximately circular region over the north pole that contains cold air. The definition of the tropospheric polar vortex relies on the definition of the tropospheric jet stream, that is a fast eastward air current located at around 10 km of altitude, at about 60 degrees latitude, present both in the northern and the southern hemisphere. The polar vortex is then usually defined as the region of troposphere (the layer of atmosphere reaching the tropopause, at around 9 km at the poles) contained inside the jet stream. The boundary location is usually identified with the geopotential height at 500 hPa [32]. Inside the polar vortex, around the North (or South) Pole, dense and cold air is contained, while outside, toward the middle latitudes, there is warm and moist air.

The strength of the polar vortex can vary through time, and it can present itself either in a strong configuration or in a weak one, affecting in this way the movements of cold and warmer air masses. The strong polar vortex configuration, as the one represented in Figure 6a, confines the cold air inside at high latitude and the warm air at middle latitudes. When the jet stream weakens, its path becomes unstable and meanders start to form, as in Figure 6b, bringing cold air toward the mid-latitudes and warmer air toward the pole.

The jet stream, and hence the polar vortex, is produced by the action of solar radiation on the terrestrial atmosphere. Due to different total insolation between the poles and the equator, a meridional temperature gradient creates. Adding to this the Coriolis acceleration, three main atmospheric cells in each hemisphere arise. Starting from the equator and going poleward, firstly the Hadley cell is encountered, then the Ferrel cell, and lastly the polar cell. Between the Ferrel and the polar cell, at around 60° N, the jet stream arises, and so the polar vortex. With rising temperature due to global warming [33], the meridional temperature gradient between the equator and the poles, is weakening due to the major temperature sensibility of the poles with respect to the equator [3]. The weakened meridional temperature gradient weakens the jet stream, and so the polar vortex, that diminish its circulation creating more and more accentuated meanders [34]. Moreover, anthropogenic aerosols may enchance the jet stream meandering through the creation of more small ice crystals [35].

The strength of the polar vortex can be associated to the the North Annular Mode (NAM) index, computed as the daily geopotential anomalies between 20 °N

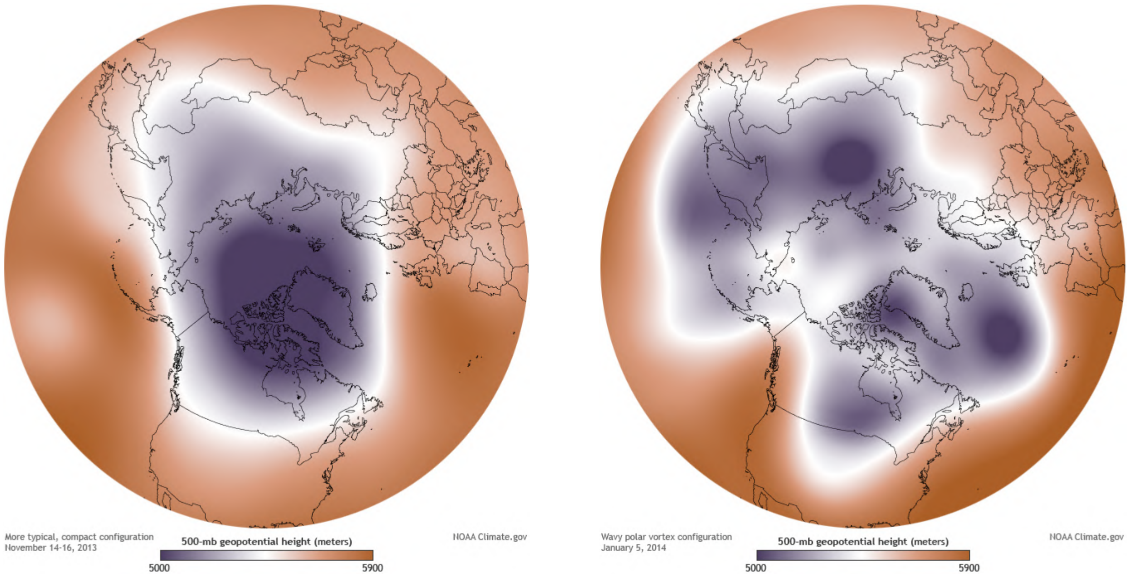

(a) **Strong polar vortex configuration.** The figure represents mid-November 2013

(b) **Weak polar vortex configuration.** The figure represents January 5, 2014.

Figure 6: The plotted variable is the 500 mbar geopotential height. Maps by NOAA Climate.gov, based on NCEP Reanalysis data from NOAA ESRL Physical Sciences Division.

and 90 °N at different pressure levels. Adapting from the definition of strong and weak stratospheric polar vortex by Baldwin and Thompson [36], the tropospheric polar vortex can be considered strong if the daily NAM index at 500 hPa exceeds the 75th percentile, and weak if the same index goes below the 25th percentile. If computed at sea level, the NAM index corresponds to the Arctic Oscillation index (AOI), so that the latter one can also be used to define the polar vortex strength.

Typical synoptic configurations

The synoptic configurations over the North Atlantic are usually classified in different categories, based on the location of major high or low pressure centers. This can be done applying a clustering algorithm or other classification methods over the 500 hPa geopotential [37]. Through these techniques, four major categories are identified, associated to four distinct configuration, as represented in Figure 7. Similar regimes can be obtained over the North America region [38].

- NAO- regime: characterized by a high pressure system over Greenland and a southern low pressure system, over the Atlantic ocean.
- Atlantic Ridge (AR) regime: the high pressure system is localized over the North Atlantic Ocean, just below Greenland and Iceland coasts.
- Scandinavian Blocking: this configuration is the opposite of the AR regime, presenting a high pressure system over Scandinavia and a low pressure system over

southern Greenland.

- NAO+ regime: the most common regime in DJFM months [38], characterized by the Icelandic Low and the Azores High.

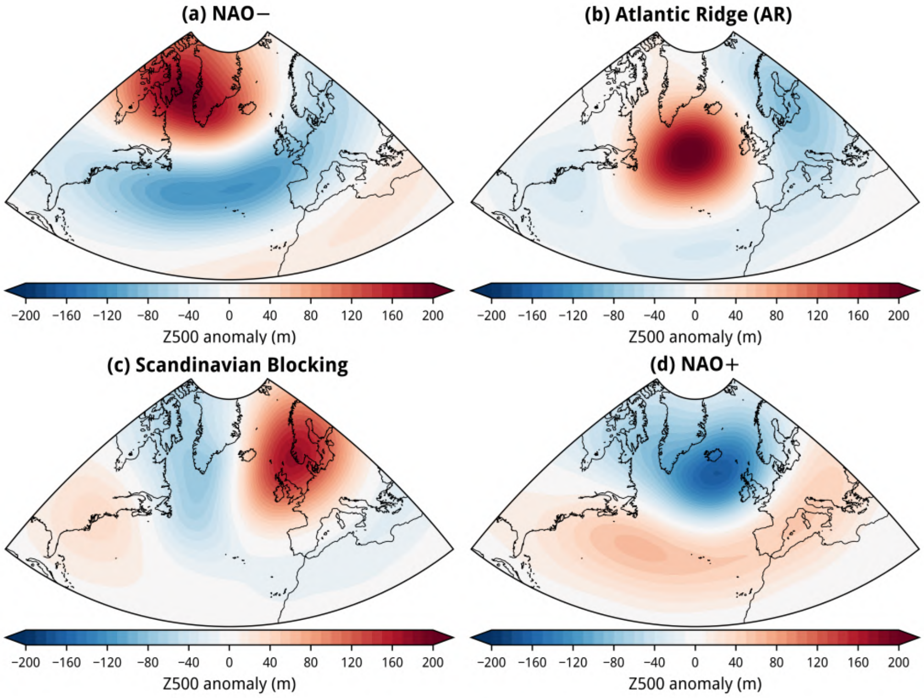

Figure 7: **The four main atmospheric regimes in the North Atlantic.** Picture adapted from [38].

Each one of these configurations is generally associated with peculiar weather conditions all over Europe. For example, the NAO+ regime is tipically associated with positive temperature anomalies (meaning warmer than normal) in central Europe, while the Scandinavian Blocking makes central Europe drier and the Mediterranean area wetter.

Polar lows

Polar lows are another characteristic synoptic structure in the polar meteorology. They are, as the name suggests, low pressure system that are usually found over the oceans at high latitudes. They are defines as ”mesoscale cyclonic vortices poleward of the main polar front” [39], meaning that they are approximately found poleward of 60° of latitude, and their horizontal scale is usually less then 1000 km. Their lifetime is usually short, from a few hours up to 36 hours, and they usually develop above the ocean, over ocean-ice or ocean-snowpack boundaries. They are associated with severe weather, including snow blizzard and fast winds, posing a big threat to local communities [40].

They can be classified accordingly to different criteria, including genesis processes, morphology, or even cloud signature, that divides them in two distinct groups, comma-shaped and spiraliform, as represented in Figures 8a and 8b.

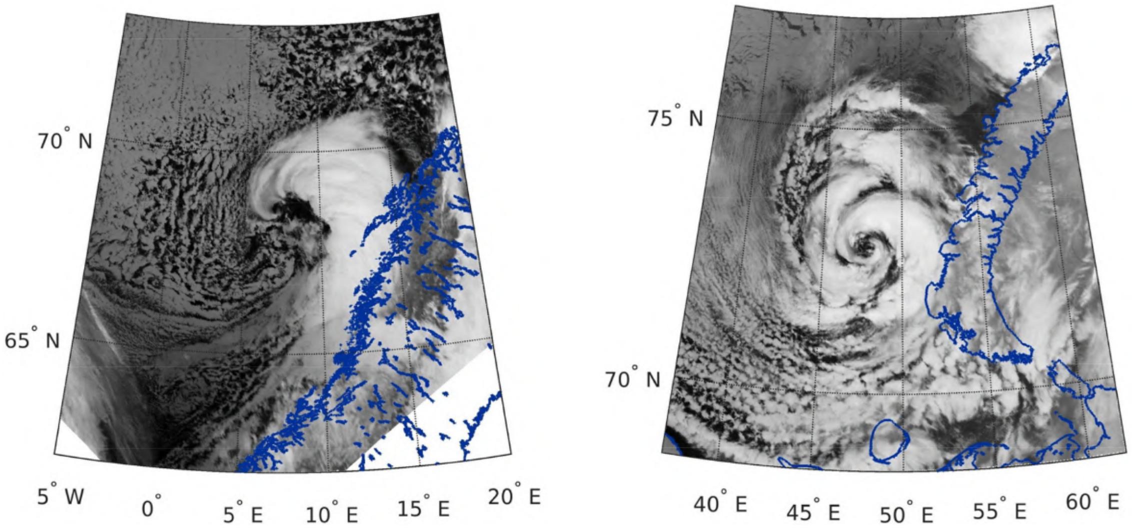

(a) **A comma-shaped polar low.** The cyclone was located offshore of the Norwegian coast.

(b) **A spiraliform polar low.** The cyclone was located over the Novaja Zemlja archipelago in Russia.

Figure 8: Two different shapes of polar lows. Pictures adapted from [40].

As an example, on the morning of 19th December 2015, a polar low reached Svalbard, creating an avalanche that hit some houses in Longyearbyen, destroying 11 of them, trapping more than 20 people, and killing two [41].

As these high-latitude cyclones are increasing in frequency during the winter season (December, January, February, DJF) [42], a better understanding is needed to increase their comprehension, and therefore increase prevention and a decrease in fatalities.

Weather correlation with climatic indices

The correlation of polar weather with climatic indices has been studied mainly looking at the North Atlantic Oscillation (NAO), a natural phenomenon happening in the North Atlantic [43]. The NAO phase is identified by measuring the seasonal air pressure difference between two weather station, usually one in Portugal and one in Iceland (that is Reykjavík due to its long weather record). These two areas where chosen due to their proximity to two permanent pressure systems, the Icelantic Low and the Azores High. The difference between these two weather stations defines the NAO index, whose values generally vary between −3 hPa and 3 hPa. The different NAO phases influence the weather at mid-high latitudes. Since it is linked to the position of the Azores high, it is also associated to the development and the direction of polar lows. Other indices exist, included the Arctic Oscillation index (AOI) previously mentioned in 1.3.1.

Still in the Northern Hemisphere, the Atlantic Multidecadal Oscillation (AMO) is a climate variability phenomenon linked with oscillations in sea surface in the North Atlantic Ocean, happening on a period of tens of years. There are suggestions that the AMO plays an important role in modulating the Arctic amplification process during decades timescale. [44]

The El Niño-Southern Oscillation, associated with the El Niño index, is a climatic phenomenon connected with the increase of sea surface temperature of an equatorial region in the Pacific Ocean. This event happens almost periodically, with a period around five years, and has major consequences in different regions of the globe, through the so-called *climate teleconnections*. Some models indicate that these small changes in Pacific Ocean can have effects on the surface air temperature in the Arctic [45].

Atmospheric Rivers

Another atmospheric structure that can be found in the polar regions, even if it is generally located at mid latitudes, are the Atmospheric Rivers (ARs). The name comes from the typical shape of this structure, that presents itself as a long and narrow filament of very moist air, that can extend for thousands of kilometers while remaining just a few hundreds of kilometers wide. They usually originate from warm tropical ocean water, and they transport moisture in form of water vapor poleward. These atmospheric rivers are very important to the society since they can cause heavy rainfall and severe damages. For example, the California state in the United States receives about up to 60% of the yearly precipitation from atmospheric rivers created over the Pacific Ocean, as the one in Figure 9. Between the end of December 1996 and the beginning of January 1997, precipitation from an intense AR hit California for about 100 hours, causing more than 1 billion dollars in damages [46].

These argumentations are valid also in the Arctic, where even if the population size is much smaller than mid latitudes countries, people are not prepared for such severe events, and naturally harsh conditions can even more complicate eventual emergency rescues. On the environmental side, it is known that poleward transport of moist and warm air from the mid latitudes easily triggers sea ice loss [48], and this could happen in periods outside the normal timings, disturbing and altering the Arctic ecosystem cycles.

Increases of moist air has been reported in the Arctic, that may come both from poleward transport from mid-latitudes and from local sources, due to sea ice decline and increase in temperature. Indeed, ARs can act as major ways of water transport from mid-latitudes to the poles, and could explain most of the moisure anomalies in Svalbard [49].

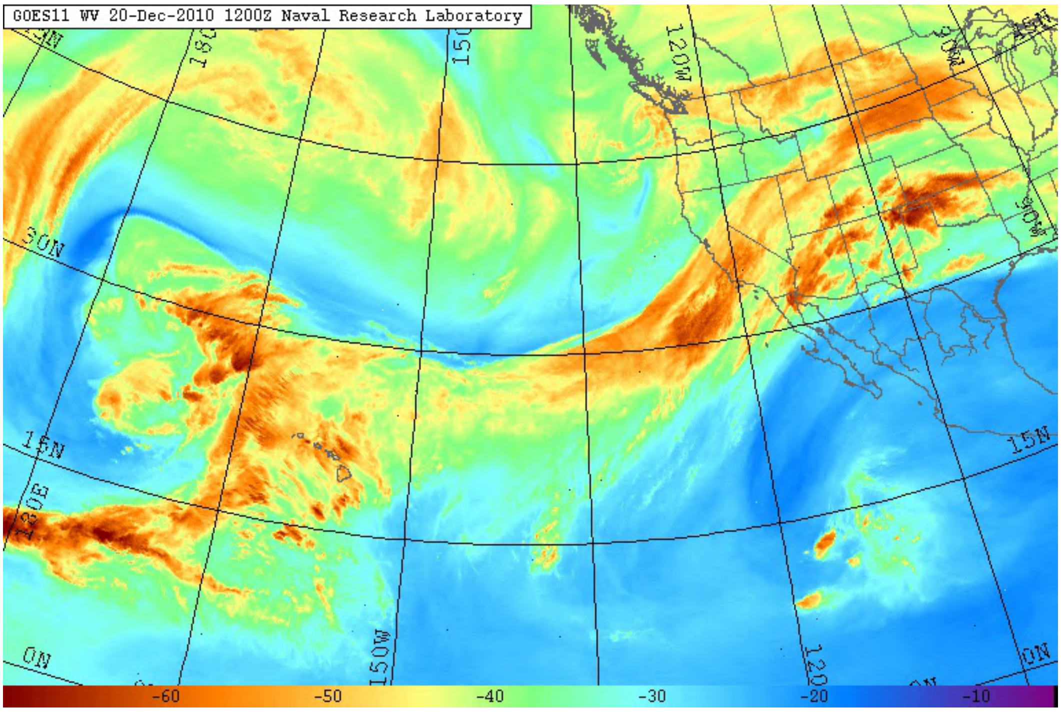

Figure 9: **Atmospheric River over California in December 2010.** The plotted variable is water vapor, measured by the GOES11 satellite. It produced as much as 660 mm of rain in California and 5.2 m of snow in the Sierra Nevada. Picture adapted from [47]

1.3.2 Winter Warming Events and ROS events

The polar amplification process sets problems that were never (or rarely were) tackled in the past. In the recent years in fact, extremely warm weather events in winter have been recorded in the Arctic. These events are called Winter Warming Events (WWE) and are often accompanied by intense rainfall, while no liquid precipitation would be expected during the cold season due to rigid temperatures, often below the freezing point. If rain occurs, the event is called Rain On Snow (ROS) event. These particular events can strongly affect both the cryosphere and the biosphere. If temperatures drop below the freezing point after the rain event indeed, a superficial or internal layer of ice can form, disturbing both animals, preventing winter graze, and human activities, transportation and infrastructures, and acting as a lid between the ground and the atmosphere, perturbing the exchanges between the two [50]. These events can also increase soil and permafrost temperature. In fact, in regions where permafrost temperatures are close to 0 °C, even small increases in temperatures can have effects on its thickness and extent [51].

These extreme events are slowly increasing in the winter season [52], creating the need for a deeper understanding, how climate change affects them, and how they can influence both the environment and the society. In December 2015, a salient WWE happened around the North Pole, reported to have set a record in buoys temperature measurement series [53]. During the month of December, the surface air temperature near the North Pole was around $-25\,^{\circ}\mathrm{C}$, but in 24 hours, from 29 December to 30 December, the air temperature increased up to $-0.8\,^{\circ}\mathrm{C}$, and returned to monthly averages in another day [53]. The temperature values reached in this event reached the 99th percentile of mid-winter temperatures ever recorded in the area.

It is hard to associate the increase of these events with different pressure patterns [54], and the causes may be found in other components, affected by climate change too. Arctic sea ice decline may in fact be responsible for disturbing exchanges between atmosphere, ice, and ocean, leading to increased heat and moisture fluxes from the atmosphere toward the atmosphere. Greenland sea ice could protect Svalbard from poleward moisture fluxes, and decreases in it could increase WWE in the region [55].

1.4 Thesis objective

The aim of this thesis is to analyse in detail a ROS event happened on Svalbard on 16 March 2022. The main objective is to carry out a comprehensive analysis that focuses on many cryospheric components for which data are available, in order to evaluate the effect of the ROS on them. The cryosphere will be analysed in great detail, but also the synoptic configuration will be studied to understand how the event generated.

Firstly, the data collection process will be described, including all the different dataset used for the analysis, as well as the laboratory procedures and the analytical instruments used to chemically characterize the Svalbard snowpack, carried out during the internship at the Council of National Research - Institute of Polar Sciences (CNR-ISP) in Mestre, Venice.

Secondly, the obtained results will be presented. Different dataset will be used, including reanalyses, weather stations, satellite data, and snowpack models. The apparently separation between these different datasets will be overcome, so that results from different areas can be combined to better understand the phenomenon.

The goal of the analysis is to understand exploit many of the effects a ROS event in Svalbard has on the various components of the cryosphere, as some of them could be still unknown or not well characterized. Most data will analyse the snowpack, through the use of physical and chemical variables, to see how the ROS event influenced them.

Chapter 2

Methodology and Data

In this chapter, technical details about weather stations, satellite, observation, reanalyses, and other datasets used in this work, are described. The use and the aggregation of very different datasets has been one of the main objectives of this thesis, in order to return a comprehensive understanding of the event. The section will start with the description of the Gruvebadet snow research site (GSRS) and its Automated Nivometric Station (ANS), then it will introduce with the snow sampling activities led by CNR, and finally the laboratory analysis carried during the internship of the candidate. Additional information about reanalyses, atmospheric models, other weather stations, and ending with the MODIS satellite and a snowpack numerical model will be also presented.

2.1 The Gruvebadet Snow Research Area

As part of the CNR research activities, snow samples are collected throughout all the snow season at the GSRS, located at about one kilometer south of Ny-Ålesund, Svalbard. Although the GVB aerosol observatory, run by CNR-ISP since 2010, is mainly focused on atmospheric chemistry and aerosol size distributions, since late 2018 also snowpack research has started, with the installation of a nivometric station [56]. At the GSRS site, the snow generally last from November to June, but it can vary from an year to the other.

The Automated Nivometric Station

The nivometric station has been installed around 80 m away from the Gruvebadet aerosol laboratory to collect nivometric data without any physical disturbance. Since its installation, in late 2020, the ANS has been implement over the last years with new sensors, becoming a key research facility for snow research in Ny-Ålesund. The station is composed of an approximately 2 meters high truss with different instruments attached at different fixed heights, that are usually installed during summer when there is no snow. The instruments whose data were available for the analysed 2021-2022 season are [57]:

- A NIR camera with a Sony IMX219 sensor to take pictures of the area under the station and calculate the fractional snow cover area;
- An Ultrasonic Level Sensor (NESA LU06) to measure the snow depth;
- An infrared sensor and six snow thermometers to respectively measure the surface and internal temperature of the snowpack;
- Four sensors to measure the liquid water content (LWC) in the snowpack;
- A shielded thermistor to measure the 2-m air temperature.

Figure 10: **The automated station located at the Gruvebadet site.** Three thermometers are visible one above the other and attached to the rods. The picture has been taken before the reallocation. The NIR camera is visible at the top as well the ultrasonic level sensor just below.

Each of these instruments collected data each 10 minutes except for the NIR camera that takes a picture each hour, and apart some ordinary maintanence, they have been running through the whole year.

The NIR camera has a Sony IMX219 sensor with a resolution of 8 Megapixel. The IR filter has been removed from the sensor and a Storaro blue NIR filter has been added to remove the red wavelenghts and allow only NIR frequencies to reach the sensor.

The Ultrasonic Level Sensor is an instrument used to measure the snow depth. Placing it at a fixed height, that has to be greater than the maximum expected snow height, it emits ultrasonic sound waves toward the ground. Measuring the delay time t_d between the emission of the sound wave and the detection of the reflected one, it is able to quantify the distance from the sensor to the surface below, that could either be soil or snow. The used formula is $h = \frac{1}{2}c_s t_d$, where c_s is the speed of sound. The sensor mounted at the on the ANS is a NESA LU06. It is composed of a piezoelectric transducer mounted inside an aluminium shield to protect it from the radiation and the wind that could disturb the measurement. It has a sensitivity of 1 mm and a response time shorter than 1 s. It is mounted over the station pole, so that the data have to be adjusted subtracting the offset height, that for the 2021-2022 season was 167.7 cm.

The surface temperature is measured by a SOMMER SIR instrument. It is composed of an infrared sensor for the non-contact measurement of the snow skin temperature, mounted inside a stainless steel casing.

The in-depth snow temperature is measured by six NESA Pt100 thermometers placed at different heights from the ground, and mounted at the end of rods attached to the truss, as visible in Figure 10. Since the snowpack doesn't always cover up all the sensors as in Figure 10, some sensors can be buried by the snow, while others could be above it. So only the temperature of the sensors inside the snowpack has to be considered to retrieve the internal snow tempererature profile, and this can be done considering the snow height from the ultrasonic level sensor.
Each snow temperature sensor includes a Resistance Temperature Detector (RTD), made of a 1/3DIN Pt100 wire. The RTD works analysing the changes in resistivity of a platinium wire, built to have a resistivity of 100 Ω at 0 °C. Knowing that the resistivity depends on the temperature, and assuming the sensor to always be in thermal equilibrium with the snow temperature, the latter can be retrieved. The acronym 1/3DIN refers to a precision standard of the sensor, that in this case results to be associated with a ±0.1 °C tollerance at 0 °C. The six thermometers, during the season 2021-2022, were placed at 10 cm, 30 cm, 40 cm, 60 cm, 85 cm, and 110 cm respectively.

The snow LWC is measured by four sensors BITLINE SM-1, installed at fixed heights from the ground at 10 cm, 35 cm, 60 cm, and 85 cm. These sensors work through the Frequency Domain Reflectometry (FDR) method, that measures the dielectric constant of the material interposed between two steel ends. Letting alternate current pass in the circuit created by the two steel ends and closed by the snow, and measuring the operating frequency, the snow dielectric constant can be computed. Since the dielectric constant of water is greater ($\epsilon_{r,water} = 80$) with respect to the one of the snow ($\epsilon_{r,snow} \sim 1$ for dry snow) [58], changes in the water content of the snowpack are easily detectable with this instrument.

The 2-m air temperature is measeured by a NESA TA-C, composed of a 1/3DIN Pt100 wire placed inside a screen to protect it from radiation, still providing natural ventilation. The working principle it's the same of the previous snow temperature sensor.

Snow samples collection

In addition to these automated measurements, weekly snow sample are collected during the snow season. During September 2020 a 10x6 m flat area, about 100 m away from the Gruvebadet laboratory, has been identified to collect the snow samples, and called "Snow Sampling Site". It is represented in Figure 11, where the poles are real poles used as a visual delimitation of the field to avoid accidental contamination.

The collection of samples has been made during the period from November 2021 to June 2022 by CNR operators staying at the Dirigibile Italia Station in Ny-Ålesund. The operators were not the same during the whole period, since each person remains at the station for about 2 months. Anyway, a manual had been redacted by the nivometric station responsible, so that the sample collection, storage, and labelling methods wouldn't change during the whole season.

According to the scheme in Figure 11, a new snowpit is dug by the operators each week, indicated with the acronym "SP_n", where n indicates the progressive number of the snowpit. In this procedure the snowpit exposed all the stratification, from the snow surface down to the ground line.

A maximum of 36 snowpits (hence 36 weeks) are planned in the used scheme, enough to cover the entire snow season, and everything is designed to minimize human contamination and contamination from previous snowpits. For example, as shown in Figure 11, the direction to shovel the snow has been indicated, to avoid to cover future snowpits with contaminated snow. Surely this scheme holds an intrinsic variability due to spatial differences of the snowpits, but the terrain has been chosen to retain the least possible differences.

Each snowpit is dug with prewashed instruments, and after that snow samples are collected using 50 mL plastic vials, every 10 cm in height starting from the ground. The vials are previously washed with Millipore ultrapure water and sonicated. The process is needed since the vials could potentially contain dust or other contaminants on the inner walls, that would pollute the sample, as the expected concentrations are on the order of parts per billion (ppb).

Millipore ultrapure water washing is necessary to avoid any contamination, while sonication is a process that uses ultrasonic frequencies to agitate particles in a sam-

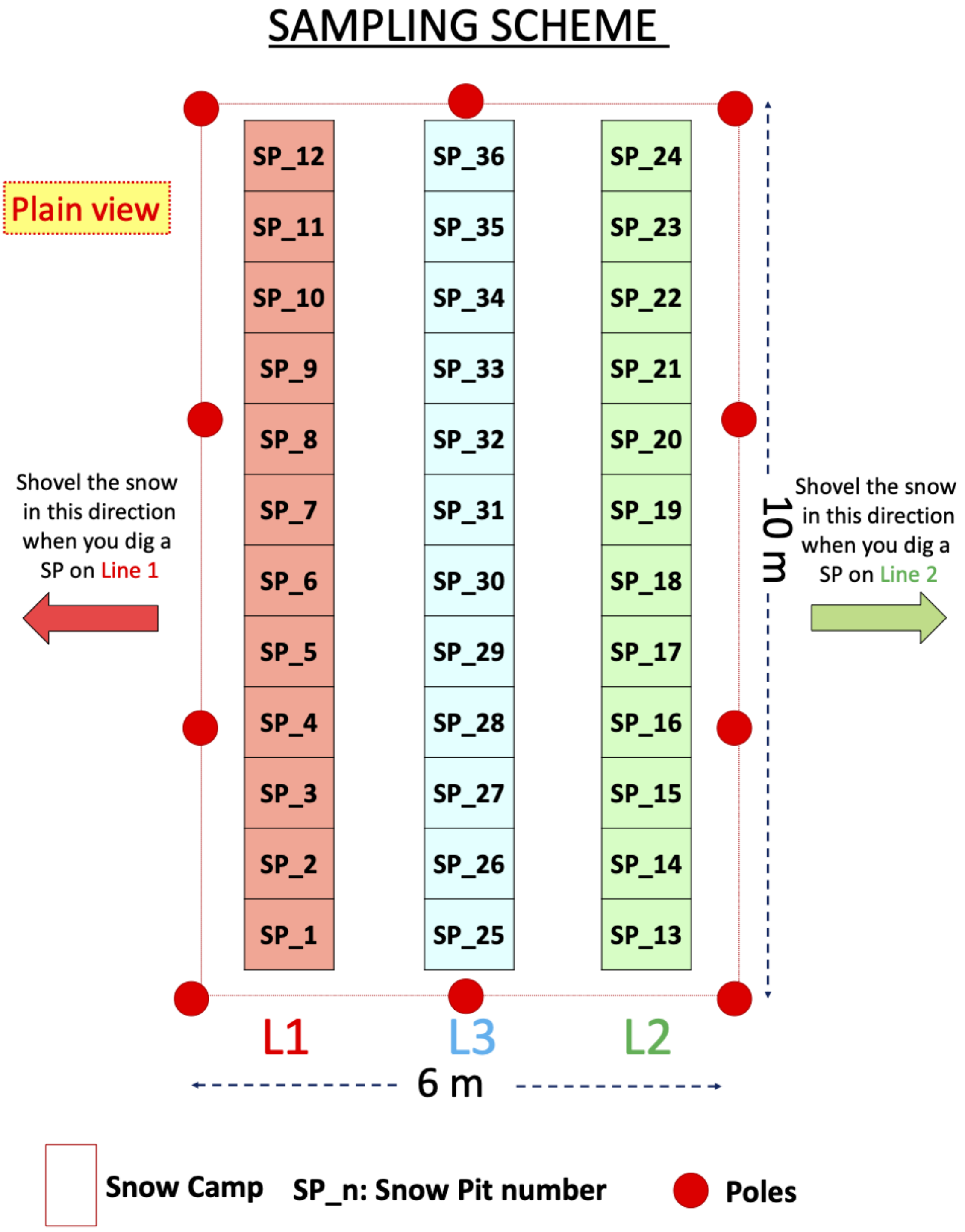

Figure 11: **Snowpit scheme.** The red rectangle represents the sampling field, while each snowpit is identified with "SP_n", where n is a progressive number that identifies the snowpit number. Instructions on the direction where to shovel the snow are reported.

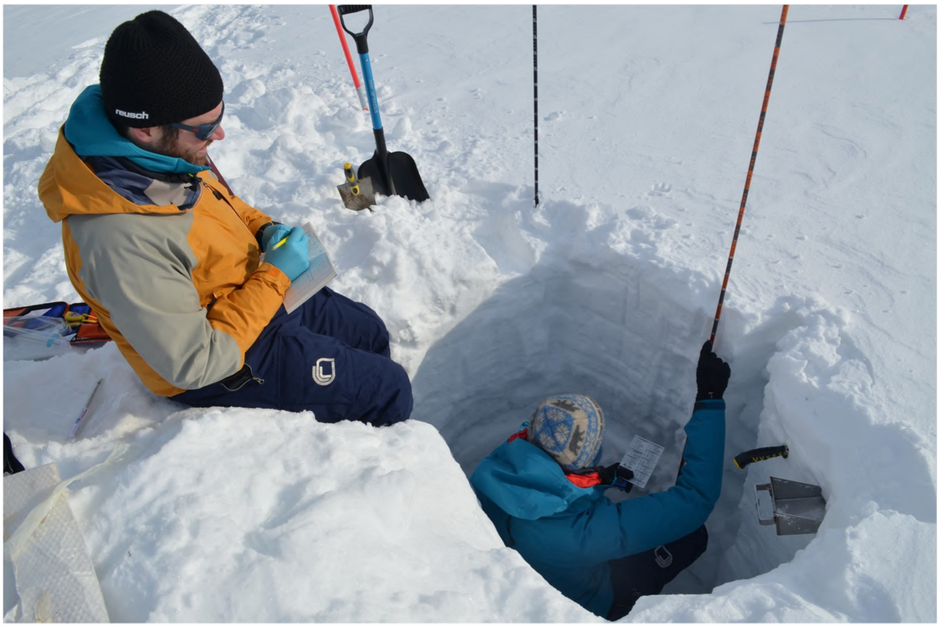

Figure 12: **Picture of a snowpit.** On the right, the snow density cutter and the knife used to measure the snow hardness are visible.

ple and remove them from the vials inner walls. Millipore water is taken from a PURELAB water purification systems. Water purity is usually measured through its resistivity, where higher resistivity indicates higher purity, since most of impurities such as ions allow a better conductivity, and with the resistivity of the used water reaches $18.2\,\mathrm{M\Omega\cdot cm}$. For comparison, distilled water has a resistivity of $500\,\mathrm{K\Omega\cdot cm}$, tap water about $5\,\mathrm{K\Omega\cdot cm}$ and sea water $30\,\Omega\cdot\mathrm{cm}$ [59]. In addiction, other precautions are used, such as the use of clean gloves to handle instruments and vials. Once each snow sample is collected in the labelled vial, the snowpit number and the collection depths are recorded. All the samples from a snowpit are grouped into a single plastic bag, on which the collection date and the snowpit number are written. The snow height is indicated starting from the ground, so that in case the total snowpack height results 26 cm, three samples will be taken. The first one will sample the layer starting from the surface and ending at 20 cm, and will be labelled as "20-26". The other two will be labelled "10-20" and "0-10". In addiction to the sample collections, other physical snow parameters are recorded, using other instruments:

- Snow Mass
- Snow Volume
- Snow Hardness
- Snow Temperature

Snow mass and volume are obtained using a metallic cutter that withdraws a standard volume of snow from a layer, usually $1000\,\mathrm{cm}^3$ or $250\,\mathrm{cm}^3$. The instrument is weighted both before the snow collection, obtaining the tare, and after the snow collection, obtaining the gross weight. The net weight divided by the cutter volume gives the snow density in kg/m^3. From these parameters also the Snow Water Equivalent (SWE) can be computed through the conservation of mass, assuming complete snow melting thanks to Equation 1.2, so that the SWE results to be measured in mm.

The snow hardness, as said in section 1.2.1 follows an international 6-steps scale, called the HH index scale, and is measured trying to make different objects penetrate in the snow layer (either a knife, a pencil, etc. see Table 2). Snow temperature is measured with a manual needle probe thermometer every 10 cm, at the boundary between each layer, starting from the bottom.

Once all the samples for the snowpit are collected, the snowpit is filled up again, paying attention not to affect the future planned snowpits. Once the samples are brought back to the station, they are frozen and at the end of the season they are shipped to the Venice headquarters of CNR-ISP to be analysed. A total of 224 samples were collected for the 2021-2022 season.

2.2 Sample chemical analysis

Since the analysis instrument cannot work with the 50 mL sampling vials, smaller 1.5 mL vials had to be washed and sonicated in advance to accomodate the samples, with the same methods used for the sampling vials. After being washed, the vials are left to dry up under an extractor hood as in Figure 13a, so that any liquid residue can evaporate. After they are completely dry, they are grouped in plastic bags previously washed with ultrapure water, and stored until the next phase.

(a) **Drying vials.** The 1.5 mL vials with the caps were left for some hours in a laminar flow cabinet to dry.

(b) **Sample storaging.** The freezer where all the 50 mL vials with the samples are stored.

(c) **Sample melting.** Snow samples are left under a laminar flow cabinet so that they can melt.

Figure 13: Pictures from the CNR-ISP laboratories that show different processes in preparation for the analysis.

Since the snow samples are frozen and stored in freezers (Figure 13b), the first step requires to let them melt for some hours under a laminar flow cabinet as in Figure 13c, until all the solid phase is gone, and only the liquid one remains. In the meantime, the 1.5 mL vials can be prepared, writing on them a unique code that identifies the snowpit (uniquely linked to a date) and the depth of collection. The used code in this case was "GVB_abc", where "GVB" identifies the Gruvebadet site, and "abc" represents a progressive three-digit number used to identify the date and the layer height. To do this, a correspondence page has been prepared to relate each number to a date and layer.

When the snow samples are completely melted, they are ready to be transferred into the smaller 1.5 mL vials, under a laminar flow cabinet, to avoid contaminations. Each sample vial is opened, the right amount of melted snow is manually transferred to the correspondent small vial, and both are closed. Once all the analyses vials have been filled up, they are stored in other plastic bags and frozen again in dark conditions, so that no major chemical reaction could happen, that could modify the ions concentrations.

2.2.1 Ion chromatography

The instrument used for to analyse the samples is a ion chromatographer, also called ion-exchange chromatographer. The instrument has not been directly used, but the data have been kindly provided by Dr. Elena Barbaro, the CNR-ISP researcher who did the analyses. Ion chromatography is a technique that allows the separation and the examination of ions in a sample, based on their *affinity* to another compound, called *ion exchanger*. The technique was set up in 1947 by F.H.Spedding and J.E.Powell to separate rare-earth elements, but the method evolved during the years, with some big interest developed during the Manhattan project, during the World War II. Around 1975 it started to be used to analyse drinking water and to study environmental problems, and it is still used to analyse different compounds concentrations in water [60].

The method is based on a ion exchange chromatography matrix (also called stationary phase or ion exchanger) that consists of a material, usually a resin, containing both positive and negative ions. This matrix is stored inside a glass column, called chromatographic column, inside which the sample is poured. There are different kinds of matrices, based on the type of ion that they exchange, anions or cations.

Figure 14 show how the process works. The chromatographic column initially contains only the stationary phase, colored in light blue. When the sample (also called mobile phase) is released at the top of the column, it starts to flow toward the bottom of the column. The distinct constituents of the sample move at different speeds vertically depending on how much they are attracted by the ions in the resin, a property called *affinity* with the matrix. The ions with lower affinity move faster in the column, while the ones with greater affinity move slower, as they get slowed down by the matrix, resulting in the last part part of Figure 14, where the three components of the sample result separeted.

At the bottom end of the column, an electrical conductivity detector is placed, to measure conductivity through time in a graph called chromatogram, as shown at the bottom of Figure 14. When each ion reaches the end of the column, a peak of conduc-

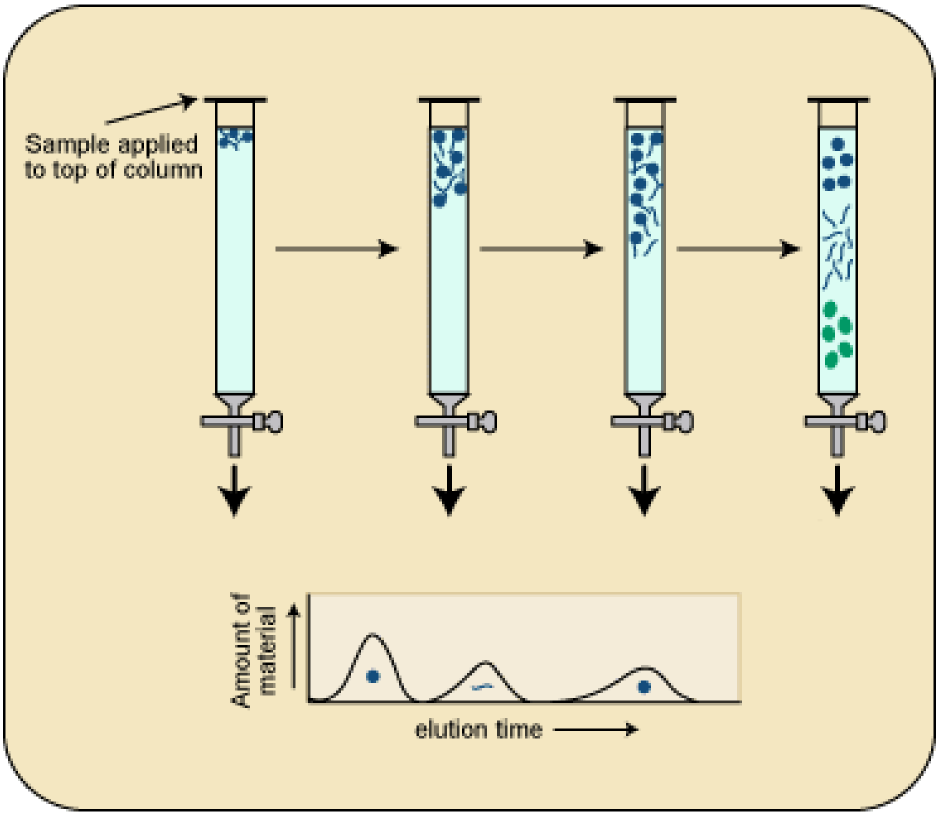

Figure 14: **Principle of working of a ion chromatographer.** The sample is applied at the top of the chromatographic column and slowly descends separating in the different compounds. When each one arrives at the bottom, it produces a signal in the chromatogram, shown at the bottom of the picture. Diagram by Madison Area Technical College. Copyright 2006 by the Biotechnology Project at MATC.

tivity is measured by the detector, as the ions conduct the electricity much better than neutral matrix. As a result, different peaks will be produced in the chromatogram, each one corresponding to the different ions of which the sample is composed. Knowing the matrix used in the chromatographic column, the different peaking times can be associated to distinct ions, and the integral of the area under each peak can be computed to associate a concentration to each ion, thanks to a prior calibration [61].

Since the correspondence between area under each peak and ion concentration can vary through the operational life of the instrument, it is a good practice to calibrate the intrument outputs at each use. To do this, particular samples called *standards*, are prepared in advance. Standards are solutions with known concentration of each element. They can either be multi-element standards, meaning that a single sample contains a known concentration of many elements (usually the same concentration for all, for simplicity), or single-element standards, meaning that only one element is added to the solution.

Usually, at least 5 standards are preparred, to match the likely concentration ranges that will be found in the sample analysis. For the most abundant elements, such as Na or Ca, additional multi-element standards with higher concentration are prepared. Other elements with lower expected concentrations are usually not included to avoid the instrument saturation. For example a standard could contain 500 ppt (parts per trillion) of each element to analyse, the second one 1 ppb (parts per billion), the third one 5 ppb, and so on.

These standards are analysed with the real samples, and when the instrument outputs are available, the calibration curves are be built, so that they can be used to associate the area under each curve with the real concentration of each compound.

2.3 Synoptic and weather data

Synoptic meteorology is a branch of meteorology interested in large-scale weather, with an horizontal spatial scale around thousands of kilometers. This discipline is mainly interested in understanding the genesis and the development of large-scale phenomena, such as weather fronts, tropical and extra-tropical cyclones, or anticyclones. Since these weather features can span thousands of kilometers and last some days while moving, it is hard to well retrieve their features from puntual weather stations, and a better way to study them is through satellites. Indeed, as previously mentioned in Section 1.3, reanalyses constitute a very good method for large scale studies, as they can provide data for large areas and long periods of time, combining models and observations.

Zooming in to the local scale, the in-situ conditions will be analysed through the use of stations located in Ny-Ålesund or in close proximity. Different types of stations will be included, starting from a Norwegian weather station, to the Italian Climate Change Tower, that collects radiation data. At the end, additional analyses will be carried out using different data sources, such as the MODIS satellite imagery to follow the sea ice evolution, or a snowpack model to see how well it can describe the snowpack evolution and detect the event effects.

Using data from all these sources, this work aims to understand the genesis, the development, and the effects of the March 2022 ROS event.

2.3.1 ERA5 reanalysis

Reanalyses are tools that allow to obtain meteorological and climatic data about the past, combining observations with results from meteorological models, in order to provide meteorological variables on a 2D or 3D grid, at hourly intervals. There are many available reanalyses, based on different models, criteria, and scope of use [62]. The ERA5 reanalysis is a project created by the European Centre for Medium-Range Weather Forecasts (ECMWF), and it is used in this work since it is one of the most commonly used for large-scale global applications, and since it has already been used in some university courses. The first ECMWF reanalysis product, published in 1995, was called ERA-15, and included about 15 years, from 1978 to 1994 [63]. In 2003 the second product was presented, called ERA-40, making available about 45 years of data, from 1957 to 2002 [64], and after it, ERA-Interim, that covered the years from 1979 to 2019.

In 2019 the most recent ECMWF reanalysis product, called ERA5, was released. ERA5 presents a very high resolution of 0.25° (ERA-Interim has a resolution of about 79 km), and covers the years from 1950 up to now [65], with variables available on hourly intervals. Atmospheric variables are computed on 137 levels, from the surface up to 80 km [66].

ERA5 comprehends an Integrated Forecasting System (IFS) that includes a data assimilation system and a numerical model of many components of the Earth system. The data assimilation system merges the latest weather observations with up-to-date forecasts that cover the places on Earth without observations, so that it creates a precise approximation of the current state of the Earth system. Then, the numerical model combines the results with other Earth system components, such as the oceans. With this framework, the complete model is able to recreate the evolution of the atmosphere and the other components.

All the available ERA5 products can be downloaded from the Copernicus Climate Data Store website, `https://cds.climate.copernicus.eu/cdsapp#!/search?type=dataset`, choosing the appropriate dataset and then filling a form with the requested variables and associated characteristics. Through a proper code, the variables can be plotted on a global or regional map. Through this reanalysis, the large scale of the event will be studied, and different variables have been downloaded to this purpose. Considering the Northern Hemisphere, the geopotential at 500 mbar and the total column water vapor (TCWV) have been retrieved from the website, in order to study the synoptic conditions and eventually identify atmospheric rivers, through a specifically designed algorithm [67].

Since this algorithm has been developed to work on the whole globe, it has also been used to identify an eventual atmospheric river in this work. The algorithm was adapted to work with the available data-The method works as following. From the ERA5 reanalysis the Integrated Vapor Wapor (IVW) product is retrieved, that is the total amount of water vapor present in a vertical atmospheric column. In this case the product has been retrieved for a 15-days interval around March 16 (from March 9 to March 23, with data twice a day, at 00:00 and 12:00) of the year 2022, for the whole Northern Hemisphere.

The same product with the same characteristics has been retrieved for a climatology of the same days, with years from 1991 to 2022. For each grid point and temporal step of the 2022, only the IVW values that exceeded the 85th percentile of the climatic IVW distribution (of that specific grid point and date) were considered, while the ones that dind't exceed the threshold were masked out and set to zero. In this way only the anomalous IVW values for the period are identified.

To ease the AR identification, the maximum IVW value for each latitude at each time step is identified and marked with a red dot. The final identification of the AR, that was automatized in the article, was made manually for this work. If the marked points follow a long and narrow structure, then the event is identified as AR. The result, showed as an example for the 23rd March 2022 at midday, is showed in Figure 15.

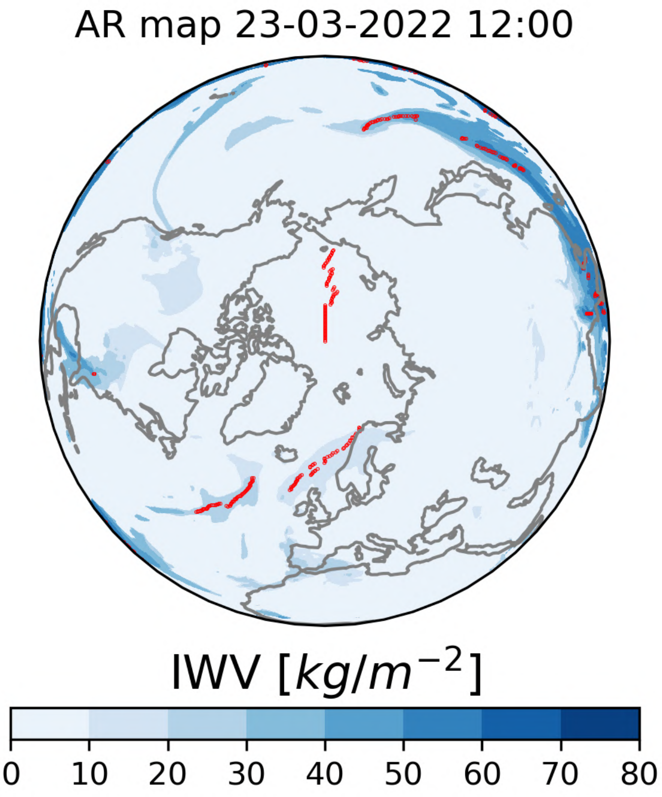

Figure 15: **Example of the algorithm output, 23 March 2022.** The masked out values are set to zero while the maximum values fo each latitude are marked with a red dot. A large and almost zonal AR is visible south of Japan.

CARRA reanalysis

Climate change effects are visible in the whole world, but the Arctic results one of the most vulnerable areas. The peculiar characteristics of the region, with large surfaces covered by snow and ice, together with specific weather patterns and phenomena, led to the creation of an Arctic-specific reanalysis, called Copernicus Arctic Regional Reanalysis (CARRA).

Through the use of satellite data, specific surface observations, and high resolution orographic maps, the final product allows a 2.5 km spatial resolution, that is the main advantage over the ERA5 reanalysis, that is anyway used to apply lateral domain boundaries to run CARRA. Moreover, CARRA better represents Arctic weather extremes, and performs better where the small-scale topography is important, such as close to mountains or coastlines. Over flat and wide surfaces, such as large ice sheets or over the ocean, the differences between CARRA and ERA5 become smaller [68].

The CARRA products are provided over two distinct domains. The west domain (CARRA-West) comprehends Greenland, Iceland, and Svalbard, while the east domain (CARRA-East) mainly comprehends Svalbard and Scandinavia [69]. While Svalbard is included in both domains, the east one has been used because the archipelago resulted in a more central position.

This reanalysis has been used to retrieve variables with a high spatial variability, that in this case are the total precipitation, the precipitation type, and the sea surface temperature. These CARRA products will allow the study of variables whose investigation would be impossible without an high-resolution reanalysis.

2.3.2 HYSPLIT

While reanalyses can give a high quality information about the meteorological configuration, no detailed information can be obtained about the movements and the origin of air masses, even if it is fundamental to understand the creation of particular meteorological events and the source of compounds found in the snowpack.

The Air Resources Laboratory (ARL), under the National Oceanic and Atmospheric Administration (NOAA), offers a tool to solve this problem, called Hybrid Single-Particle Lagrangian Integrated Trajectory (HYSPLIT) model. This atmospheric model is able to model and simulate the movements of air in the atmosphere, both on local and global scales, considering both horizontal and vertical movements, and offering different features to work with [70]. In order to provide a very good model, HYSPLIT includes physical and chemical processes, such as dispersion, chemical transformation and deposition process.

Day of March	$\overline{CBH}$ [m]	σ_{CBH} [m]
15	683	327
16	642	319
17	960	818
18	1241	1000

Table 3: Mean cloud base heights, with associated standard deviation, as computed from the ceilometer data [71].

In addition, both forward and backward trajectories can be simulated, meaning that air masses movements can be either predicted in the future, for example to predict the destination of particles originated in an event, or retrieved in the past, starting from a target location. While the first feature is useful for example to predict where certain pollutants, that may derivate from a fire, or radioactive particles, may end up days or weeks after an event, the latter one allows to retrieve the past path made by an air mass arriving on a place at a specific time. This is useful in atmospheric chemistry to establish the source of chemical compounds and aerosols found in-situ [70]. Anyway, for the sake of this work, only backward trajectories are used, to retrieve the origin of the air masses associated with the ROS event.

HYSPLIT is called "Hybrid" since it is a hybrid model, whose mechanism falls in between the Lagrangian approach, that uses a frame of reference moving with the particle of interest, and the Eulerian one, that uses a still frame of reference. The model must run with meteorological data that are already provided on the website, although more detailed data can be manually provided for more precise results. For this analysis, the meteorological data from the website were used.

Since HYSPLIT offers back-trajectories starting from three heights above a specific location, it's useful to know the height of the air mass of interest, in order to have be more plausible results. In this case, the cloud base for cloud formations present during the ROS event have been retrieved by the PANGAEA database `https://doi.pangaea.de/10.1594/PANGAEA.942331`, where a dataset of cloud base heights above the Ny-Ålesund station is available with data ranging from August 2017 to November 2022. The data have been measured by a Vaisala CL51 laser ceilometer that measures each minute the cloud base heights (CBH) up to 13 km [71].

The ceilometer works through a principle called Light Detection and Ranging (LIDAR). A laser with wavelength of 910 nm is sent vertically from the surface, and the cloud-scattered signal that comes back is analysed to detect clouds layers. The Vaisala CL51 model has a range of detection up to 13 km for cloud profiling, with a resolution of 10 meters [72].

For the days of interest, mean daily CBHs, $\overline{CBH}$, with relative standard deviations σ_{CBH} have been computed and reported in Table 3. Looking at these results, it has been decided to use 500 m, 1000 m, and 2000 m as starting heights for the HYSPLIT model.

2.3.3 Ny-Ålesund weather station

To effectively estimate the event effects on the local scale, local data are needed. In fact, between the meteorological parameter, precipitation is one of the more spatially variable, and it's important to retrieve in-situ data to correctly analyse the event and its effects. Being under the Norwegian sovereignty, data from the weather station located in Ny-Ålesund are available on the Norsk Klima Service Senter (Norwegian Centre for Climate Services) website `https://seklima.met.no/`, that still provides data for many stations all around Norway.

The station used in this work is located in Ny-Ålesund, at the coordinates 78.9218 °N, 11.9325 ^{O}E, at 8 m above sea level. It started recording data on the 26th July 1974 [73], and it is part of the WMO weather station network, with the identification number 1007. The station is maintained by the Alfred-Wegener-Institut (AWI), a German research institute for polar and marine research.

The station has been used to retrieve 2-meters air temperature, wind speed and direction, and 10-minutes cumulated precipitation. The wind speed and direction are measured by an FT702LM air flow sensor, produced by FT Technologies. The sensor works analysing the phase of an acustic wave emitted by three transducers, so that wind speed and direction can be computed. Since the relation depends on temperature, pressure, and humidity, corrections for these parameters are made. The resolution of the wind speed is 0.1 m/s and 1 for the wind direction [74] [75].

The air temperature is measured by a Vaisala HMP45C probe, that measures both the air temperature and the relative humidity. Temperature measurements are made through a 1/3DIN Pt1000 wire, that works as the one mounted on the Gruvebadet station [74] [76].

The precipitation measurements are made through a OTT Pluvio2 Version 400, where the number 400 represents the collection area in cm^2. The pluviometer measures every 6 seconds the weight of the collecting bucket over a scale with a water equivalent resolution of 0.01 mm. Removing the weight of the empty bucket, the weight of the precipitation is found. The rim of the top opening is heated to include solid precipitation [77] [78].

2.3.4 Climate Change Tower

Another weather station installed in Ny-Ålesund is the Amundsen-Nobile Climate Change Tower (CCT). The station is run by the italian CNR-ISP, and it's a key structure for different international studies. The tower was inaugurated on 30th April 2009 with the aim to study meteorological variables in the lower part of the troposphere. The research tower is 34 meters tall and it includes different measurements at four heights: 2 m, 5 m, 10 m, and 34 m. At each one of these heights, temperature, relative humidity, wind speed and direction, are measured.

In addition, radiation fluxes are measured by three different radiometers. At 33 m a Kipp and Zonen CNR1 net radiometer measures both incoming and outgoing shortwave (SW) and longwave (LW) fluxes from which the albedo is computed, while at 25 m two other radiometers measure the outgoing SW and LW fluxes. The SW fluxes are measured by a Zonen first class CM11 Pyranometer, while the LW ones by a Kipp & Zonen CG4 pyrgeometer.

The albedo and the radiative downward intensities have been downloaded from the Italian Arctic Data Center `https://data.iadc.cnr.it/erddap/index.html` [79]. The SW radiation mainly includes the solar component of the radiative budget in the atmosphere, with wavelengths up to 4 µm, while LWs mainly include infrared radiation emitted by the surface, clouds, or atmosphere. At the station other variables are measured that won't be used in this work, such as atmospheric pressure, snow height, snow temperature, heat fluxes, and aerosol distributions [80].

Since weather data have already been retrieved from the SEKlima station, only radiometric data have been fetched from the CCT. Data have been downloaded for the whole month of March.

2.3.5 Zeppelin Observatory

In addition to weather and radiometric data, also chemical data can give indications about the local processes, as well as hints about lont-scale air masses transport. The Zeppelin observatory is a Norwegian research station located close to the top of the Zeppelin Mountain, about 2 km south of Ny-Ålesund, shown in Figure 16. Opened in 1990, it is the northern Norwegian research station. The scientific activities are carried on by the Norwegian Institute for Air Research (NILU).

Figure 16: **The Zeppelin observatory as seen from the Zeppelin mountain top.** Ny-Ålesund is the city on the left. Photo by Advanced Global Atmospheric Gases Experiment [81].

The station measures the concentration of many different gases in air, with specific focus on greenhouse gases. The station data are used by many global networks, included the Global Atmospheric Watch (GAW), or the Arctic Monitoring and Assessment Programme (AMAP) [82].

Data are public and available at the website `https://ebas-data.nilu.no/`, and all the available chemical compounds for March 2022 have been retrieved. These data will help in understanding how chemical compounds in the air are transported, how they react to these events, and how long they are affected by them.

In addition, a webcam is mounted at the station, whose pictures taken every 10 minutes are public and stored on the Norsk Polarinstitutt website [83]. The camera points to Ny-Ålesund and to the mountains on the other side of the fjord, so that the pictures will help in understanding the real conditions of the city and of the snowpack before, during, and after the event.

2.3.6 MODIS

Satellite data are useful to analyse the properties of atmosphere, land, and ocean. The Moderate-Resolution Imaging Spectroradiometer (MODIS) is a scientific instrument installed on both Terra and Aqua NASA satellites, respectively launched in 1999 and 2002. MODIS is able to collect radiation intensities on 36 different spectral band, both in shortwave and longwave intervals, and with spatial resolution of 250, 500, or 1000 m depending on the band [84].

The spectral bands range from 0.4 µm to 14.4 µm, hence including both SWs and LWs. Four differents methods of calibration are included on the satellites, as well as a view to space. Calibration is important to convert the instrument output to a radiation intensity, and different methods are used for different spectral regions. The two satellites that carry on the MODIS instrument, Terra and Aqua, move in a polar sun-synchronous orbit, meaning that they pass from any point at the same local solar time each time, so that the illumination conditions remain always similar over each location.

An archive of the satellite images can be found at `https://worldview.earthdata.nasa.gov/`, where selecting a specific day, all the imagery from MODIS can be shown. Using the Corrected Reflectance (True Color) product, cloud-free days can be selected. This product provides so-called natural color images, since they result similar to what the human eye would see. They are made using MODIS channel 1 (0.62 – 0.67 µm) as red, channel 4 (0.54 – 0.57 µm) as green, channel 3 (0.46 – 0.48 µm) as blue, and combining them to obtain the final images. Through these images, the sea ice concentration will be studied.

Moreover, the radiation intensities signal from all the channels will be used to study the effect of the event on the snow albedo and emission over a 3 km x 3 km region close to Ny-Ålesund.

2.4 Energy Balance Snow Model

Numerical models are computer simulations that try to replicate real physical processes, to provide data that no one may have, such as the height of the snowpack in all the locations in Svalbard. Since these models are not perfect, they always have to be validated bt real data, when available, to assess how well it behaves in reproducing real processes.In this perspective, if the model results significantly differ from the observation, an opportunity arises to acknowledge the model's weaknesses, to include more processes, and to improve it.

Snowpack modelling is an important tool to understand the vertical evolution of snow physical properties, such as temperature, density, or water content. In this framework, Prof. Ward van Pelt, senior lecturer in physical geography at Uppsala University, Sweden, has developed a model for firn evolution, called "Coupled Energy Balance – Firn Model" (EBFM) [85] [86]. The model has also been updated to include seasonal snowpack processes, and called Energy Balance - Snow Model (EBSM). While the EBFM code is available online, the one for EBSM has not still been published, but thanks to a collaboration between CNR-ISP and Prof. Ward van Pelt, it has been requested to run the model in the Ny-Ålesund area, to compare its results to the nivometric station observations.

The model couples an energy balance and a multi-layer snow models to simulate the evolution of the snowpack, through the use of meteorological inputs either from reanalyses or in-situ data [85]. The two models are coupled so that melt water production at the surface is used as an input by the multi-layer model to simulate storage, refreezing, or percolation [85].

The surface energy balance models considers the following equation to compute the energy available for melting:

$$Q_{melt} = SW_{net} + LW_{net} + Q_{sens} + Q_{lat} + Q_{rain} + Q_{sub} \tag{2.1}$$

where SW_{net} and LW_{net} are the net shortwave and longwave radiations respectevely, Q_{sens} and Q_{lat} are the turbolent and latent heat fluxes, Q_{rain} is the heat transferred by the rain, and Q_{sub} is the heat flux toward the ground [85]. The snowpack internal model is based on the SOMARS model (Simulation Of glacier surface Mass balance And Related Subsurface processes) developed in 1994 [87], and comprehends a modelization for heat transfer, compactation due to gravity, percolation, refreezing, and runoff of melted water [85].

The output variables are the snow density, the snow temperature and the irreducible water content. The last one is a particular variable that will be explained following. When some water, either from precipitation or melting, does not entirely refreeze in a layer, the remaining amount of water continues the descent still in liquid form toward the ground. Another small amount of water, called irreducible water, is indeed held in place by capillary forces, so that it remains in the layer. In the model the irreducible water content is computed as a function of the porosity, while water vertical percolation is stopped only by an ice layer [85].

For this simulation, meteorological data have been retrieved from the Norwegian reanalysis NORA3 [88] on the Ny-Ålesund area, and used to simulate the snowpack evolution from the 1st October 2021 to the 1st May 2022.

Chapter 3

Results

3.1 Synoptic analysis of the event

Following the order of the topics in Chapter 2, synoptic data are here presented. The aim of these data is to visualize the ROS event on the large scale, understanding the geopotential configuration, visualizing the presence of major synoptic structures, and understanding where the air mass that produced the rain came from.

3.1.1 ERA5

In Figures from 17a to 17d the geopotential height at 500 mbar is represented every two days starting from March 12 and ending on March 18. The lower geopotential height area in green represents the region where the cold polar air is trapped, and comparing it to Figures 6a and 6b, a weak configuration of the polar vortex is noticeable in all the plots. In fact, in those days the polar vortex created two major low pressure systems, one more intense that the other, that are found over the Baffin Bay and over Siberia, Russia. As shown in Figure 17a, the weakening of the polar vortex allows higher pressure and hence warmer air to intrude poleward from Scandinavia. Subsequenlty, the low pressure system over Canada moves a little eastward toward Greenland and intensifies, creating the configuration in Figure 17c.

On this day, March 16, a very steep pressure gradient created over Svalbard. Thanks to this synoptic configuration, a corridor is created, through which air masses can be easily and quickly transported northward from mid-latitudes. Just after a couple of days, in Figure 17d the corridor doesn't exist anymore, and the polar vortex slowly recomposes itself, moving the major low pressure system over the North Pole again.

Having seen the possible path through which the humid air that created the ROS event passed, it is now interesting to take a look to the atmospheric water vapor content that could have driven such event. Using the TCWV product from the ERA5 reanalysis, the algorithm described in Section 2.3.1 has been applied, resulting in Figures from 18a to 18d. The results are presented for the entire Northern Hemisphere, each

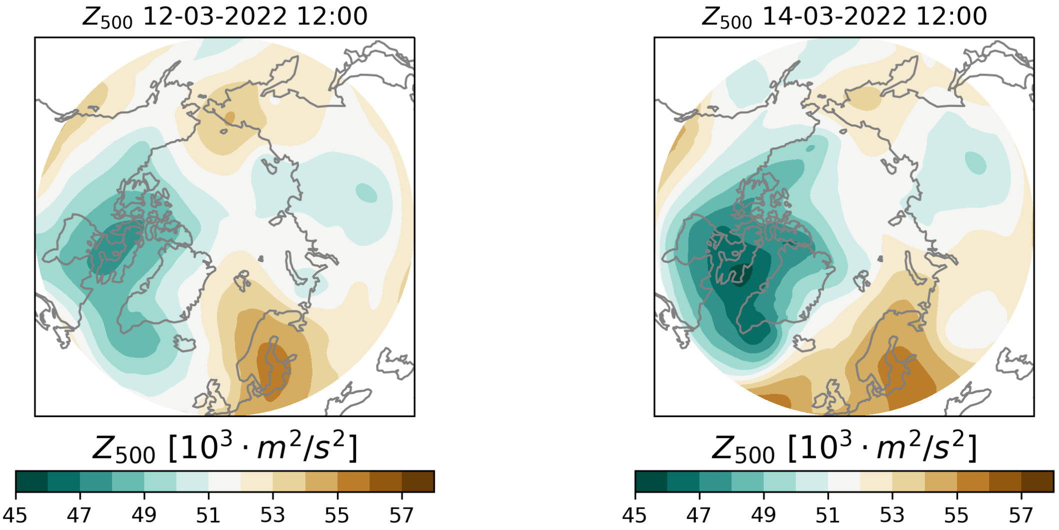

(a) **Geopotential configuration** on the 12th of March 2022, 12:00.

(b) **Geopotential configuration** on the 14th of March 2022, 12:00.

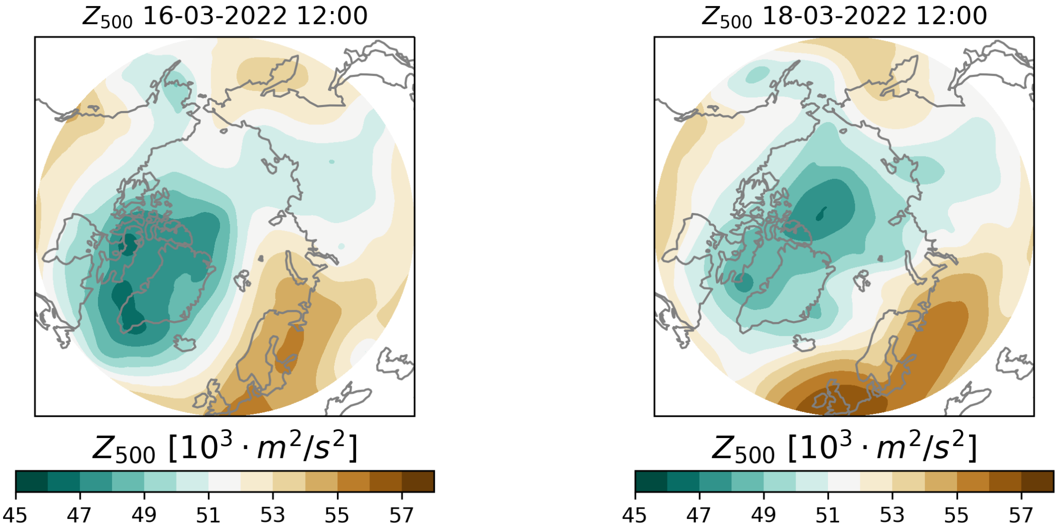

(c) **Geopotential configuration** on the 16th of March 2022, 12:00.

(d) **Geopotential configuration** on the 18th of March 2022, 12:00.

Figure 17: Geopotential height at 500 mbar in different days around the event.

day at midnight from March 14 to March 17. Referring to the algorithm, all the grid points where the TCWV didn't exceeded the 85th percentile have been set to zero in the plots. Then, the maximum TCWV value for each latitude has been marked with a red dot to visually recognize the atmospheric river. The red dots don't automatically identify the AR, and a manual visual inspection is required to check the real presence of the structure. It is clear that, starting from March 14, a very well defined atmospheric river extends starting from mid latitudes, around the Mexican Gulf area, and reaching Greenland. As time passes, the AR stretches eastward and northward, until March 16 when it discharges most of the water on Svalbard, quickly weakening and dying out on the days after, as shown in Figure 18d.

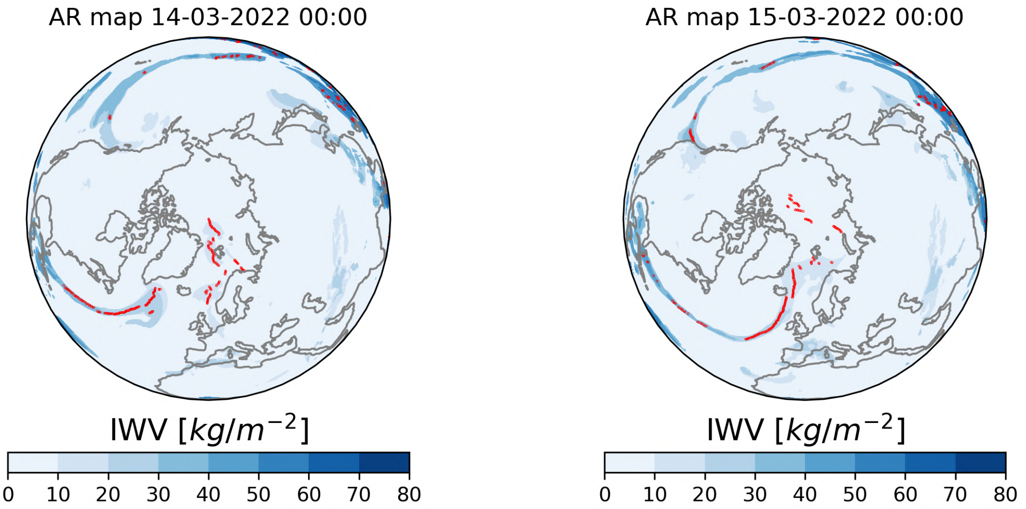

(a) **AR detection** on the 14th of March 2022, 00:00.

(b) **AR detection** on the 15th of March 2022, 00:00.

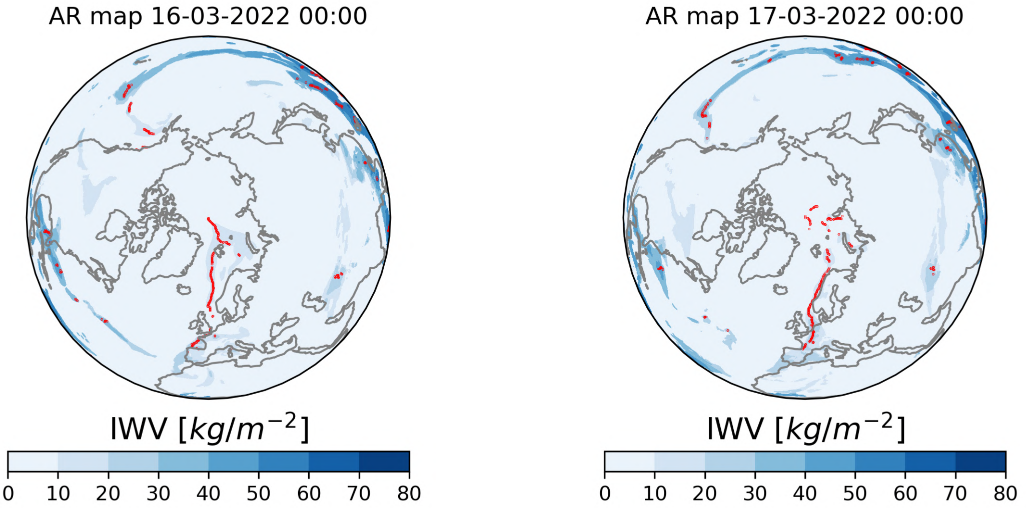

(c) **AR detection** on the 16th of March 2022, 00:00.

(d) **AR detection** on the 17th of March 2022, 00:00.

Figure 18: Maps obtained through the AR detection algorithm, showing the northern hemisphere on different days around the event.

3.1.2 HYSPLIT

Here the backtrajectories obtained from the HYSPLIT model are presented. Three runs have been made. The first one, in Figure 19, considers backtrajectories starting from March 16 at midnight, from three differents heights, 500, 1000, and 2000 meters above Gruvebadet station (above ground level, AGL). As previously explained in section 2.3.2, these heights have been chosen analysing the data from a ceilometer located in Ny-Ålesund. From this run it is visible how all the considered air masses come from South-South-West, from a region above Scotland, passing over the Norwegian Sea (between Norway and Iceland) on the day before the event.

The second run, in Figure 20, has been made considering just one height, 1000 m AGL, but with different starting time for the backtrajectories. Six different starting times have been considered, from March 18 at midnight to March 16 at midday, every 12 hours. This run has been made to analyse the provenance of the different air masses in time, and to check if the ROS event is identifiable.

In the third run, in Figure 21, an ensemble of 27 trajectories is generated for the same point, starting from 1000 m AGL on midnight of March 16. The HYSPLIT ensemble is generated randomly shifting the meteorological variables of one grid point horizontally and of $0.01\,\sigma$ vertically, where $\sigma = \frac{p_s}{p}$ is the ratio between the surface pressure and the pressure at a certain height.

3.2 Physics of the snowpack

Having evaluated the synoptic configuration that led to the ROS event, the local effects in the Ny-Ålesund area can now be analysed. In this section, the physical properties of the air and the snowpack, are reported, from the nivometric station in Gruvebadet. In Figure 22 the black line represents the snow height as retrieved from the Ultrasonic Level Sensor. It is visible how the snow height gradually increases throughout the year, with growths in correspondence of multiple snowfalls, followed by a slower snow metamorphism and compaction (although wind drift cannot be exluded), that led to a reduction of the snowpack height. Colors ranging from blue (sub-zero temperatures) to red (positive temperatures) in Figure 22 represent the air and snowpack temperature recorded in the snow season.

As described in Section 2.1, the thermometers were placed at 10 cm, 30 cm, 40 cm, 60 cm, 85 cm, and 110 cm. Since the snow height never reached the two highest thermometers at 85 cm and 110 cm, their data have been discarded. The second thermometer from the bottom, the one at 30 cm, constantly recorded a temperature with a positive bias of 2 or 3 °C compared to the ones measured right below and above. Due to this, the data from this thermometer have been excluded from the analysis. However, a routine check will be done in summer 2023, when the snow melting will allow an inspection of the instrument. Considering only the measured temperatures

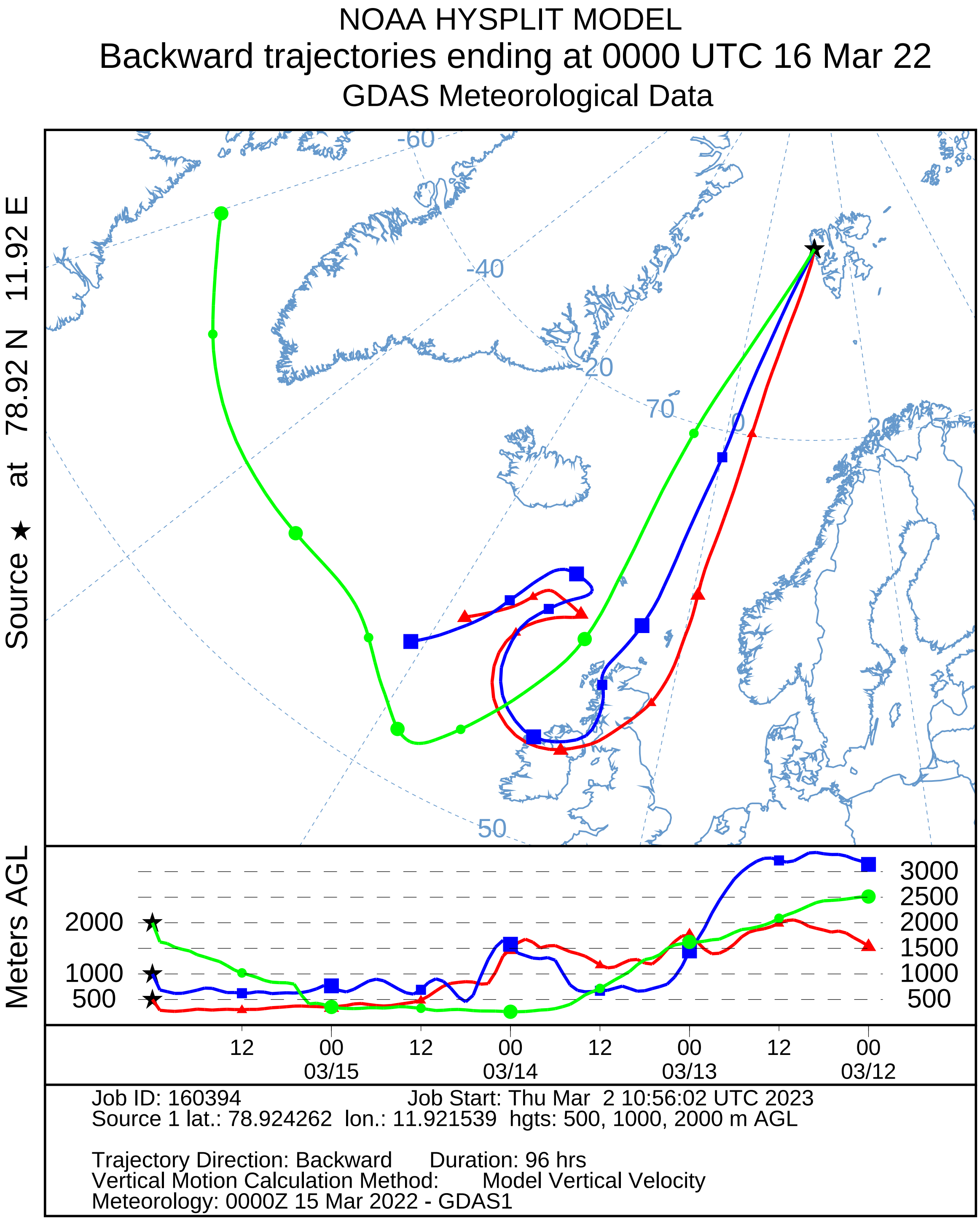

Figure 19: **HYSPLIT model backtrajectories for three differents heights**. The trajectories start on March 16 at midnight and go back for 4 days, starting from 500, 1000, and 2000 meters above Gruvebadet station. All the trajectories go 96 hours (4 days) back in time.

from the instruments inside the snowpack and the skin temperature, a vertical linear interpolation has been made in order to retrieve the complete vertical profile every

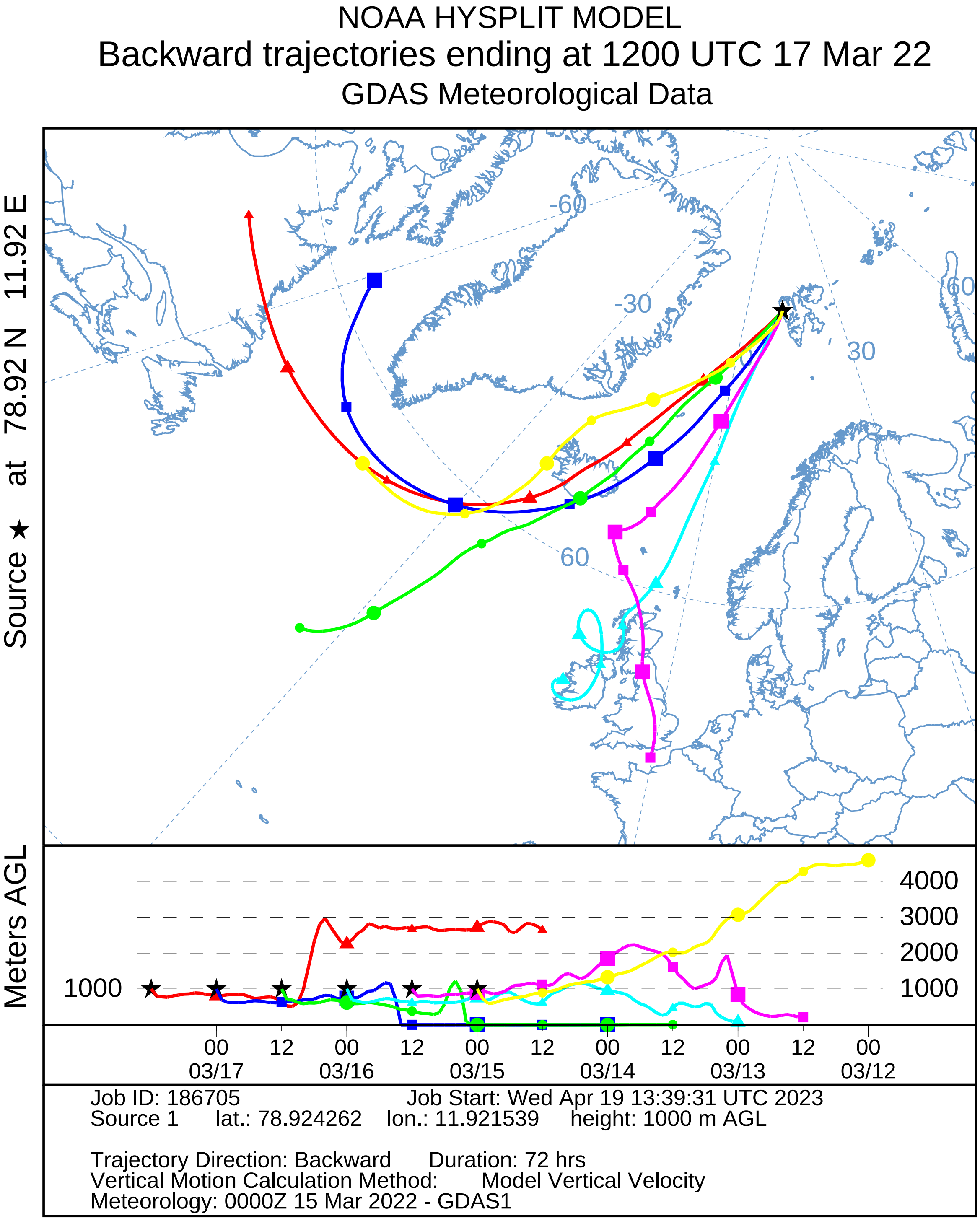

Figure 20: **HYSPLIT model backtrajectories starting in different times**. The trajectories start on March 18 at midnight every 12 hours, for a total of 6 trajectories. Each one starts from 1000 meters above Gruvebadet station. All the trajectories go 96 hours (4 days) back in time.

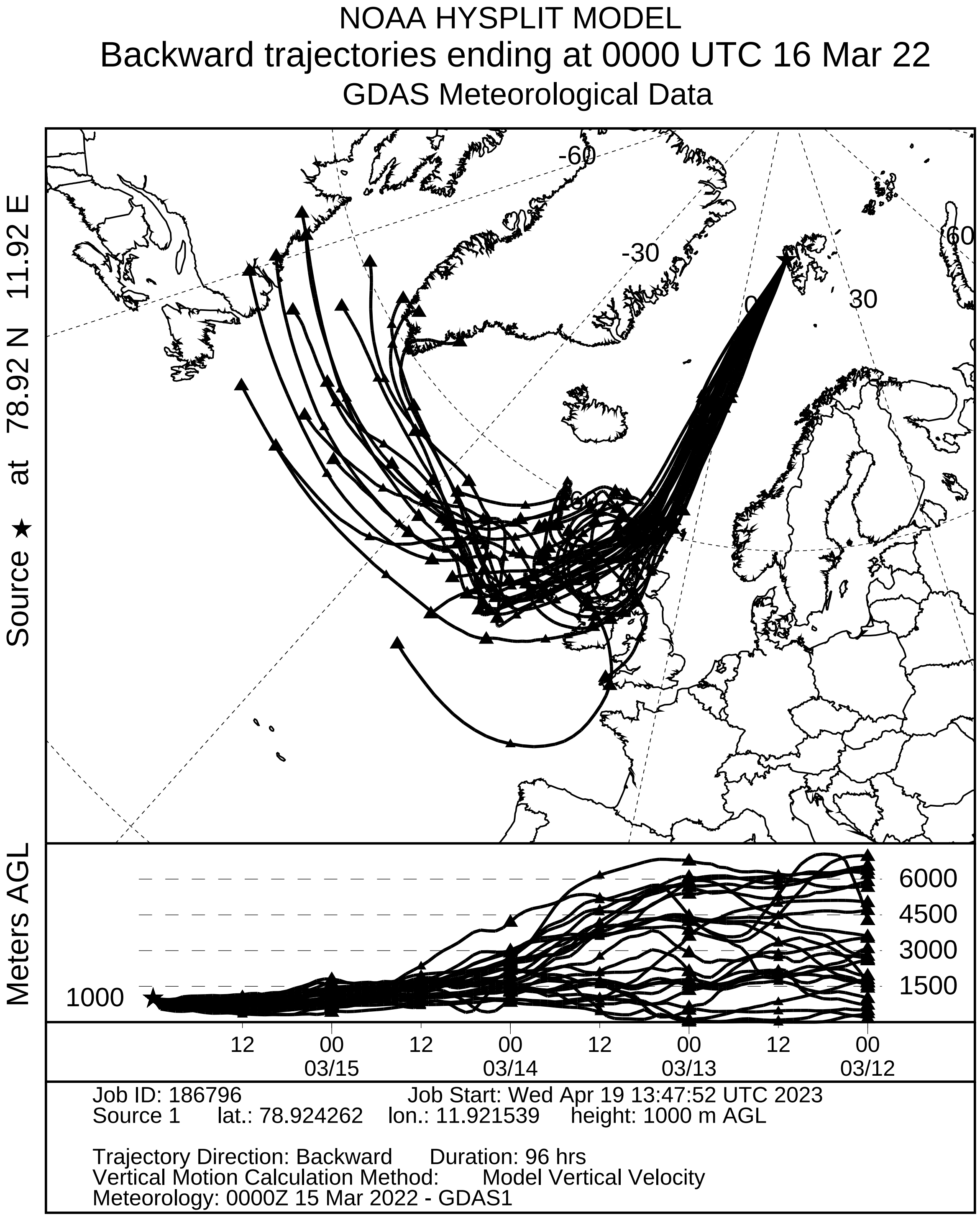

Figure 21: **HYSPLIT model ensemble backtrajectories**. The trajectories start on March 16 at midnight from 1000 meters above Gruvebadet station, and an ensemble is used to produce a total of 27 backtrajectories. All the trajectories go 96 hours (4 days) back in time.

10 minutes.

Above the snow height line, the air temperature measured from the dedicated sensor has been reported with the same color scale used for the snowpack. As said, red air temperatures indicate above zero temperatures. The red region starting at the end of May represents the arrival of the summer season, when all the snowpack quickly becomes isothermal at 0 °C and melts.

In Figure 23 a zoom of March 2022 has been made, to highlight the behaviour of snow temperature during the analysed ROS event. It is visible how, starting from March 13, the air temperature quickly increased up to $3-4$°C, immediately raising also the snow skin temperature. The internal temperature instead takes some days to increase, reaching 0 °C on March 16, probably due to rain percolation and heat transfer. Due to the snowpack thermal inertia, the internal temperature remains at 0 °C until March 22, with slightly different timings depending on the depth.

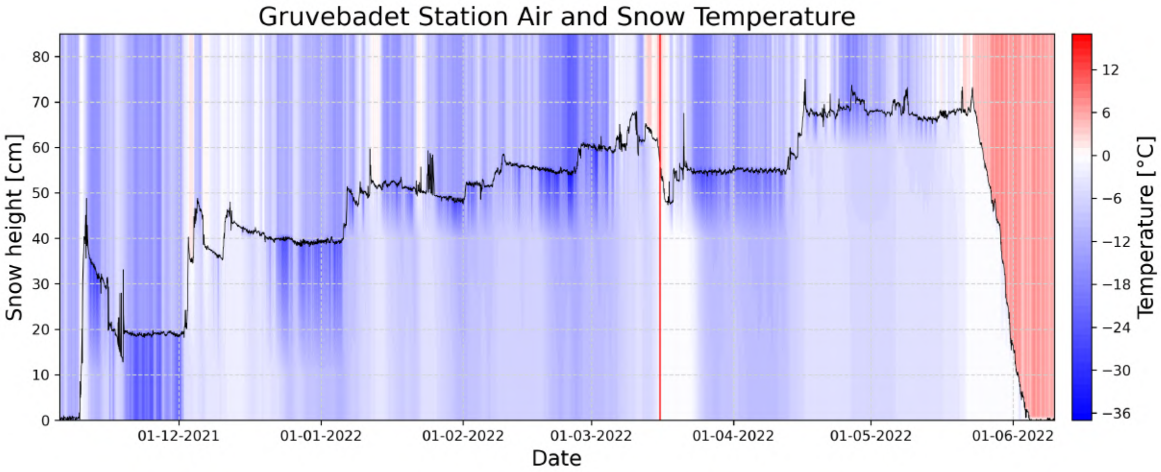

Figure 22: **Temperature vertical profile for snowpack and air measured by the Gruvebadet ANS.** In black the snow height, while in blue to red shades the air temperature, above the snow height boundary, and below it, the snow temperature. The temperatures around 0 °C are represented with whiter shades. March 16 at midnight is identified by a red vertical line.

Then, processed with the same methods of Figures 22 and 23, the LWC in the snowpack is presented in Figures 24 and 25. The sensors were placed at 10 cm, 35 cm, 60 cm, and 85 cm, and only the ones totally confined within the snowpack have been considered. From Figure 22, it is clear how the two events that increased the snowpack temperature during the whole year are the ROS event of March 16 and the melting season respectively. In Figure 25 a zoom around the event has been made, with midnight of March 16 marked with a vertical red line. It is visible how the rain reaches the lower layers (the sensor at 10 cm) some hours after midnight, and quickly saturated the lower snowpack up to the first 35 cm, where the second sensor is placed. Then, after about two days, the snowpack was completely free of liquid water.

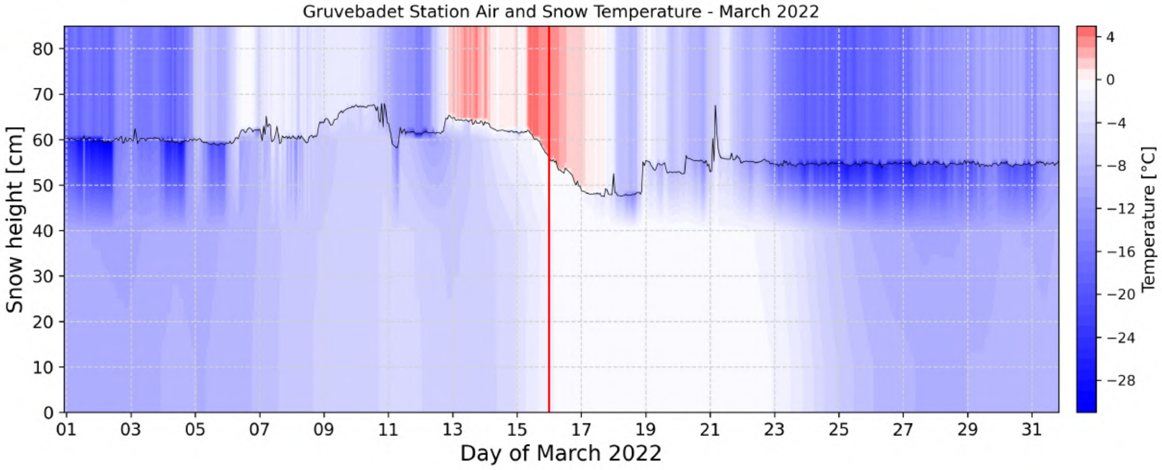

Figure 23: **Temperature vertical profile for snowpack and air measured by the Gruvebadet nivometric station, in March 2022.** March 16 at midnight is identified by a red vertical line.

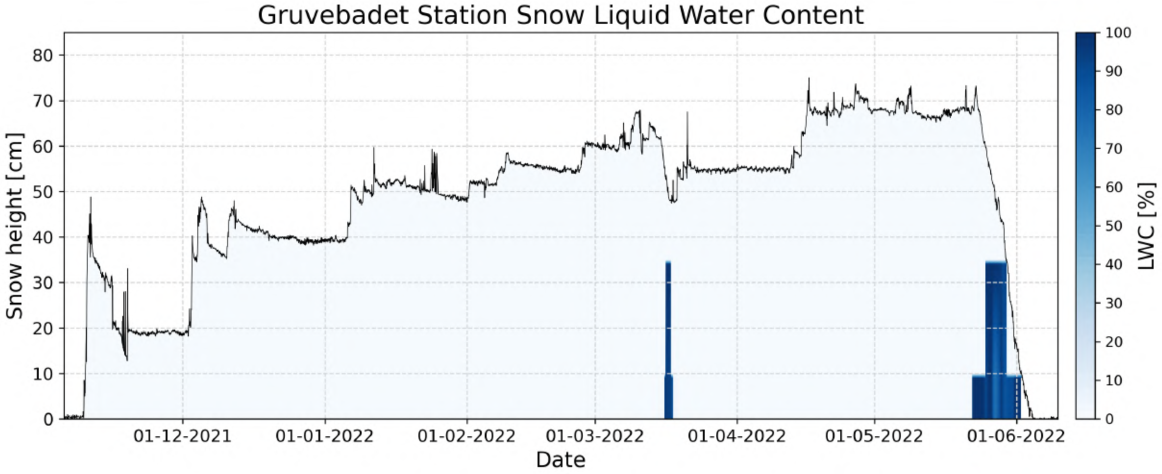

Figure 24: **Liquid Water Content vertical profile for snowpack measured by the Gruvebadet nivometric station.** In black the snow height, while in blue the LWC with values from 0 to 100.

In Figures 26 and 27, the measured density and the relative SWE calculation obtained from the snowpits are shown. Since the two quantities are strictly linked by equation 1.2, they follow the same distributional pattern, except for layers shorter than 10 cm, such as some of the superficial ones. In the plots there are some blank cells as the samples may have been missing or not analysed, but they are not close to the event.It is visible that before the event an internal denser layer exists between 20 cm and 30 cm, with some less dense layers above. Right after the ROS event, from the snowpit done on March 22, a denser layer is visible on the surface, probably due to refreezing. On the second snowpit after the event, on March 29, a thick and very

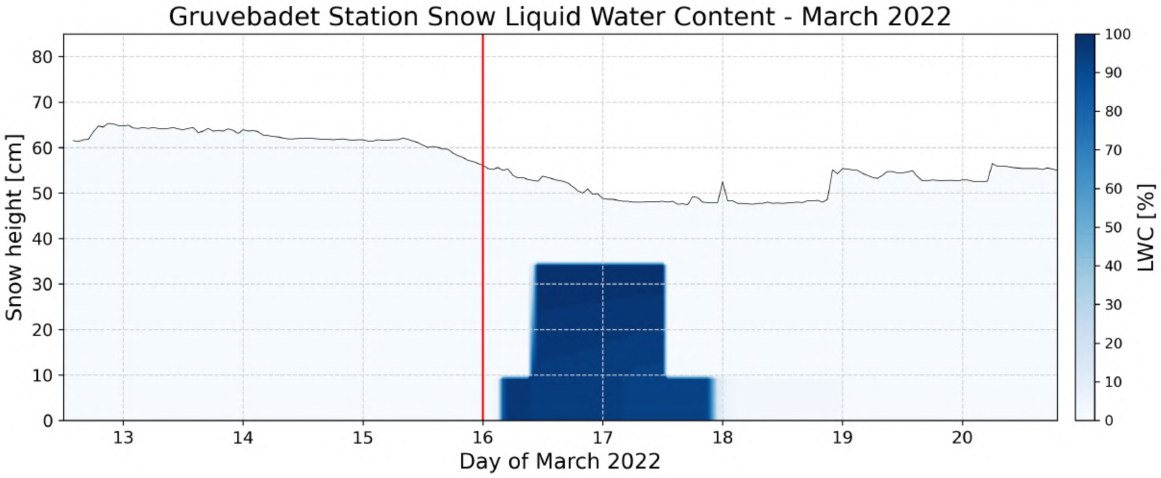

Figure 25: **LWC vertical profile for snowpack measured by the Gruvebadet nivometric station, in March 2022.** March 16 at midnight is identified by a red vertical line.

dense layer appears from the ground up to 40 cm. Afterwards, the vertical density profile becomes more homogeneous and at the start of the melting season, the density approaches very high values, due to presence of liquid water. These changes will be further discussed in Section 4.

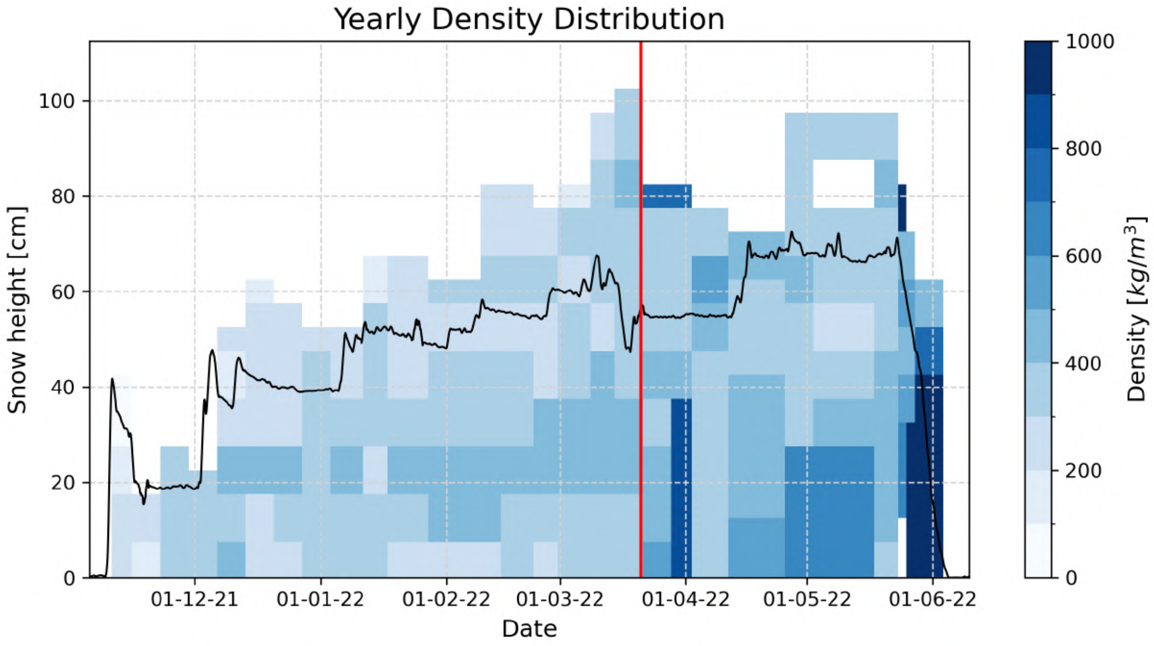

Figure 26: Density vertical and temporal distribution as measured with the snowpits. The red line identifies the date of the first snowpit after the event.

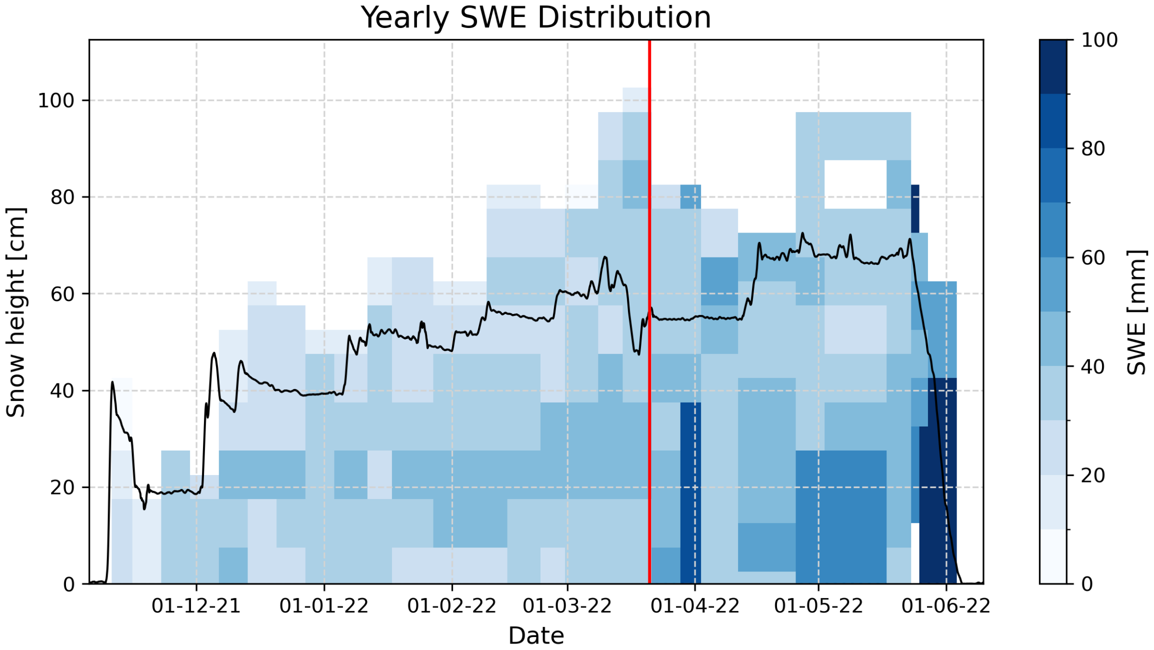

Figure 27: SWE vertical and temporal distribution as measured with the snowpits. The red line identifies the date of the first snowpit after the event.

3.3 Chemistry of the snowpack

The results obtained by the ion chromatography analyses, regarding the snow samples from the snowpits, are now presented. These result in the chemical concentrations vertical profile of different compounds through the year. In Figures from 28e to 28n the vertical and temporal distribution of different chemical compounds is shown. The black line represents the snow height. Each colored cell represents a snow sample, that stands for a specific snowpit (hence date) and snow layer (hence height from the ground). The left border of the cell is set at the snowpit date, while the right border is placed on the date of the following snowpit. Similarly, the bottom border of each cell is placed at the bottom height of the snow layer where the samples was taken, and the top border at the top height of the same layer. Then, each cell has been filled with a color that identifies the measured concentration of the represented chemical compound as found from the ion chromatography, with a color scale that varies for each compound, as they can span different ranges.

The date of the first snowpit after the event, that has been done on March 22, is marked with a red line. This line therefore separates the snowpits of March 15 (just one day before the event), and March 22. The different chemical concentrations between these two snowpits can help in understanding how the event modified the chemical profile of the snowpack. It is already visible how some elements, such as Ca, K, or Methane Sulfonic Acid (MSA), present a high concentration on the top (surface) layer right after the ROS event. Others, like acids (C1 Formic, C2 Acetic, C2 Glycolic, C2 Oxalic) or Br, do not present such pattern, and the possible reason will be discussed in Section 4.

Many discrepancies are visible between the snow height measured by the automatic sensor and the maximum height found from the snow samples. The possible reason for this is the spatial variability between the snowpit position and the snow depth sensor. While the first one could have accumulated wind-drift snow on the top, the sensor could suffer from percolation of water from the tower where it is installed (in Figure 10 a small depression around the tower is visible), that leads to an underestimation of the snow depth. As for the previous snowpit data, some blank cells are present.

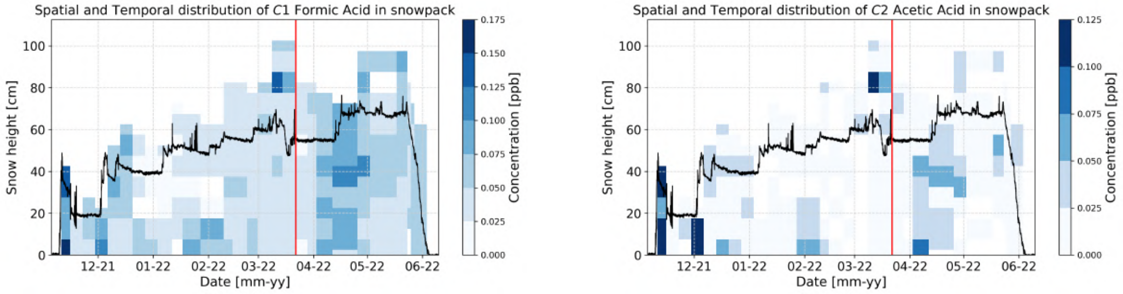

(a) C1 Formic acid in the snowpack.

(b) C2 Acetic acid in the snowpack.

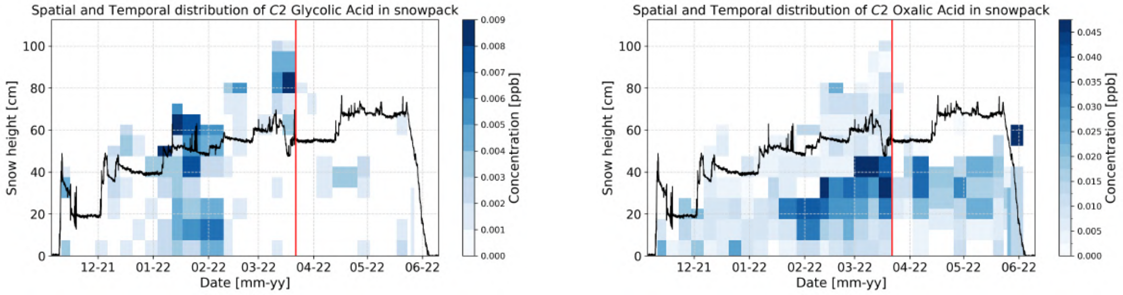

(c) C2 Glycolic acid in the snowpack.

(d) C2 Oxalic acid in the snowpack.

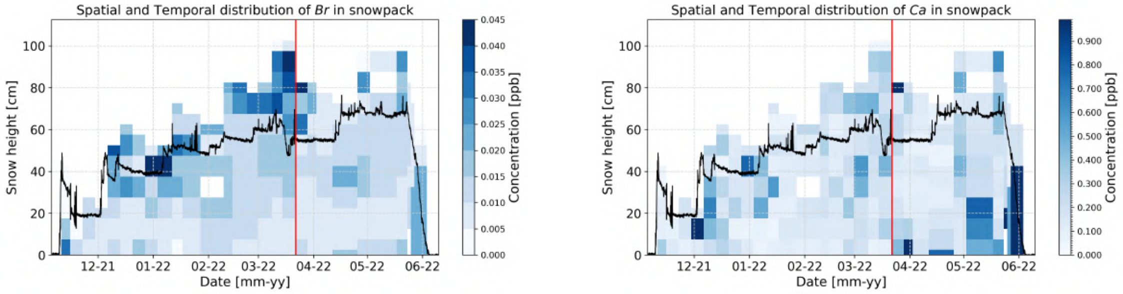

(e) Br in the snowpack.

(f) Ca in the snowpack.

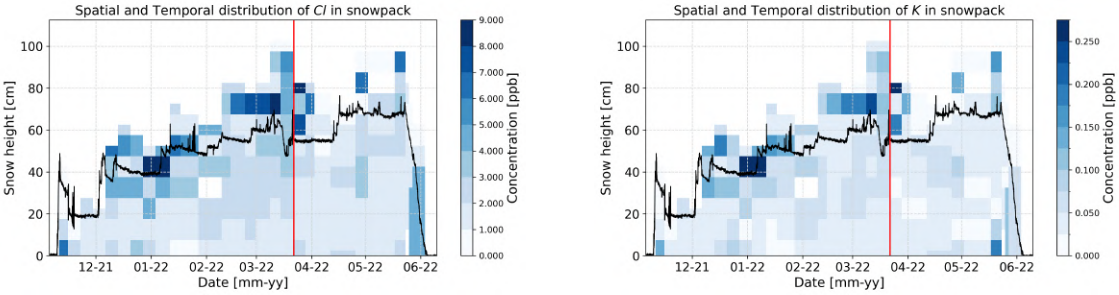
Spatial and Temporal distribution of *Cl* in snowpack

Spatial and Temporal distribution of *K* in snowpack

(g) Cl in the snowpack.

(h) K in the snowpack.

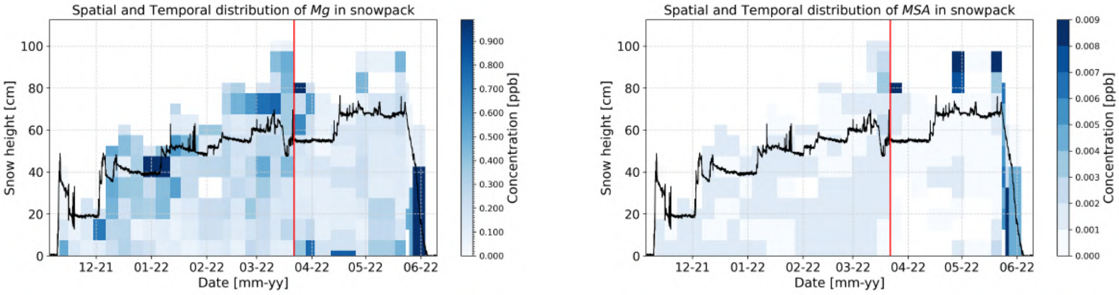
Spatial and Temporal distribution of *Mg* in snowpack

Spatial and Temporal distribution of *MSA* in snowpack

(i) Mg in the snowpack.

(j) MSA in the snowpack.

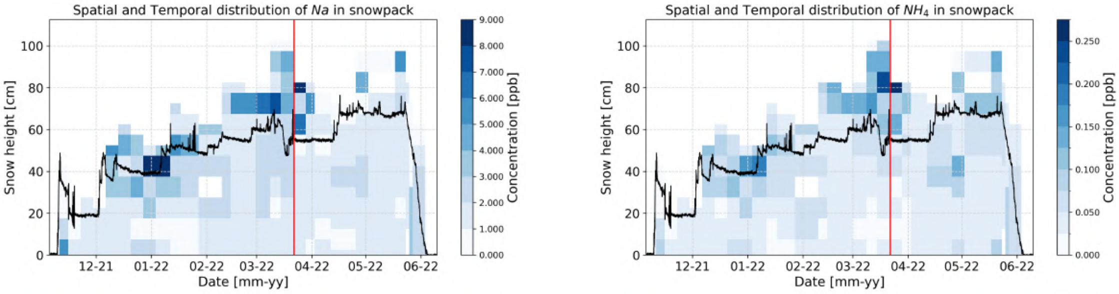
Spatial and Temporal distribution of *Na* in snowpack

Spatial and Temporal distribution of *NH₄* in snowpack

(k) Na in the snowpack.

(l) NH_4 in the snowpack.

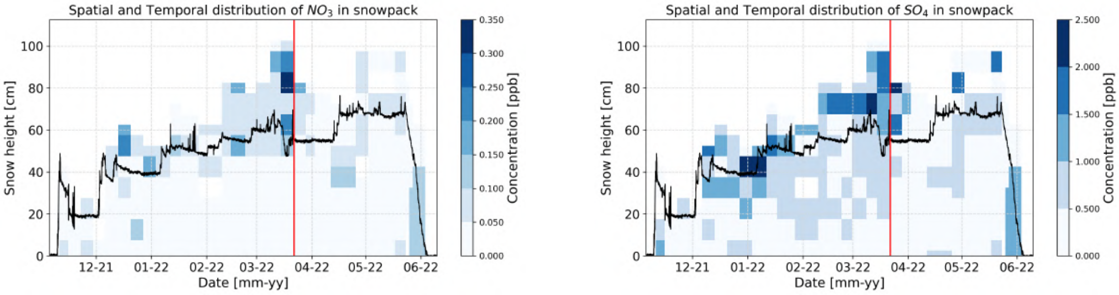
Spatial and Temporal distribution of *NO₃* in snowpack

Spatial and Temporal distribution of *SO₄* in snowpack

(m) NO_3 in the snowpack.

(n) SO_2 in the snowpack.

Figure 28: Spatial and temporal distribution of the analysed chemical compounds in the snowpack. The vertical red line indicates the separation date between the last snowpit before the event and the first one after it.

In the following plots, from Figure 29e to 29n, the load for each compound is represented. The load of an element is computed as the vertical integration of a compound concentration in a single snowpit, as following:

$$\text{Load}(t) = \sum_{i=0}^{N(t)} C_i(t) \cdot h_i(t) \tag{3.1}$$

where the load of a certain snowpit Load(t) is computed as the sum for all the N layers i of the layer concentration $C_i(t)$ times the layer thickness $h_i(t)$. Since the blank cells are far from the event date, they do not perturb the analyses.

Through this variable, the temporal evolution of the total amount of a compound in the snowpack can be followed, and it can be checked if the total amount decreased or increased with the ROS event. In this case, it can be seen that a general decrease for each compound is present after the event, and the result will be discussed in Section 4.

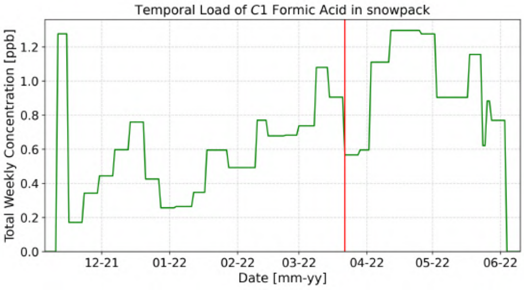

(a) Temporal load of C1 Formic acid in the snowpack.

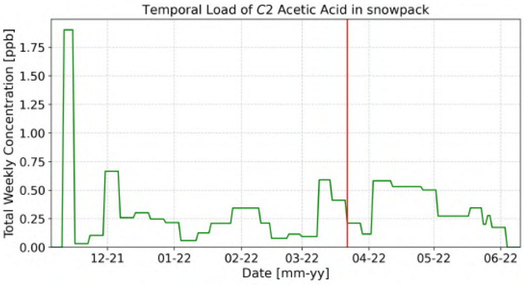

(b) Temporal load of C2 Acetic acid in the snowpack.

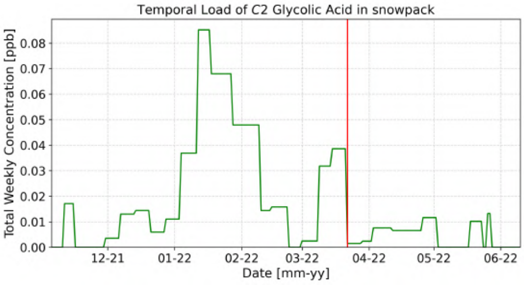

(c) Temporal load of C2 Glycolic acid in the snowpack.

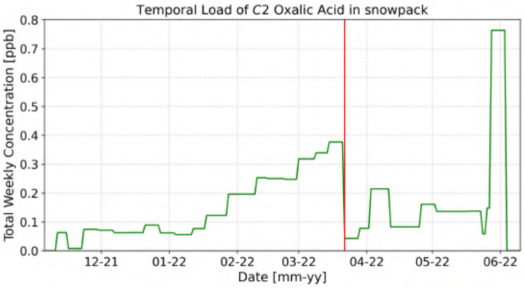

(d) Temporal load of C2 Oxalic acid in the snowpack.

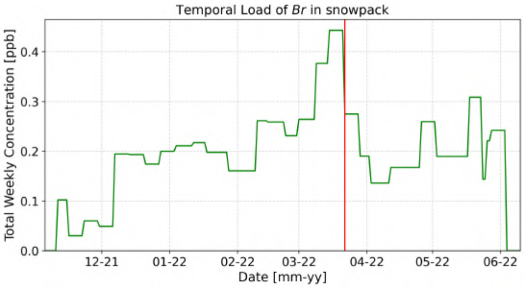

(e) Temporal load of Br in the snowpack.

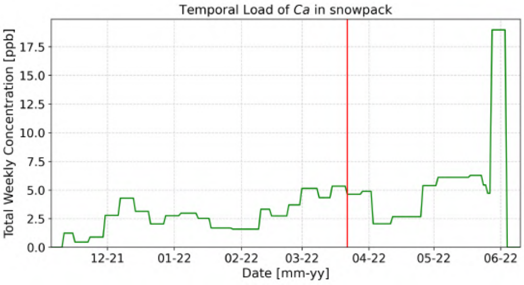

(f) Temporal load of Ca in the snowpack.

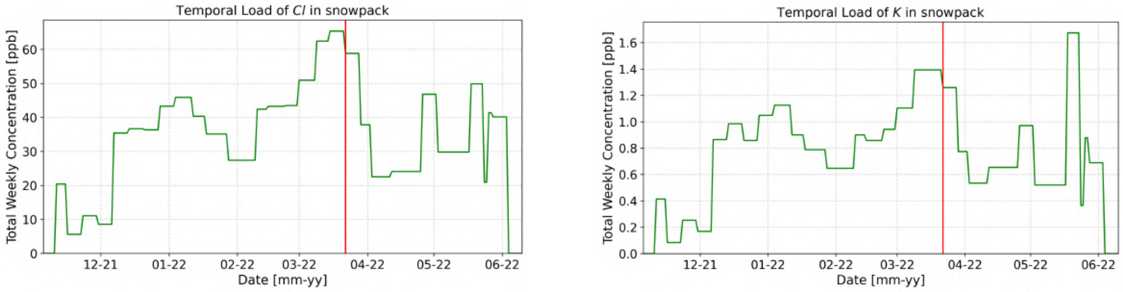

(g) Temporal load of Cl in the snowpack. (h) Temporal load of K in the snowpack.

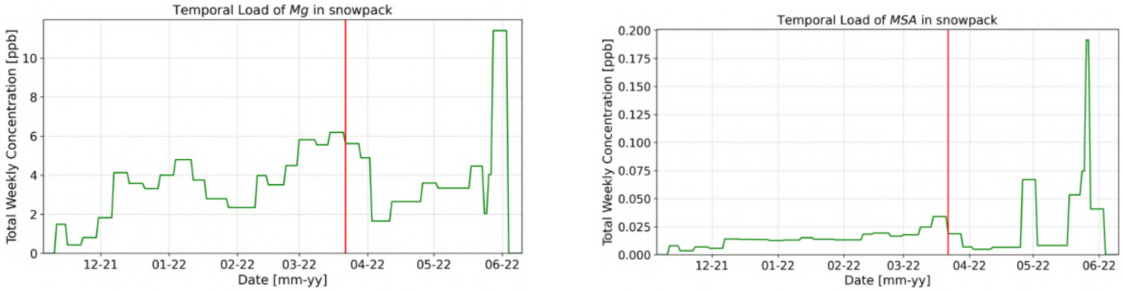

(i) Temporal load of Mg in the snowpack. (j) Temporal load of MSA in the snowpack.

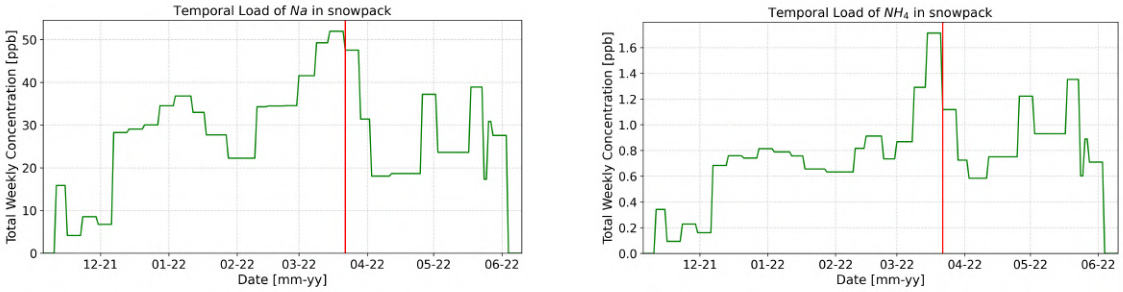

(k) Temporal load of Na in the snowpack. (l) Temporal load of NH_4 in the snowpack.

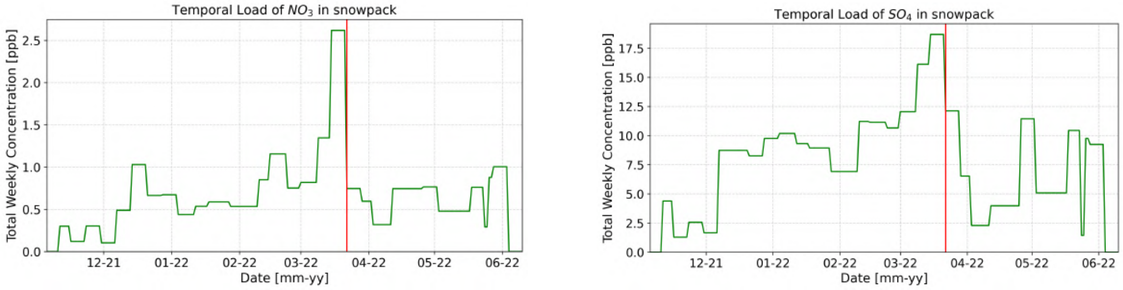

(m) Temporal load of NO_3 in the snowpack. (n) Temporal load of SO_4 in the snowpack.

Figure 29: Temporal load of the analysed chemical compounds. The vertical red line indicates the separation date between the last snowpit before the event and the first one after it.

3.4 Local data

3.4.1 Ny-Ålesund weather station

Here, weather data retrieved by the SEKlima website, collected at the Ny-Ålesund weather station, are presented. In Figure 30 all the data for the days from March 15 to March 19 are shown. On the top plot the temperature is reported with a scale of colors, ranging from blue for below zero temperatures to red for above zero temperatures. The total cumulated liquid precipitation over the last 10 minutes is represented with black bars in the same plot of the temperature, to ease visual correlation between the two variables. In fact, it's evident how a drastic change in air temperature, just before midday of March 15, is associated with the arrival of a light rain, as the first precipitation corresponds to a maximum rain rate of 2.4 mm/h. Then, during the afternoon of March 15, and during the entire morning of the day afterwards, the precipitation is constant and the rate can be classified as moderate rain as it exceeds 2.5 mm/h [89]. In the following days the rain decreases with occasional light showers, especially around midnight of March 18. On the plot below, wind intensity and direction are reported on the same dates as the top plot. Both variables are measured at 10 m above the ground and reported in the dataset as average of the 10 minutes before. The intensity is illustrated with a blue line and is reported every 10 minutes. It reaches a maximum value of about 15 m/s, that corresponds to a Force 7 on the Beaufort Wind Scale, usually associated with 4 to 6 meters ocean waves and some resistance when walking against wind [90]. The wind direction of provenance is represented with arrows that follow the wind direction. Each arrow corresponds to the mode of three hours before and after the time where the arrow is drawn, in order to avoid considering quick changes in wind direction.

In the same section, wind roses are presented both for the days of the event (from March 15 to March 18) and for the climatology of the same days for the years from 1995 to 2007, the years available from the website. Wind roses show the distribution of wind provenance, represented through a pie chart with a defined slice angle width. Each slice represents a wind provenance direction, and its length characterizes the percentage of data coming from that direction interval. The more one slice is long, the more is the percentage of data where wind comes from that direction. Each slice is additionally portioned with different colors, that indicate the fraction of winds within a certain interval of speed in that slice, with the color legend reported on the bottom left section of the picture.

Figure 31 considers the wind data for the days from March 15 to March 18 only for year 2022, so that this wind rose only examines the event. As also visible in Figure 30, the main wind provenance directions during the event are S and SW, while the most intense winds arrive mainly from SE.

Figure 32 considers instead the same days range but for years spanning from 1995

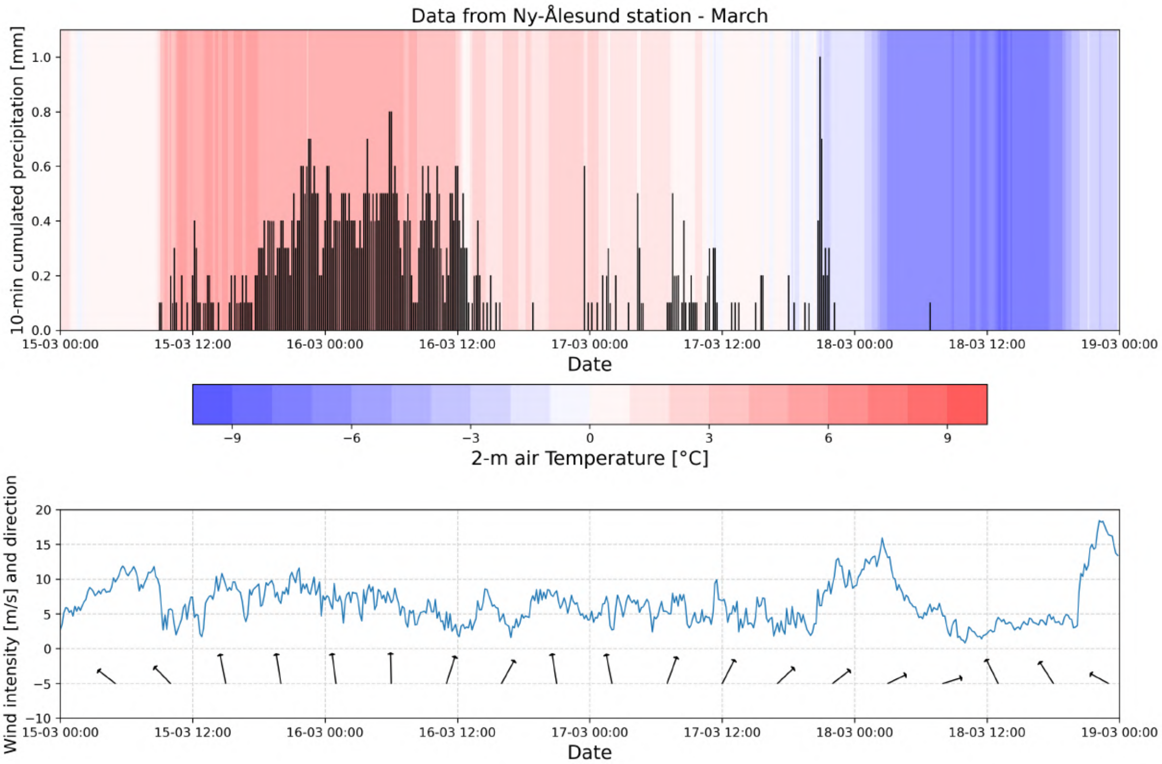

Figure 30: **Weather data from the Ny-Ålesund station as retrieved from SEKlima.** On the top plot the air temperature and the 10-min cumulated precipitation, while on the bottom one the wind intensity and direction. The plot focuses on the dates from March 15 to March 19, the days around the event.

to 2007 (the years that had available data on the SEKlima website), to have a control climatology for the previous picture. Here, three main directions are identifiable, NW, SW, and SE, that may be linked to three major winds that blow in the area, mainly due to topography. These different wind patterns will be more carefully analysed in Section 4.

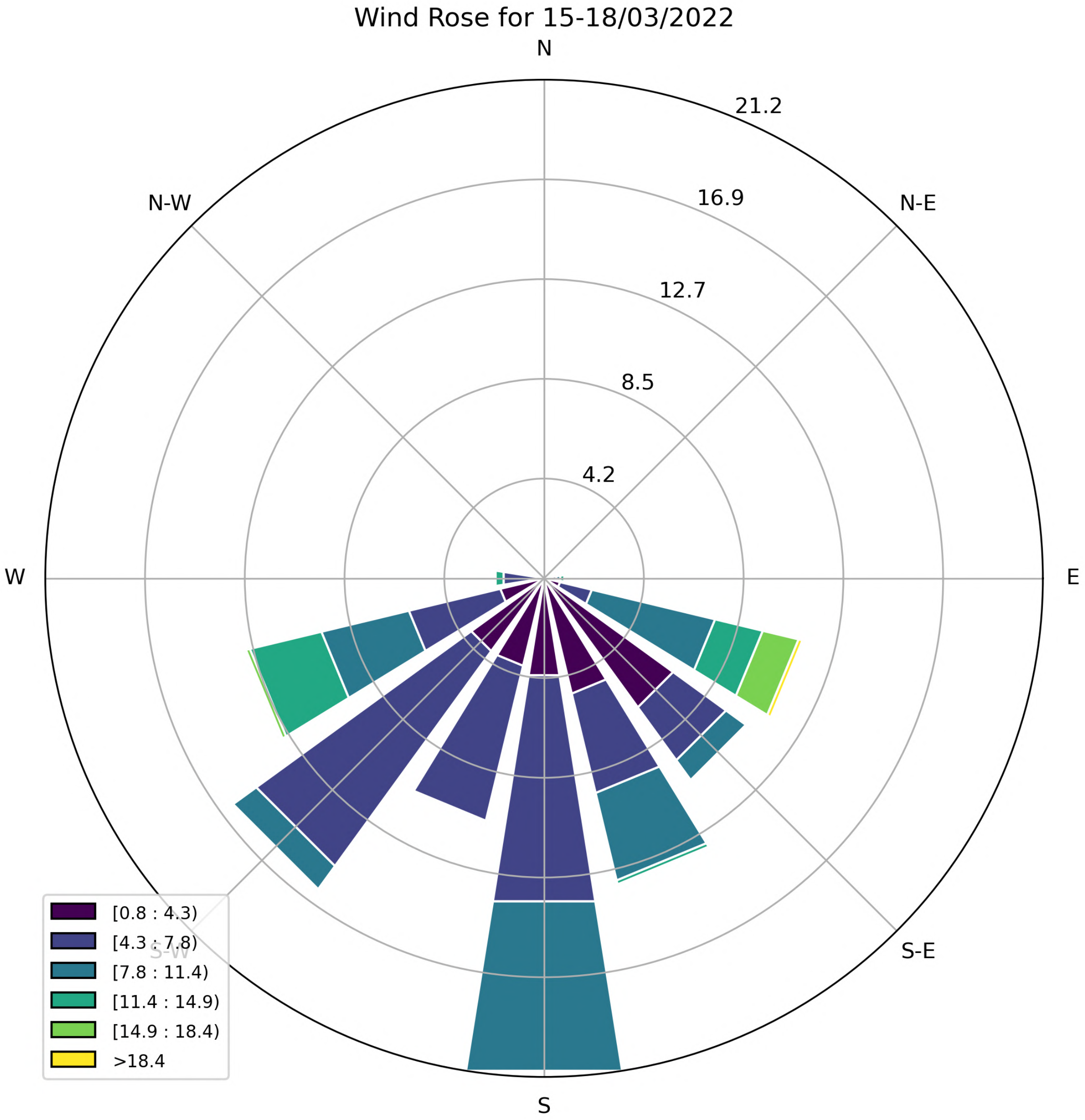

Figure 31: **Wind rose for the event days**. The data are for the days from March 15 to March 18, 2022. South-West and South result as the main directions of wind provenance.

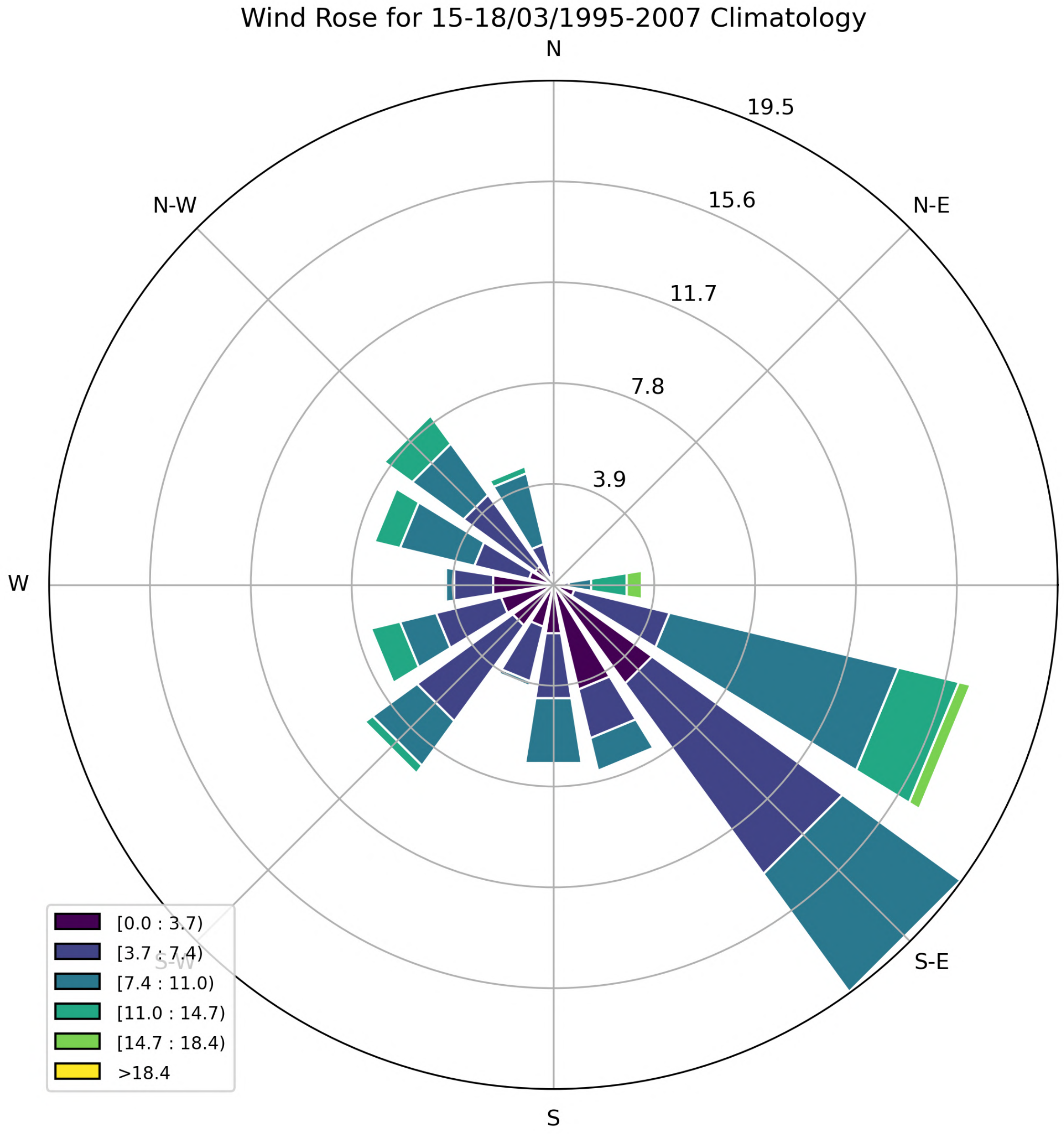

Figure 32: **Climatologic wind rose**. The considered days are the same as Figure 31, considering the years from 1995 to 2007. South-East results as the main directions of wind provenance.

3.4.2 Zeppelin observatory

Atmospheric chemistry data were retrieved from the Zeppelin observatory over Ny-Ålesund, and they are used as they can give hints about the air mass properties that passed over the region during the event. In Figure 33 time series for different chemical compunds are represented, considering seven days before and after March 16, from March 9 to March 23.

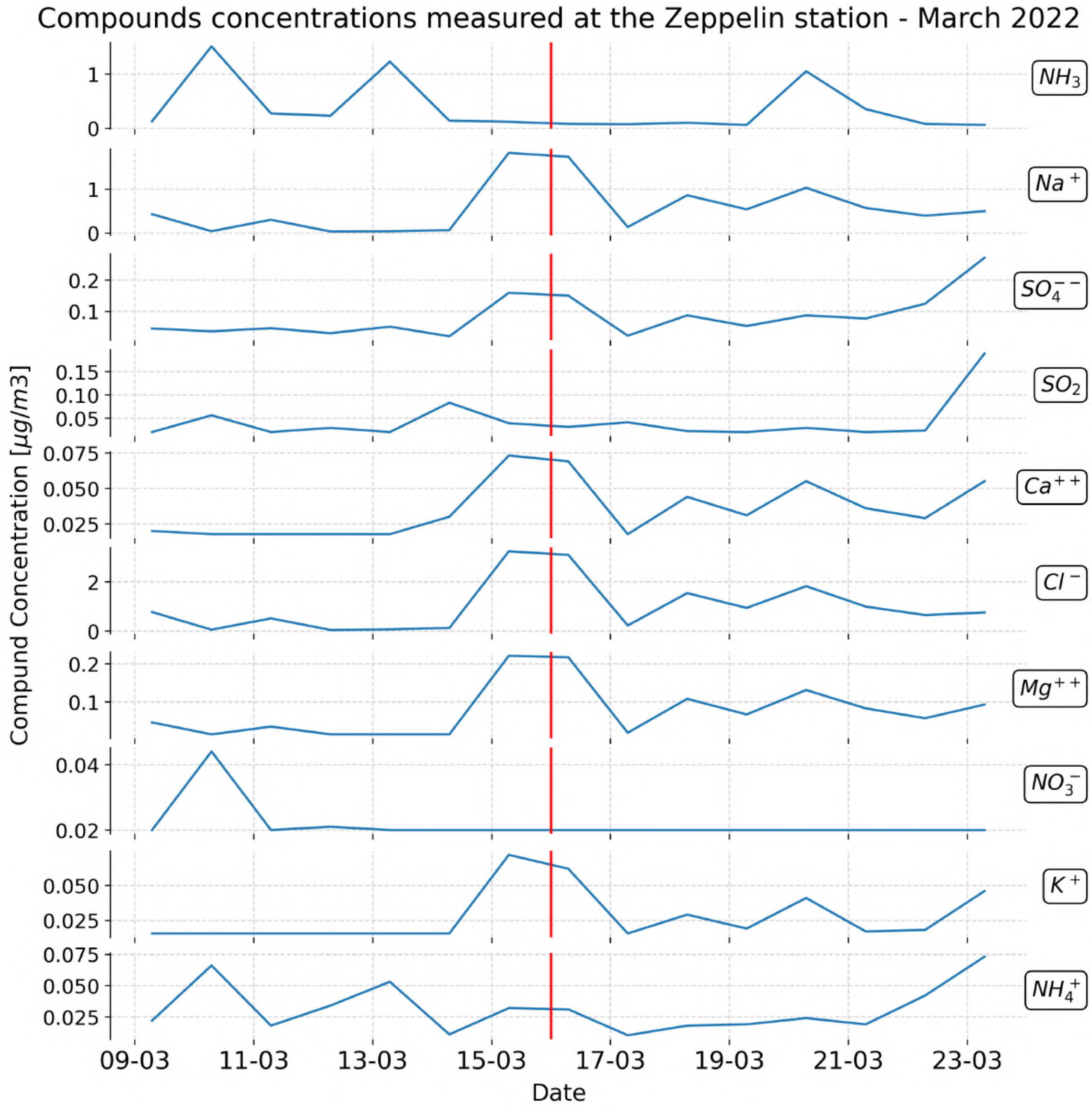

Figure 33: **Concentration of the main compounds as measured by the Zeppelin observatory**. The days considered went from March 9 to March 23, 2022. The event day, March 16 - 00:00, is marked with a red vertical line.

Midnight of March 16 is identified with a vertical line, to ease the event identification. Different compounds are found to have increased in correspondence of the air mass passage between March 15 and March 17, such as Na^+, Cl^-, or K^+. Others, such as NO_3^- or SO_2, don't seem to be influenced at all by the event. These different behaviours can give indications about the air mass provenance, where it passed from, and what it collected on its way, and will be further discussed. The comparison between these results and the chemical data from the snowpits presents challenges due to some problems. In fact, they have their different time resolutions, there could be lack of knowledge of certain aerosol-to-snow processes, and the removal of compounds by percolation modifies the real concentrations of the snow surface.

3.5 Radiation data

In Figure 34 radiation data from CCT are shown, with midnight of March 16 marked with a vertical red line. On the top plot downward SW and downward LW radiation intensities are reported as measured from the sensors positioned at 25 m, considering the same date interval as in Figure 33, seven days before and after the event.

In correspondence of the event, a high and stable downward LW radiation is present, while the daily cycle of solar light, already present in March at these latitudes, looks to be attenuated with respect to the days around. In the bottom plot of Figure 34 the SW albedo as measured from the SW sensors is presented. An abrupt decrease in albedo is visible during the event, and will be further discussed.

3.6 MODIS

Here, data obtained from the MODIS satellite are presented. Two clear-sky days close to the event, one before and one after it, have been selected using `https://worldview.earthdata.nasa.gov/`. A 3 km x 3 km area on the Holtedahlfonna glacier, close to Ny-Ålesund (Figure 35), has been chosen to average the radiation data on, so that eventual errors could be reduced. The distant and wider area has been chosen so that the topography or the presence of the sea could not influence the results. In fact, choosing a pixel over the city would almost surely have brought contributions from the sea or the buildings.

Data from all the MODIS channels have been retrieved, and the results are shown in Figures 36a and 36b, respectively for SW and LW channels. The green line refers to March 11, the closest clear-sky day over the region before the event, while the black line refers to March 18, two days after the event. It can be seen that while the longwave emission doesn't seem to change a lot, the SW reflectivity, measured as a fraction from 0 to 1, did change, and in general it results lower after the event, in the majority of the channels.

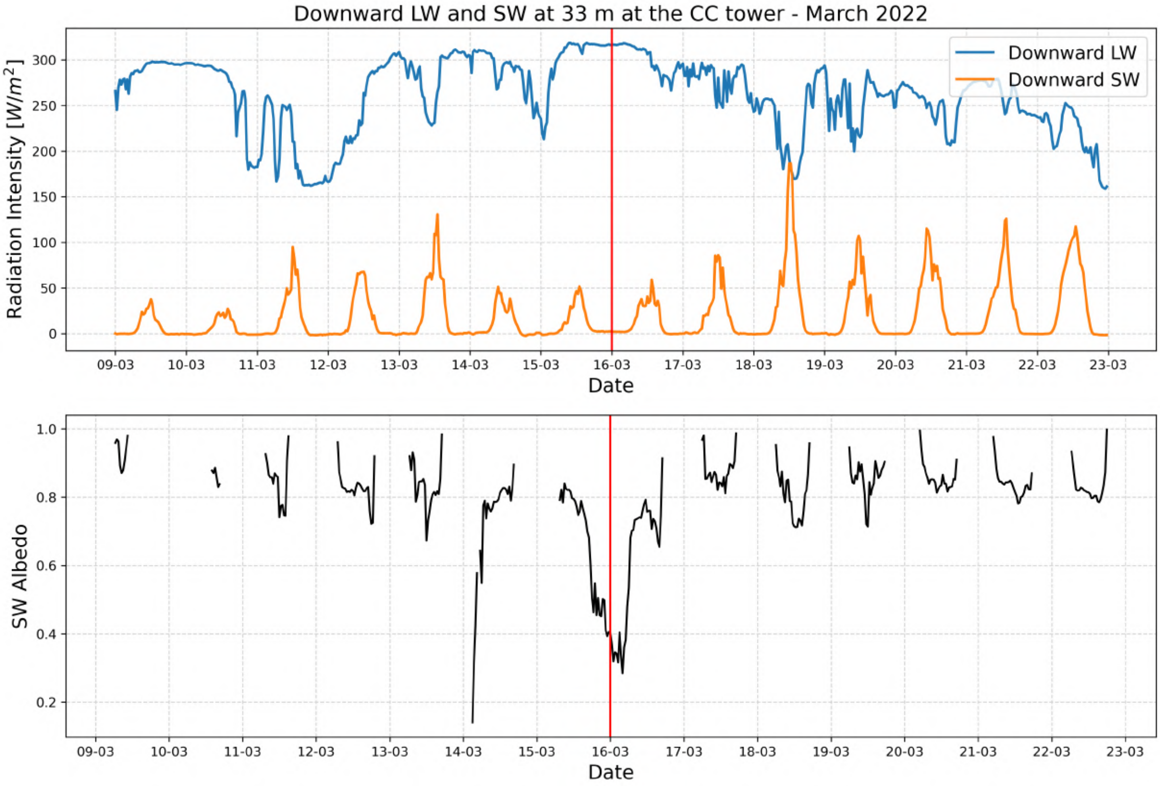

Figure 34: **Radiation Data from the CC tower**: the days considered were from March 9 to March 23, 2022. In the plot above downward LW and SW are represented, while on one below the albedo is plotted.

Figure 35: **Holtedahlfonna glacier location.** The red square approximately indicates the 3 km x 3 km area used to retrieve radiation data.

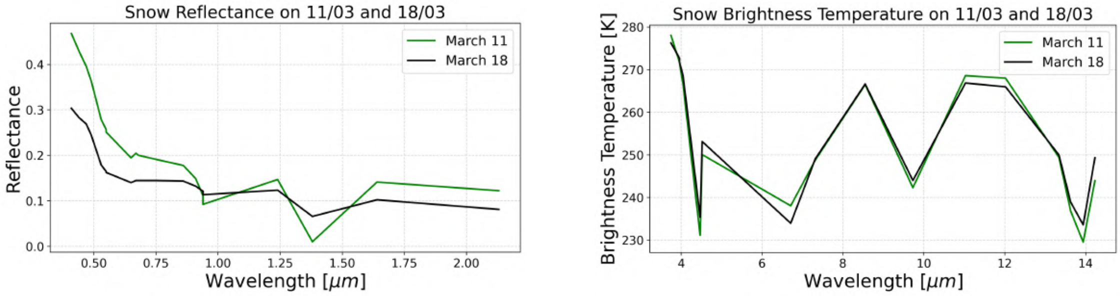

(a) **Reflectance (SW) Comparison** for March 11 (green) and March 18 (black), retrieved from the Holtedahlfonna glacier area. Reflectance is reported as a number between 0 and 1.

(b) **Brightness temperatures (LW) comparison** for March 11 (green) and March 18 (black), retrieved from the Holtedahlfonna glacier area. The computed brightness temperature is reported.

Figure 36: Comparison between MODIS channel between March 11 and March 18.

MODIS imagery has also been used to retrieve RGB images of the whole archipelago, in order to check impacts of the event on the sea ice that lies around the islands, especially on the north-eastern coastlines. The RGB images are composite of three different MODIS channels as explained in Section 2.3.6. Considering only weather conditions when the sea ice was visible, four days have been chosen before and after March 16, so that the evolution of the sea ice could be visible. The 8th, 11th, 18th, and 25th of March have been selected and are presented in Figures 37a, 37b, 37c, and 37d.

On March 8 (Figure 37a) the sea ice completely covers the Storfjorden, that is the big fjord on the south that separates the biggest island Spitsbergen from the two island on the East.Also on the East side of the picture, the sea ice entirely covers the ocean, reaching Kong Karls land, that are the two small islands on the right, and Kvitøya, the slightly bigger island at the top right corner. On March 11 (Figure 37b) the situation looks unchanged, except for the detachment of the sea ice from the coastlines in Storfjorden. A general disgregation in the southern region is also visible. After the event, on March 18 (Figure 37c), most of the sea ice has disappeared from Storfjorden, leaving none on the southern region of the picture. Moreover, the eastern coasts of the islands are now ice free, just as Kvitøya at North-East. Even if cloudy, it is visible how on March 25 (Figure 37d) more and more sea ice is being fragmented and transported away. Now, also the western coast of the southern part of Spitsbergen looks ice free, as most of it is drifting into the sea.

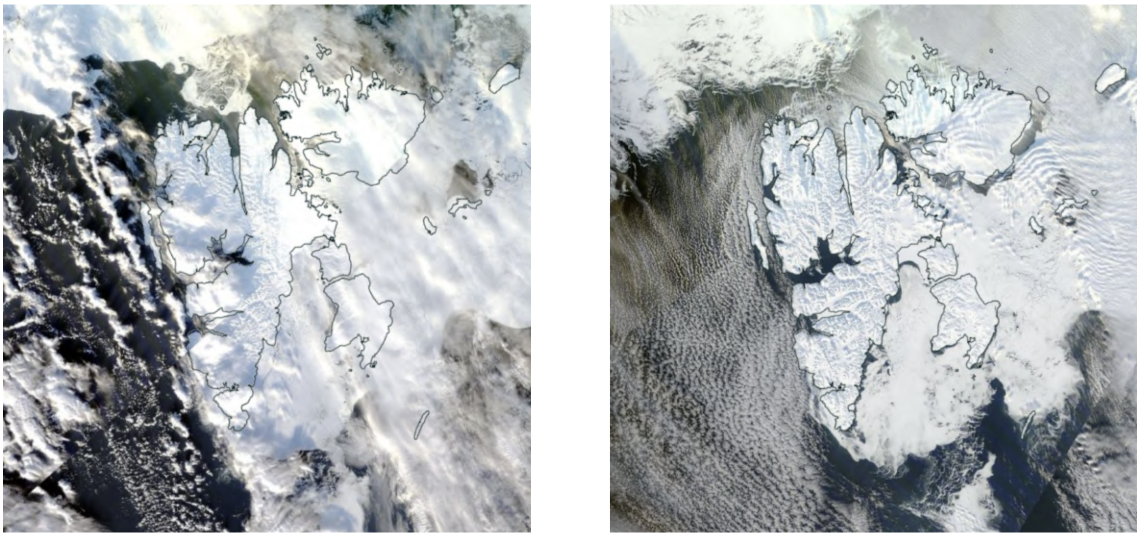

(a) **MODIS picture of Svalbard on the 8th March 2022.** The sea ice completely covers the Storfjorden, that is the fjord that separates Spitsbergen from the two island on the East, Barentsøya and Edgeøya.

(b) **MODIS picture of Svalbard on the 11th March 2022.** The sea ice is still visible below the clouds, completely covering the Storfjorden, but detached at the northern border.

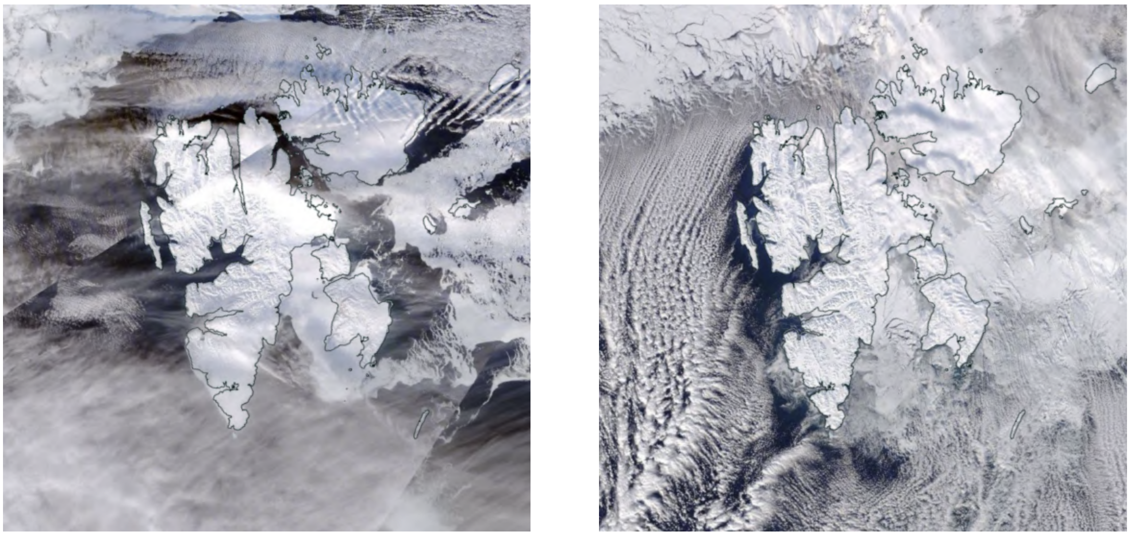

(c) **MODIS picture of Svalbard on the 18th March 2022.** The sea ice extention is greatly reduced, as the south-western section does not exist anymore.

(d) **MODIS picture of Svalbard on the 25th March 2022.** The sea ice cover is significanlty decreased and the remaining one results fragmented and almost completely detached from the shoreline.

Figure 37: **MODIS imagery.** These pictures have been taken by NASA Worldview application (`https://worldview.earthdata.nasa.gov/`), part of the NASA Earth Observing System Data and Information System (EOSDIS).

3.7 CARRA reanalysis

3.7.1 Total Precipitation

From the CARRA-East reanalysis, that focuses on the eastern Atlantic Arctic region, both the total precipitation and precipitation type products have been retrieved from March 9 to March 23, where both products refer to the precipitation that reaches the surface. The precipitation type product classifies the precipitation according to eight categories associated to a number: drizzle (1), rain (2), sleet (3), snow (4), freezing drizzle (5), freezing rain (6), graupel (7) and hail (8) [91].

To produce the following figures, the first two categories have been identified as ”rain” (mostly liquid precipitation) while the others as ”snow” (mostly solid precipitation). The resulting maps of the two categories has been combined with the total precipitation product to obtain an integrated map that comprehends both the amount of precipitation and the precipitation type, as shown in Figure 38a. The 3h cumulated snow precipitation is shown in red shades while the 3h cumulated rain is shown in blue. In Figure 38b a zoom has been made to show the region around Ny-Ålesund, that is marked in both figures with a black dot. Both the plots represent the midnight of March 16.

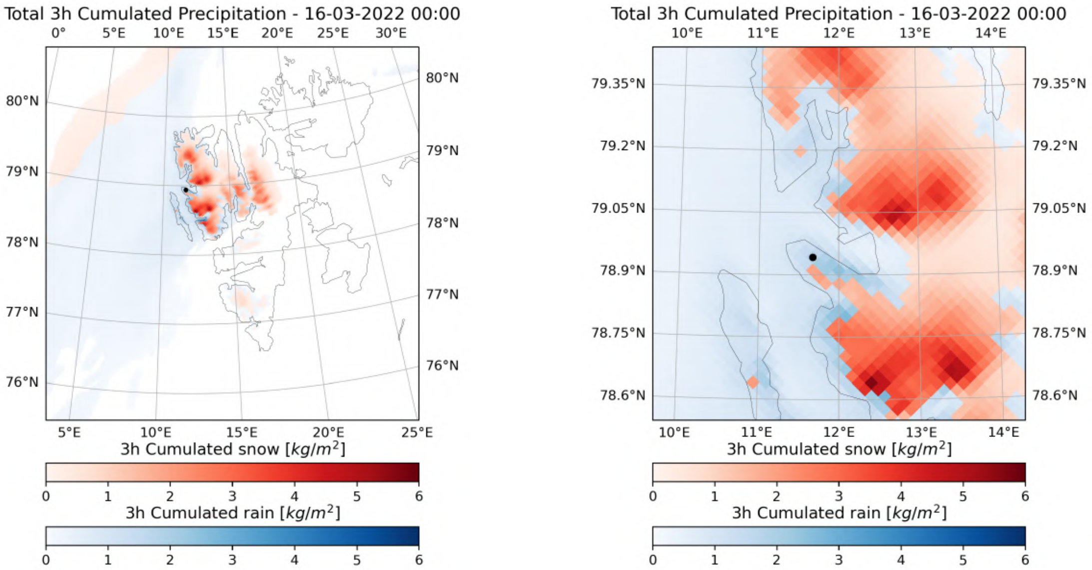

(a) **Precipitation at the surface on Svalbard at midnight of March 16.** Ny-Ålesund is marked with a black dot. Rain is represented in blue while snow in red. The atmospheric river coming from south-west is visible.

(b) **Precipitation at the surface on Svalbard at midnight of March 16, zoomed.** Ny-Ålesund is marked with a black dot. Rain is represented in blue while snow in red. It is visible how at higher altitudes snow arrived to the ground, while at low altitudes rain arrived.

Figure 38: Precipitation at the surface on Svalbard at midnight of March 16 from the CARRA reanalysis.

In Figure 38a the arrival of the AR from south-west is visible, with precipitation happening in a wide area at north-east of the archipelago, including Ny-Ålesund. On the zoomed plot, in Figure 38b, it is visible how the snow reached the ground only in the mountainous areas, while in others only rain arrived to the surface.

3.7.2 Sea Surface Temperature

Then, sea surface temperatures were retrieved for the whole month of March 2022, to analyse eventual effects the event could have had in Kongsfjorden. In Figures 39a (March 15) and 39b (March 17) the retrieved SST is represented for the western coast of Svalbard. Before the event, a steep gradient of temperature is visible just outside Prins Karls Forland, the narrow and long island at the center of the plot. Right after the event, on March 17, a warmer water tongue stretches from the open sea to the fjord, meaning that the SST raised in that area, probably due to the event. This will be further discussed.

Considering Kongsfjorden as the area delimited by the red rectangle in Figures 39a and 39b, a mean SST for that area has been computed for each day of March 2022 and reported as a time series in Figure 40. It is visible how the month of March carries a general increase of temperature, with almost 1 K of increase with the event, identified by a vertical red line.

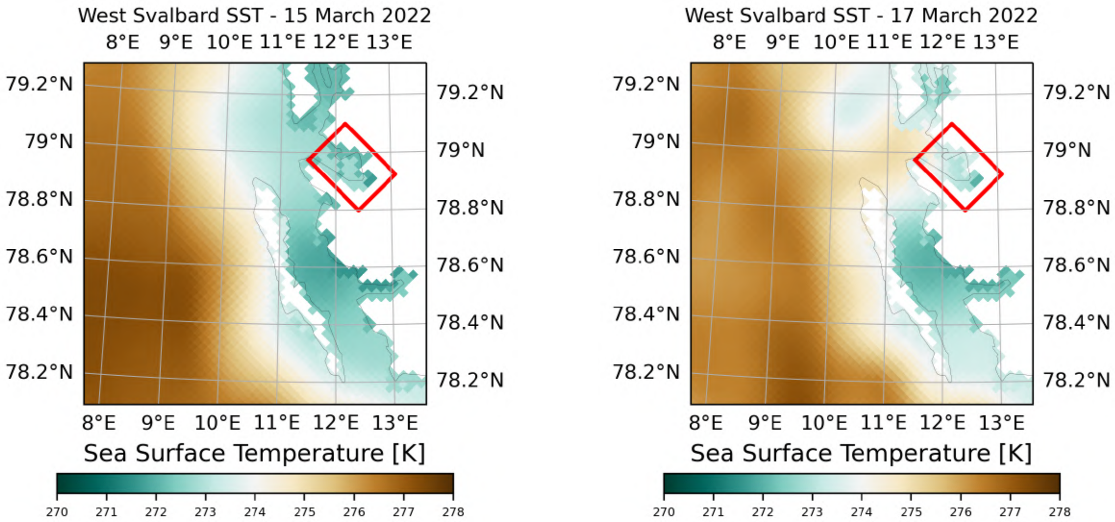

(a) **SST on West Svalbard on March 15.** A gradient of temperature is present just offshore of Prins Karls Forland, the narrow and long island at 11°E.

(b) **SST on West Svalbard on March 17.** It is visible how a tongue of warmer water stretches from the open sea to Kongsfjorden.

Figure 39: Comparison between SSTs on West Svalbard for March 15 and 17.

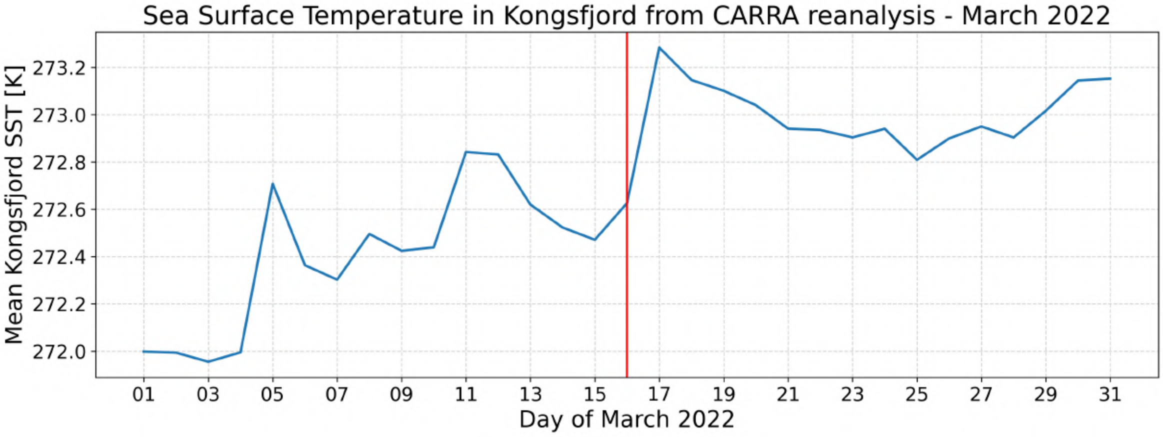

Figure 40: **SST series for Kongsfjorden.** The fjord is identified with the red-bordered area in Figures 39a and 39b. The vertical red line identifies March 16 - 00:00.

3.8 Zeppelin Webcam

To better understand the local weather conditions in Ny-Ålesund, webcam pictures have been retrieved from the Norsk Polarinstitutt website [83]. Four of the analysed pictures are reported here, for midday of March 13, March 15, and March 18 (respectively Figures 41a, 41b, and 41d). Since the picture taken at midday on March 16 was completely white due to weather conditions, the one taken at 10:00 is shown here (Figure 41c). The pictures cover the entire event from two days before to two days after if, when the sky cleared again from clouds. The camera is pointed toward Ny-Ålesund and reaches the fjord behind, Kongsfjorden, with the mountains beyond. On the left a section of the airport runway is visible, while at the center the different buildings are recognizable.

From Figure 41a the snow conditions before the event are visible, as all land surfaces are covered in bright snow. Two days after, in Figure 41b the sky is covered with low level clouds and a snowfall is present, since white flakes are visible all over the picture. On the day of the event, in Figure 41c, the weather conditions completely mask the surface, even if something can still be distinguished. On March 18, Figure 41d, the sky results clear again but the snow condition changed dramatically. The snow doesn't look as bright as before and darker patches are visible in many points around the city.

(a) **Webcam image from the Zeppelin observatory.** Picture taken on March 13, at 12:00.

(b) **Webcam image from the Zeppelin observatory.** Picture taken on March 15, at 12:00.

(c) **Webcam image from the Zeppelin observatory.** Picture taken on March 16, at 10:00.

(d) **Webcam image from the Zeppelin observatory.** Picture taken on March 18, at 12:00.

Figure 41: Webcam images taken from the Zeppelin observatory in different days around the event.

3.9 Snowpack Model

In this section results from the EBSM model run by Prof. Ward van Pelt are presented. In Figure 42 three variables are visualized inside the snowpack. A light black line determines the snow height, and therefore the maximum height on which the variables are visualised.

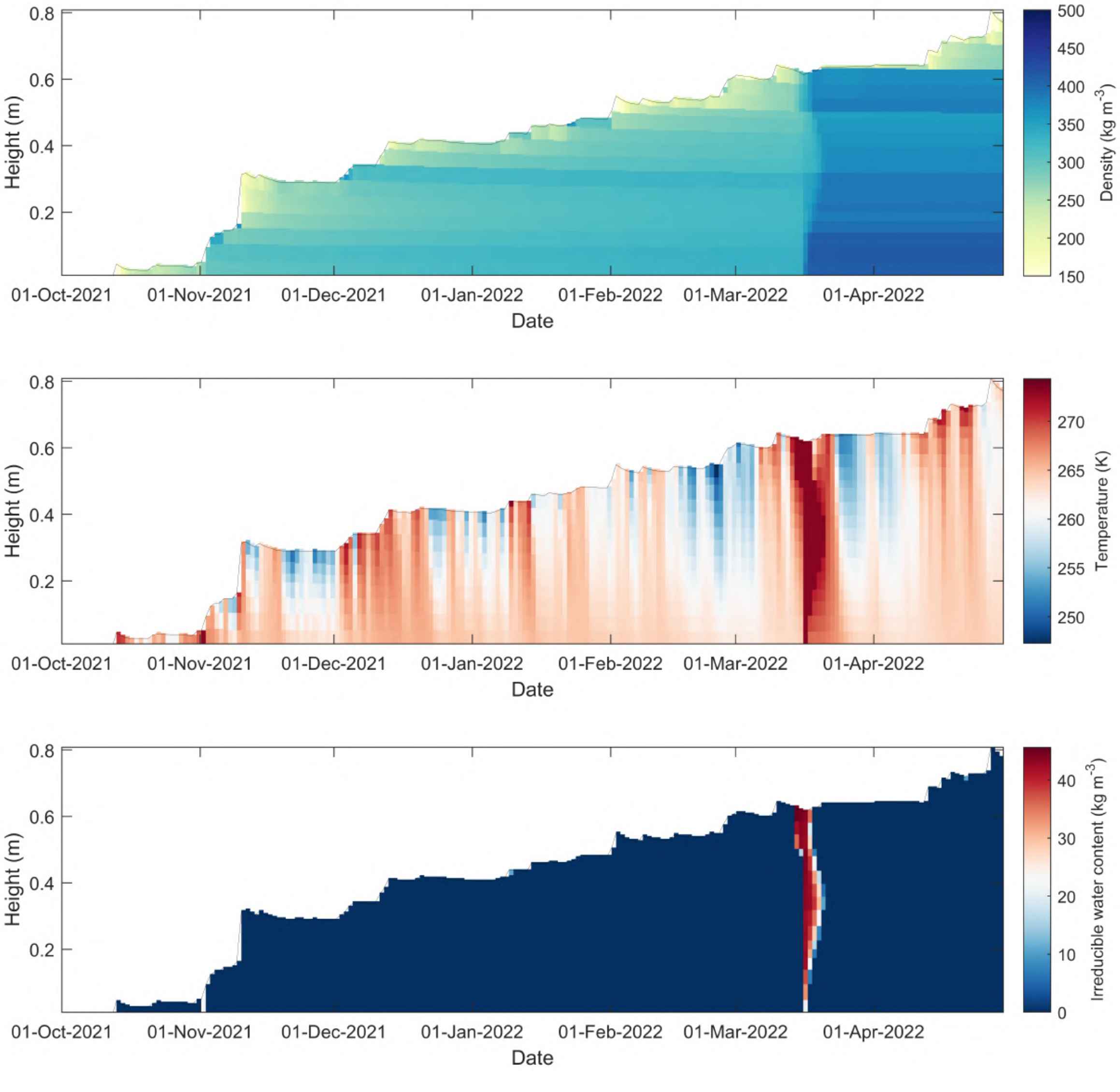

Figure 42: **Energy Balance Snow Model results.** From top to bottom different variables are represented inside the snowpack, snow density, snow temperature, and irreducible water content. Personal communication by Ward van Pelt.

The snow density is represented on the top plot, where the event is clearly visible in the middle of March, with a density increase all over the snowpack depth. Some more features are visible, such as a denser layer around 30 cm created around the beginning of December, probably created by a particular snowfall, that could correspond to a denser layer found in the snowpits. The snow temperature is instead represented on the middle plot, where the event stands out as the whole snowpack quickly reaches a temperature of 273 K, that seems to be kept for some days in the central layers. In the bottom plot the irreducible water content is shown, that is the amount of water contained between the snow grains. As expected, it is not zero only when the rain percolates inside the snowpack, starting from March 16 and reaching the bottom in a couple of days. These results will be afterwards compared to the observation available for the snowpack.

Chapter 4

Discussion

While some of the presented results don't need an extensive analysis other than the alrealy done comments, as they have very clear and direct implications, some others need a deeper examination. In this chapter, further analyses are carried out on the previous results and some discussion on them is presented. Surely, due to the large amount of data, the presented analyses do not compose the entire sprectrum of studies that could be accomplished, but at least they present the major characteristics end effects of the ROS event.

4.1 Large scale effects

In Section 3 the geopotential configuration in the days around the event has been reported. As presented, a weak configuration of the polar vortex seems to have led to the creation of a corridor between the colder polar air and the warmer air at mid-latidudes. This caused the intrusion of warm and moist air from mid-latitudes, passing from the North Atlantic Ocean. At the same time, an AR generated around the Gulf of Mexico, about 8000 km away, was helped by the previously mentioned corridor to stretch all over the North Atlantic Ocean and reach Svalbard around midnight of March 16.

This hypothesis can be corroborated by the combined plot in Figure 43, where both the geopotential at 500 mbar and the AR are plotted together. Both are shown for midday of March 15, the geopotential height with colors while the AR with dotted lines.

The results from the HYSPLIT model suggest that while the AR stretched northward and eastward thanks to winds generated by the two pressure systems, winds acted in its interior moving moist air poleward toward Svalbard. When the AR encountered land, it precipitated producing the ROS event [92].

It appears clear from the HYSPLIT results in Figures 19, 20, and 21, that the airmass that generated the event passed from the Norwegian Sea the previous day, and over Scotland on March 14. Being at low altitude during the previous two days, the air mass might have transported sea spray and likely also some anthropogenic product since it passed over Scotland and Northern Ireland. This will be verified with the chemical analyses.

The passage of the previously mentioned corridor can be seen from 20, where the pink, cyan, and green trajectories correspond to airmasses that generated rain on Ny-Ålesund. The others correspond to trajectories arrived before (yellow) and after (red, blue) the event. While the event-related ones pass from the Norwegian Sea and Scotland, the others have a different provenance, as they mainly come from the Labrador Sea (between Greenland and Canada). So, it is visible how the circulation changed with the passage of the corridor between midday of March 15 and midday of March 16, creating a 24-hour window for the AR to reach the archipelago.

From the CARRA reanalysis, in Figures 38a and 38b, it is visible how on midnight of March 16 a lot of precipitation resulted on north-western Svalbard, around Ny-Ålesund. The distribution of snow and rain, together with an analysis of the topography, suggests that above an altitude threshold variable between 500 m and 1000 m the precipitation was still in solid form, while below those altitude it melted becoming liquid. As it resulted, since Ny-Ålesund is located about at the sea level, it only received liquid precipitation.

The presence of effects of the rain of the SST can be estimated through Figure 44, where in colors the SST difference between March 17 and March 15 is showed. With dashed lines instead, the SST of March 15, the day of reference, is reported. It can be clearly seen that an approximate area of 600 km^2 offshore of the Brøggerhalvøya peninsula (where Ny-Ålesund is located) increased its temperature with a mean of 1.6 K in two days, probably due to the rainfall.

Further from the coast the SST instead seems to have cooled down, up to a decrease of $-1.5\,°\mathrm{C}$. Ascribing the temperature changes only to the precipitation and assuming its temperature spatially constant, the rain temperature at the surface can be estimated observing which areas have warmed up and which ones have cooled down. The dashed line at 275 K seems the one best dividing the warming and cooling regions, giving an estimate of about 2 °C for the rain temperature. The value seems to be acceptable for rain generated by melted snow falling with a over-zero air temperature. Anyway, no specific literature has been found on rain temperature, so that the value cannot further discussed.

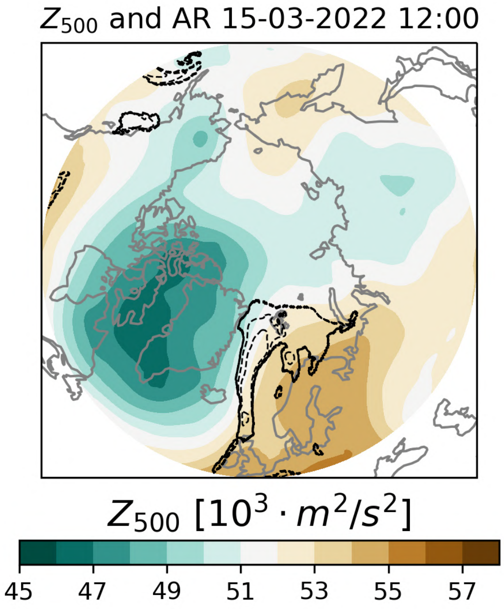

Figure 43: **Combined plot for the geopotential and AR map.** The geopotential at 500 mbar, in colors, shows how the AR responsible for the event, shown in dashed lines, was helped by the synoptical configuration to reach Svalbard.

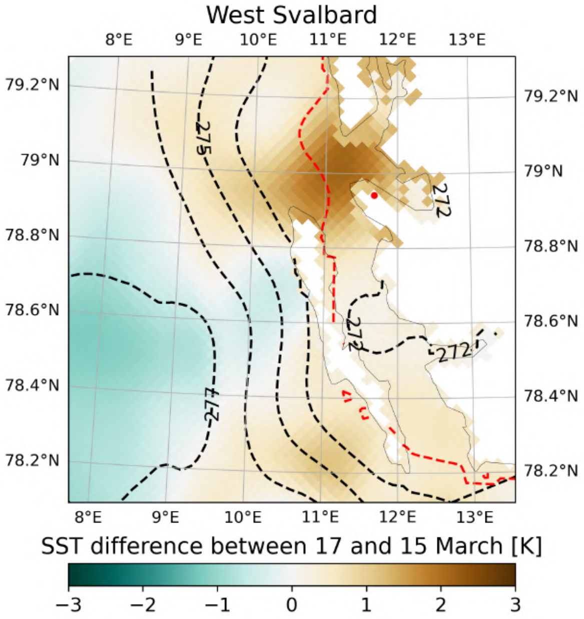

Figure 44: **Analysis of SST changes.** In colors, the SST difference between March 17 and March 15, while the dashed lines represent the SST on March 15, that is the reference one. 273 K, that approximately correspod to 0 °C is colored in red. Ny-Ålesund is marked with a red dot.

4.2 Chemical analyses

Some further chemical analyses can be carried out using the results from the snowpits (Figures from 28e to 28n) and from the Zeppelin observatory (Figure 33). The Zeppelin data have been analysed again and results reported in Figure 45, marking with a black dot the data that exceed the 90th percentile of whole month. In this way, the compound that presented a significant increase during the ROS event can be identified.

Then, the possible sources of the different chemical compounds has to be identified, in order to perform a qualitative source apportionment. It is in fact impossible to do a complete source apportionment due to the limited amount of data. In Table 4, the compounds analysed in this work are reported together with the relative major sources and the principal possible origin is reported (natural and/or anthropogenic), keeping in mind the characteristics of the analysed region.

The last column indicates if the compounds presented a significant increase during the ROS event. For the compounds measured in the Zeppelin observatory the significance of the increase is defined by Figure 45, otherwise the plots in Section 3.3 are used and checked manually, with particular focus on the surface layer, that is the one with the higher correlation with the event.

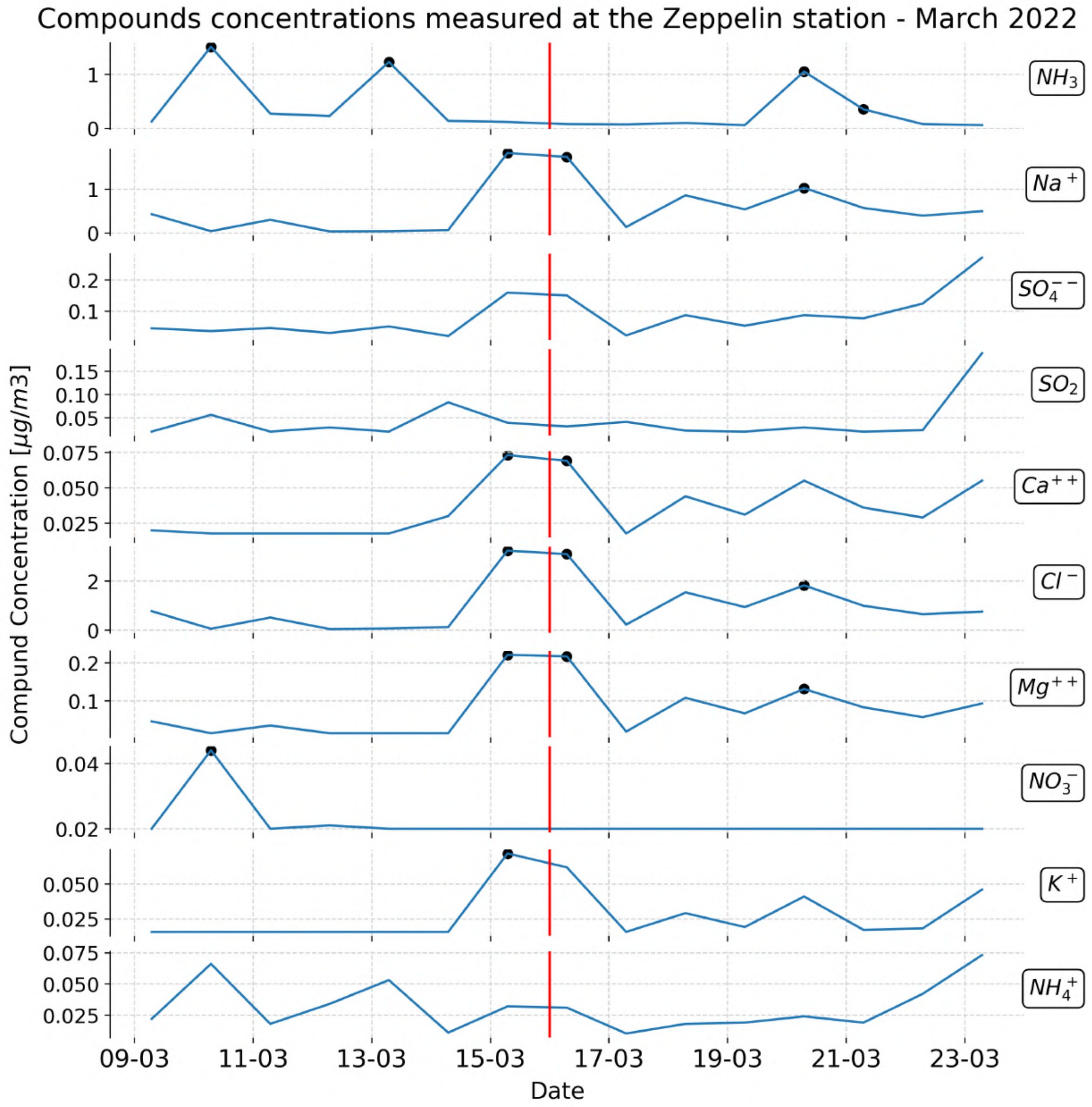

Figure 45: **Concentration of the main compounds as measured by the Zeppelin observatory**. The days considered were from March 9 to March 23, 2022. The event day, March 16 - 00:00, is marked with a red vertical line. The data exceeding the 90th percentile of the the whole March 2022 are marked with a black dot. If a dot is found around the red line, the compound is associated with a significantly increase during the ROS event in Table 4.

It looks clear that all the anthropogenic compounds, with particular attention to the ones of ones of major anthropogenic origin, such as NH_3 or SO_2, didn't have a significant increase during the event. On the other hand, compounds with mainly natural sources, such as Na or Mg did show a significant increase. These results suggest that the air mass responsible for the ROS event didn't collect a significant amount of

Compound	Major Sources	Natural	Anthrop.	Sign. Increase
NH_3	Agricolture, Animal husbandry [93]		●	×
Na^+	Seawater, mineral dust [94]	●		✓
SO_4^{--}	Minerals, Industry [95]	●	●	✓
SO_2	Fossil Fuels Combustion [96]		●	×
Ca^{++}	Mineral Dust, Industry [97]	●	●	✓
Cl^-	Sea Spray [98]	●		✓
Mg^{++}	Mineral Dust [99]	●		✓
NO_3^-	Fossil Fuels Combustion [100]		●	×
K^+	Sea salt, Dust, Biomass Burning [101]	●	●	✓
NH_4^+	Agricolture, Animal husbandry [93]		●	×
Br	Marine Activity [102]	●		✓
C_1−Formic	Organic [103]	●		×
C_2−Acetic	Organic [103]	●		×
C_2−Glycolic	Organic, Biomass Burning [104]	●	●	×
C_2−Oxalic	Organic, Biomass Burning [105]	●	●	×
MSA	Primary Production [106]	●		✓

Table 4: **Major sources of different compounds.** With a × is marked the major origin of the compound, either natural or anthropogenic. It has to be stressed that almost every compound has both a natural and anthropogenic origin, so here the relative major origin is reported, also considering the context of the analysed region and air mass. If the compound had a significant increase with the event, the column contains a ✓, with a × otherwise.

anthropogenic compounds while passing over Ireland and Scotland, while it probably accumulated a significant amount of sea spray aerosols above the Northern Atlantic Ocean. In fact, the compounds that show a significant increase are all attributable to sea provenance, such as ions from salt dissolved in water or primary production, as MSA [107].

From Figures reported in Section 3.3 regarding the distribution of chemicals, the effects of the ROS event on compounds inside the snowpack can be studied. Some compounds, such as Br or Ca, present a superficial layer heavily concentrated right after the event. These compounds are mainly of natural origin and their provenance has just been discussed. Some others, that are the C1 and C2 acids, decrease their total concentration and do not present a new superficial concentrated layer. Anyway, looking at the loads in Figures from 29e to 29n, it is visible how all the compounds analysed do decrease immediately after the ROS event or in the two snowpits afterwards.

This behaviour can be explained through the percolation of water, that likely washed away the compounds from the snowpack. As a rule of thumb, the more soluble compunds decrease more than the others as they were better collected by percolating rain on its way to the ground. Then, since the snow collection site is slightly downhill (Figure 46), the water that gathered on the bottom of the snowpack could slowly have flowed into the Westbyelva riverbed. Probably due to this topography all the loads decreased after the event or some days afterwards, when as seen in 23, the snow temperature was still close to zero.

How the compounds suffered the event as a consequence of different solubilities

Figure 46: **Zoomed map of Gruvebadet**, with contour lines marking 5 meters height differences. The probable path followed by percolated water is highlighted with a light blue arrow.

Compound	Rel. Decrease [%]
Cl	22.6
NO_3	50.2
SO_4	42.3
MSA	48.1
Br	38.3
C_1-formic	46.2
C_2-acetic	72.3
C_2-glycolic	76.2
C_2-oxalic	82.3
Na	19.9
NH_4	28.6
K	18.0
Mg	5.4
Ca	-9.9

Table 5: Relative decrease of the load of each element after the event.

can be studied looking at the relative decreases. Each element load has been examined considering two snowpits before the event (9/3/22 and 15/3/22) and two after it

(22/3/22 and 29/3/22). The mean load for each snowpit couple has been computed to attenuate possible errors caused by contamination, analyses and so on. Then, the relative decrease for each element has been determined, with results reported in Table 5. Referring to other studies, as in [108], a ranking for the most and less influenced compunds can be done. It resulted that the most affected compounds were the organic acids, probably because the event didn't deposited them on the snowpack. Others, like Mg or Ca, resulted the least affected, probably because they are less soluble in water. Anyway, it is hard to decompose the effects that act on the relative decrease, since the compounts were both added from the precipitation and removed through runoff.

Additional clues on the provenance of the air mass can be found considering ratios between different compounds. Knowing the fractional presence of the elements in sea water, the superficial layer can be studied to see if the ratios do correspond. Anyway, this is a semi-quantitative analysis since the concentrations of the superficial layer can include many different errors. The partial sea water composition is reported in Figure 47, obtained from [109].

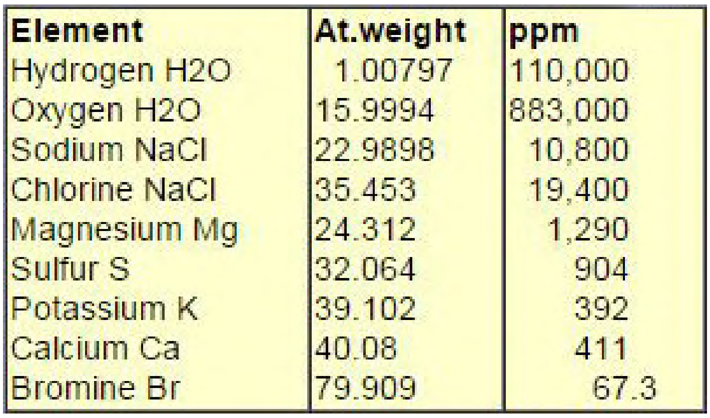

Element	At.weight	ppm
Hydrogen H2O	1.00797	110,000
Oxygen H2O	15.9994	883,000
Sodium NaCl	22.9898	10,800
Chlorine NaCl	35.453	19,400
Magnesium Mg	24.312	1,290
Sulfur S	32.064	904
Potassium K	39.102	392
Calcium Ca	40.08	411
Bromine Br	79.909	67.3

Figure 47: **Sea water composition.** Adapted from [109].

Four compounds, available both in 47 and in the measurements, were analysed, Br, K, Mg, and Ca. Two tests have been made, using Na and Cl as reference elements, as they are the most abundant in seawater. The concentration in ppm has been used as it is the same used for the snowpit analyses (the conversion from ppm to ppb has been made).

Standard element	Br [%]	K [%]	Mg [%]	Ca [%]
Na	58.6	86.8	98.5	191.2
Cl	89.8	133.0	150.9	292.7

Table 6: Percentage of measured concentration of an element with respect to the sea water expected one, using Na and Cl as standards.

From the results in Table 6, it seems that K and Mg completely correspond to sea water. Br presents a slightly lower concentration than the one expected from sea water, while Ca instead presents a higher concentration than the one expected, suggesting that it doesn't completely come from sea sources. This could suggest that, if Br was collected by the air mass, it suffered some chemical reaction that brought it to be removed from the air mass. In fact, once Br is emitted in the atmosphere through aerosol, it passes to the gaseous phase, so that a fraction of it is not deposited with the snowfall [110]. Ca instead, as Mg, could additionaly derive from mineral dust, probaly from the passage over Scotland.

4.3 Wind patterns

Wind patterns are now studied, and differences between climatology (Figure 32) and event (Figure 31) provenance directions are investigated. In Figure 48 the major wind patterns are illustrated, in blue for the climatology and in red for the event.

Figure 48: **Ny-Ålesund map with wind patterns.** In blue the usual (from climatology) wind patterns, while in red the ones during the ROS event.

The wind coming from SE can be explained through local orography, as the fjord mainly stretches in that direction, and through the presence of Kongsvegen glacier at 10 km to South-East (at the start of the blue arrow). Air is cooled down on the top of the glaciers, and when is cold enough, it flows down on the surface of Kongsvegen, a phenomenon called katabatic wind. The channel created by the mountains surrounding the glacier helps in strengthening the wind, that finally results in the strong SE winds measured in Ny-Ålesund [111]. The same explanation can be given for SW winds, that originate in katabatic flow from Brøggerbreen glaciers (Vestre Brøggerbreen and Austre Brøggerbreen, under the red and blue arrows). The last predominant wind direction, the one coming from NW, is probably created by W winds from the ocean that enter the fjord and reach Ny-Ålesund from NW passing the mountains.

During the event, only winds from SW, S, and SE have been recorded. This is probably due to the major synoptic wind conditions, that created a major wind flux from that direction. In fact, a new major wind provenance from South, not seen in climatology, is present. The other two southern directions seem to be associated to the climatologic ones but enhanced by the synoptic conditions, as the wind speeds from SW and SE result higher than the maximum speeds in climatology. This is probably a result of the combination between the already present katabatic winds and the added southern wind due to synoptic conditions.

4.4 Impact on snow physics

4.4.1 Snowpack interior

The snowpack interior is the region of the snowpack underneath the surface. The scale of thickness of the surface layer usually depends on the considered process. For example, the penetration depth of light in snow depends on the wavelength, and can vary from a few millimiters to tens of centimeter [112]. Other processes, such transfer of heat or chemical transport can have other different scales.

For example Figure 23 shows some very cold surface temperatures at the beggining of March, that penetrate in depth only for about 10 to 20 cm, where the snow temperature results less influenced by atmosphere changes. These peculiar radiative coolings tipically occur in calm and clear nights, but also during the day, when they are responsible for forming suncrusts, that are formations created by melting and refreezing of a thin layer on the snowpack surface [113].

The heat transfer process can be better visualized through Figure 49, where the temperature vertical profile is shown for the midnight of different days around the event, from March 12 to March 22. The color gradient shows different days and goes from darker colors for March 12 to light green for March 19, so that a temporal evolution can be followed in the plot. The surface height and temperature is marked each day with a black dot. On the right of the dot there is the air temperature while on the left the snowpack interior.

It can be seen that on March 12, the air temperature is still low (about −15 °C), and the snow surface is even colder probably due to radiative cooling. From the day afterwards the air temperature raises above 0 °C, followed by the snow surface temperature, that quickly responds to the change. The interior instead stays at temperatures around −5 °C.

The interior temperature starts to increase only from March 14, and reaches 0 °C on March 17, after five days the air temperature started to raise. Now, the melting of the snowpack interior probably starts, due to high temperature. After reaching 0 °C, it takes until March 22 (five days) for the bottom layer to cool again and reach sub-zero temperatures, while after March 25 it finally reaches about −5 °C.

It resulted that it is a quite fast process for the snowpack interior to reach the melting temperature, while it may takes many days for it to return at the previous temperatures.

The same seems to hold for the percolation and accumulation of water in the snowpack. Even if the site is slightly downhill (Figure 46), from relativity humidity results in Figure 25, it is evident that the time to accumulate water in the snowpack is shorter than the one needed to the complete runoff.

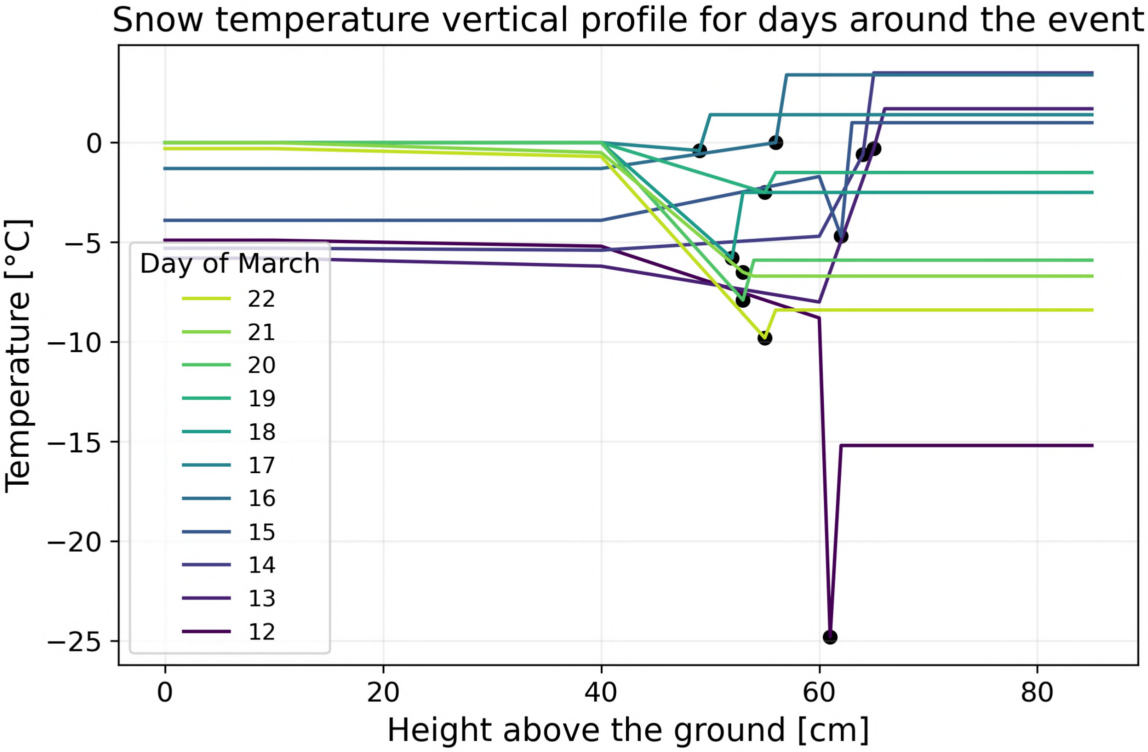

Figure 49: **Temperature vertical profile for days around the event.** The colors have been chosen to follow a gradient, to ease visualization. A black dot indicates the surface height on the relative day. The temperatures are referred to the midnight of each day.

The results from the EBSM model can be now qualitatively compared to the observations. The model results in Figure 42 can be compared to density (26), temperature (22 and 23), and LWC (25) plots to assess similarities and eventual discrepancies. The model results end on the 1st of May, not allowing a comparison for the late spring and melting periods.

Since the model has a way higher resolution than the density measured from the snowpit, it is hard to make a good comparison, but the main structures can be investigated. The low density of snowfall is a characteristic present in both the plots, and also the superficial and bottom dense layers of the two snowpits after the event is well represented. Anyway, the values do not seem to completely correspond, as from the snowpits the denser layers right after the event seem to reach values around 850 kg/m^3 and 750 kg/m^3 respectively for the deep layer and the superficial one. On the model, these layers don't ever exceed 500 kg/m^3. While in the first case the high value is probably given by a high abundance of ice, the model doesn't seem to correctly identify the change of phase, or at least the concentration of ice. Moreover, the model seems to mantain high densities continuously from the event, while from observations the density lowers again after some weeks. This seems to suggest that some snow metamorphism process is not included in the model.

For the temperature all over the year, the cold waves that appear approximately around the start of each month are well represented by the model, probably because they only need the air temperature and a heat transfer equation to be well represented. In fact, if the melting temperature is not reached, phase changes do not enter in the modelization. Focusing on the event, it can be seen that only the first 10 cm layer on the surface reaches 0 °C on March 14, just as the observation. On March 16 all the snowpack results isothermal from the model, as in the observations. The major differences are visible after the event, as in the model the last snowpack region to cool down is the central one, while from the station data it seems the one on the bottom layer. This could be caused by a not perfect soil-snow heat exchange modelling, as probably in the model the soil was considered warmer than it really was.

Since the irriducible content of water defines the quantity of water between the snow grains, it can be compared to the measured LWC, that measures approximately the same thing, with another method. The two result null all over the year, with only non-zero values during the event (and the melting season for the observations). As for the temperature, the shape looks very different, as in the model it seems that the water stays longer in the central layers, while it disappears from the bottom ones. From the observation indeed it results that the bottom layers are the ones to maintain the water for a more prolonged period of time. As before, this could be given by a wrong soil-snow fluxes modellization. Anyway, it has to be said that the presence of ice could also disturb the LWC measurements, but further analyses should be made in this sense.

4.4.2 Albedo and radiative properties

The effect of the event on the radiative properties of the snow can be studied through the albedo, as it has been retrieved for two locations, the CCT and the Holtedahlfonna glacier through MODIS. As previously mentioned, the downward SW radiation seems to be highly attenuated, probably due to the presence of thick low clouds. This can be also seen in the downward LW, that results very high, exceeding 300 W/m^2 on the event day, suggesting again the presence of thick low clouds. These kind of clouds and LW intensities have been found to be correlated with arctic warming and moisture intrusions from mid-latitudes from analysis of the 2015-16 winter, [114], so it is important to consider these events as drivers of snow melting and polar warming in general. The presence of low level clouds is confirmed by the webcam image in Figure 41c, considering that the Zeppelin observatory is located at about 500 m asl.

While the albedo measurements usually don't work during the night due to absence of solar radiation, during the night between March 15 and March 16, it seems that measurements were possible, probably due to diffused light by clouds. These measurements suggest that the SW snow albedo significantly decreased down to 30% during the night period, when most of the rain has fallen. Anyway, it is uncertain if these values can be considered correct since they were made without direct solar radiation. Anyway, the albedo seems to goes back to values around 80% from March 17, just one day after the event. This behaviour can be compared to the MODIS data retrieved over the Holtedahlfonna glacier in Figures 36a and 36b.

From Figure 36b, that reports the brightness temperature of the snow surface, hence its emission, it seems that no big differences are present between the two days, March 11 and March 18. This is probably due to the fact that this variable mainly depends on the superficial snow layers, that according to the nivometric station data in Figure 23 already returned to below zero temperatures on March 18, so that the brightness temperatures result similar. The small differences visible don't have immediate explainings, also due to the punctuality of the measure, but could be caused by presence of water on the snowpack that influences the snow emission.

On the other hand, regarding the snow surface reflectivity shown in Figure 36a, it is visible how the reflectivity in 17 out of 20 channels decreased between March 11 and March 18. This is what one would expect, as the major effect of liquid water in snow is to make the snow grains form bigger clusters [115]. Snow reflectance is sensitive, mainly in the near-infrared and shortwave-infrared intervals, to the grain size [116]. Since these bigger clusters are optically equivalent to larger grains, it results that the albedo of wet snow decreases in comparison to dry snow.

This seems be in contrast with the measurements made with the CCT, but it could have different explanations. The CCT is located over a small hill that suffers snow drift, since it is directly hit by the katabatic wind coming from the Brøggerbreen glaciers. Adding the fact that the CCT measures only considers a small area close to the tower, the quick return to normality could be caused by snow blown over the area. On MODIS data this effect may be removed.Due to this facts, the MODIS data looks more truthful about the snow albedo. Relying on these it is visible how the rain event modified the snow reflectivity, through a process called *snow aging*. As said, the rain modified the snow grains dimension and therefore changed their reflectivity.

Anyway, it has to be considered that the useful cloud-free days were one week apart, and other processes outside the ROS event could have played a crucial role in modifying the snow albedo.

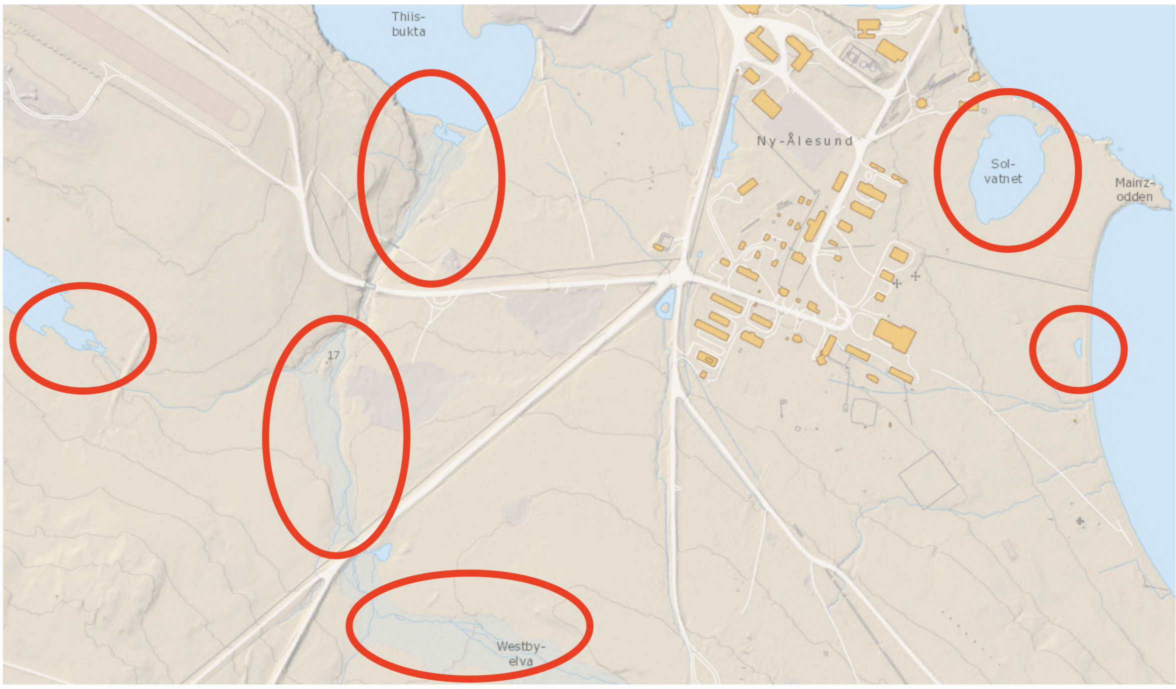

Figure 50: **Ny-Ålesund map with wind patterns.** In blue the usual (from climatology) wind patterns, while in red the ones during the ROS event.

Differences on the snow surface radiative properties are visible also on the webcam images, from Figure 41a to 41d. On the first image of March 13 in Figure 41a, the city is visible completely covered in snow, due to a snowfall during the previous night, visible looking at the snow height on the station data in Figure 23. The roads and the runway are still covered in snow, but they will be cleaned the day afterward.

On March 15, in Figure 41b, the first precipitation according to the weather station (Figure 30) was falling in form of snowflakes. From the following picture, Figure 41c, the first effects of rain can be seen. On the last bit of land on the right the Solvatnet lake (Figure 50) is visible. Previously it was completely covered by snow, but on that day the rain melted the superficial snow layer. Moreover, the snow cover on the rock on the bottom right corner decreased always due to melting.

Two days after the event, on March 18, in Figure 41d, some ice puddles are visible. Those ice puddles correspond to small water bodies, such as small lakes or rivers, marked in Figure 50. Comparing the last webcam picture with March 13, in Figure 41a, it is visible how those water bodies were previously covered with snow, that probably was lying over an ice layer. The ROS event, that brought high temperatures and rain could have melted the superficial snow layer, and then frozen it into a new layer of ice, or melted both the snow and ice, and creating a brand new layer when temperatures dropped again below zero.

Either way, the ice puddles that were previously covered with snow are now exposed to the solar radiation and, as visible from the webcam pictures, they are less reflective than snow. This clearly affects the radiative properties of the surface, reducing the overall albedo. On large scale, due to the significant presence of rivers and lakes in Svalbard, an earlier melting of snowpack could be set with more frequent ROS events.

4.5 Effects on sea ice

From the MODIS RGB images, in Figures from 37a to 37d, it is visible how the sea ice extension highly decreased in the month of March. It has to be said that March is the month when the sun starts to significantly rise above the horizon in Ny-Ålesund, after the winter twilight. This surely influences the presence of sea ice, that in fact usually completely disappears during the following months.

Anyway, winds can importantly influence the sea ice concentration also through ocean dynamics [117]. In fact, strong winds create important waves that can fragment and detach the sea ice from the shore. Once it is detached, the ice sheet can be easily transported away or being even more fragmented, as it seems to have happened during the event. Referring to 17d, it can be understood how the wind, blowing to from WSW, had a clear influence on the sea ice drifting, visible on Figure 37c, where the fragmented sea ice is evidently transported toward ENE.

From the MODIS images it can be approximated the sea ice fraction disappeared or fragmented after the event. Manually selecting the still intact or slightly fragmented sea ice to the East of Svalbard, it can be estimated that the extent decreased of about 60% between March 8 and March 25, in 17 days. Between March 11 and March 18 instead, in 7 days, the sea ice extent decreased of about 50%, suggesting that the most part of the quick decline is attribuible to the ROS event.

Chapter 5

Summary and conclusions

The cryosphere is an important component of the Earth system, as it comprehends some of the important and vulnerable regions on the globe, especially when considered the effects of climate change. Snow and ice have great contributions in many processes of the Earth system, from the energy balance to the hydrological cycle, and changes in their properties can affect on many levels both polar and mid-latitudes regions.

The Svalbard archipelago is one of the most studied Arctic regions since it host research stations from many different countries. The seasonal snowpack present approximately between October and June at Ny-Ålesund, Svalbard, is continuously monitored by an automated nivometric station at Gruvebadet, run by CNR-ISP. Furthermore, weekly snowpits are carried out to study the chemical and physical properties of the snowpack.

The climate on Svalbard is mostly arctic, characterized by low temperatures and snow precipitations during winter, with liquid precipitation starting to appear in late spring, when the air temperatures raise above zero. In the recent years, a phenomenon called Winter Warming Event, that brings above-zero temperatures during winter, is becoming more and more frequent, posing challenges to the Arctic population and ecosystem that had never been faced before. Some of these events produce a Rain on Snow (ROS) event, where liquid precipitation falls during winter over the snow cover. These events surely have many and different effects on the cryosphere and consequently on the population and the ecosystem. On the 16th March 2022 an important ROS event happened over Ny-Ålesund.

The thesis has analysed this recent ROS event studying many aspects of it. Many different kind of data were retrieved from different sources, with distinct data formats that were examined in different way with uniques programs and algorithms.

The origin of the event was located in a warm and moist air mass coming from mid-latitudes and driven by a weak polar vortex configuration. The air mass resulted to be associated with an atmospheric river that started around the Mexican Gulf and stretched, thanks to the synoptic conditions, to Svalbard, where it precipitated over the north-west portion of the archipelago, where Ny-Ålesund is located. During the event, the local orographic wind patterns have slightly changed due to the major synoptic winds.

The chemical analyses, both on the snowpack and on the air mass, suggest that the air mass was primarly composed of natural compounds, while no significant concentrations of anthropogenic compounds were found during or immediatly after the event. In particular, the concentrations seems to approximately match the ones of sea water or mineral dust, suggesting that the air mass collected the major portion of its aerosols above the North Atlantic Ocean. All the chemical compounds in the snowpack decreased their vertical integrated concentration, probably due percolation of water that carried away a significant amount of these compounds. Anyway, some have been found to have suffered more the event of others, probably due to the different solubilities in water.

The rain that fell at low altitudes, together with the high air temperatures, warmed up the whole snowpack, starting from the more superficial layers and making the bottom layers reach 0 °C too. Only many days afterwards, around March 25, the whole snowpack reached again −5 °C, the temperature it had before the event. Additionaly, snow metamorphism and snow melting made the snow height decrease approximately 15 cm, a unique decrease during the whole year. The liquid water, either precipitation or melted water, reached the bottom layers in a few hours from the first precipitations, and stayed there for about two days, before going away due to the terrain slight slope. Anyway, since the air temperature decreased below zero already starting from March 18, ice was probably created at different heights in the snowpack.

The precipitation had also effects on the radiative properties of snow, since rain affects snow grains making them bigger and therefore decreasing the reflectivity.

After the event, the sea surface temperature increased near the north-west coast of Svalbard, increasing of about 1 °C the mean temperature in the fjord in front of Ny-Ålesund. Sea ice was greatly affected mainly by strong winds and high temperatures, that disgregated most of it both at south and east of the archipelago, resulting in a 50% decrease in the days of the event.

In conclusion, this work has given a wide insight on the potential effects a ROS event can have on the cryosphere. Different datasets have been analysed and a framework to work on such events have been proposed. Future synoptic configurations that result similar to the one analysed could be carefully followed from the genesis to improve our understanding and develop a specific forecasting system for these kind of events. This would help in forecasting and preventing casualties such as the avalanche in December 2015.

The analyses of the effects on the snowpack can certainly help in understanding how the snow cover will suffer the global warming in the future. If ROS events are linked to climate change, in the next decades an increase in their frequency can be expected, that almost surely would bring to a significant decrease in the snow cover in the Arctic.

Bibliography

[1] N. Snow and I. D. Center, "Why sea ice matters." `https://nsidc.org/learn/parts-cryosphere/sea-ice/why-sea-ice-matters`.

[2] Y. Malhi, J. Franklin, N. Seddon, M. Solan, M. G. Turner, C. B. Field, and N. Knowlton, "Climate change and ecosystems: threats, opportunities and solutions," *Philosophical Transactions of the Royal Society B: Biological Sciences*, vol. 375, no. 1794, p. 20190104, 2020.

[3] S. Lee, "A theory for polar amplification from a general circulation perspective," *Asia-Pacific Journal of Atmospheric Sciences*, vol. 50, pp. 31–43, Jan 2014.

[4] M. Rantanen, A. Y. Karpechko, A. Lipponen, K. Nordling, O. Hyvärinen, K. Ruosteenoja, T. Vihma, and A. Laaksonen, "The arctic has warmed nearly four times faster than the globe since 1979," *Communications Earth & Environment*, vol. 3, p. 168, Aug 2022.

[5] S. Museum, "Svf 27624.tif: — fotoweb 8.0." `https://bildearkiv.svalbardmuseum.no/fotoweb/archives/5000-Historiske-bilder/Indekserte%20bilder/SVF%2027624.tif.info#c=%2Ffotoweb%2Farchives%2F5000-Historiske-bilder%2F`.

[6] Wikipedia contributors, "Svalbard — Wikipedia, the free encyclopedia," 2023.

[7] "Dirigibile italia." `https://www.isp.cnr.it/index.php/it/infrastrutture/stazioni-di-ricerca/stazione-artico-dirigibile-italia#:~:text=La%20stazione%2C%20inaugurata%20nel%201997,quale%20fu%20chiamata%20Dirigibile%20Italia`.

[8] Wikipedia contributors, "Köppen climate classification — Wikipedia, the free encyclopedia," 2023.

[9] Wikipedia contributors, "Tundra climate — Wikipedia, the free encyclopedia," 2023.

[10] Wikipedia contributors, "Geography of svalbard — Wikipedia, the free encyclopedia," 2022.

[11] Wikipedia contributors, "Climate of svalbard — Wikipedia, the free encyclopedia," 2023.

[12] O. Nordli, "The svalbard airport temperature series," *Bulletin of Geography, Physical Geography Series*, vol. 3, pp. 5–25, 12 2010.

[13] E. Førland, R. Benestad, I. Hanssen-Bauer, J. Haugen, and T. Engen-Skaugen, "Temperature and precipitation development at svalbard 1900–2100," *Advances in Meteorology*, vol. 2011, 01 2011.

[14] B. Earth, "Svalbard and jan mayen - berkeley earth." `http://berkeleyearth.lbl.gov/auto/Regional/TAVG/Text/svalbard-and-jan-mayen-TAVG-Trend.txt`.

[15] C. U. Press, "Arctic: Arctic climate impact assessment," tech. rep., Cambridge University Press, 2005.

[16] J.-P. Dedieu, B. Carlson, S. Bigot, P. Sirguey, V. Vionnet, and P. Choler, "On the importance of high-resolution time series of optical imagery for quantifying the effects of snow cover duration on alpine plant habitat," *Remote Sensing*, vol. 8, 06 2016.

[17] S. Karlsen, L. Stendardi, H. Tømmervik, N. Lennart, I. Arntzen, and E. Cooper, "Time-series of cloud-free sentinel-2 ndvi data used in mapping the onset of growth of central spitsbergen, svalbard," *Remote Sensing*, vol. 13, 08 2021.

[18] Wikipedia contributors, "Primary production — Wikipedia, the free encyclopedia," 2023.

[19] M. Krajewska, M. Szymczak-Żyła, W. Tylmann, and G. Kowalewska, "Climate change impact on primary production and phytoplankton taxonomy in western spitsbergen fjords based on pigments in sediments," *Global and Planetary Change*, vol. 189, p. 103158, 2020.

[20] S.-U. Kim and K.-Y. Kim, "Impact of climate change on the primary production and related biogeochemical cycles in the coastal and sea ice zone of the southern ocean," *Science of The Total Environment*, vol. 751, p. 141678, 2021.

[21] L. H. H. C. L. H. Orr E., Hansen G., "Sess report 2018, svalbard integrated arctic earth observing system, longyearbyen.," 2019.

[22] Wikipedia contributors, "Albedo — Wikipedia, the free encyclopedia," 2023.

[23] Wikipedia contributors, "Snowpack — Wikipedia, the free encyclopedia," 2023.

[24] R. L. Armstrong and E. Brun, *Snow and Climate: Physical Processes, Surface Energy Exchange and Modeling.* Cambridge University Press, 2008.

[25] G. of meteorology, "Ice crust." `https://glossary.ametsoc.org/w/index.php?title=Ice_crust&oldid=11401`.

[26] N. Polarinstitutt, "Vegetation in svalbard." `https://www.npolar.no/en/themes/vegetation-svalbard/`.

[27] I. M. Eira, G. Eira, C. Jaedicke, O. Magga, N. Maynard, D. Vikhamar-Schuler, and S. Mathiesen, "Traditional sámi snow terminology and physical snow classification—two ways of knowing," *Cold Regions Science and Technology*, vol. 85, 10 2012.

[28] I. A. of Cryospheric Sciences, "The international classification for seasonal snow on the ground," 2009.

[29] M. J. Brodzik, "The relationship of snow water equivalent to snow depth and density." `http://cires1.colorado.edu/~brodzik/depth_to_swe.pdf`.

[30] C. Fierz, *Temperature Profile of Snowpack*, pp. 1151–1154. Dordrecht: Springer Netherlands, 2011.

[31] X. Wang, W. Pu, X. Zhang, Y. Ren, and J. Huang, "Water-soluble ions and trace elements in surface snow and their potential source regions across northeastern china," *Atmospheric Environment*, vol. 114, pp. 57–65, 2015.

[32] A. Kashki and J. Khoshhal, "Investigation of the role of polar vortex in iranian first and last snowfalls," *Journal of Geography and Geology*, vol. 5, 10 2013.

[33] P. Arias, N. Bellouin, E. Coppola, R. Jones, G. Krinner, J. Marotzke, V. Naik, M. Palmer, G.-K. Plattner, J. Rogelj, M. Rojas, J. Sillmann, T. Storelvmo, P. Thorne, B. Trewin, K. Achuta Rao, B. Adhikary, R. Allan, K. Armour, G. Bala, R. Barimalala, S. Berger, J. Canadell, C. Cassou, A. Cherchi, W. Collins, W. Collins, S. Connors, S. Corti, F. Cruz, F. Dentener, C. Dereczynski, A. Di Luca, A. Diongue Niang, F. Doblas-Reyes, A. Dosio, H. Douville, F. Engelbrecht, V. Eyring, E. Fischer, P. Forster, B. Fox-Kemper, J. Fuglestvedt, J. Fyfe, N. Gillett, L. Goldfarb, I. Gorodetskaya, J. Gutierrez, R. Hamdi, E. Hawkins, H. Hewitt, P. Hope, A. Islam, C. Jones, D. Kaufman, R. Kopp, Y. Kosaka, J. Kossin, S. Krakovska, J.-Y. Lee, J. Li, T. Mauritsen, T. Maycock, M. Meinshausen, S.-K. Min, P. Monteiro, T. Ngo-Duc, F. Otto, I. Pinto, A. Pirani, K. Raghavan, R. Ranasinghe, A. Ruane, L. Ruiz, J.-B. Sallée, B. Samset, S. Sathyendranath, S. Seneviratne, A. Sörensson, S. Szopa, I. Takayabu, A.-M. Tréguier, B. van den Hurk, R. Vautard, K. von Schuckmann, S. Zaehle, X. Zhang, and K. Zickfeld, *Climate Change 2021: The Physical Science Basis. Contribution of Working Group I to the Sixth Assessment Report of the Intergovernmental Panel on Climate Change.*

[34] J. A. Francis and S. J. Vavrus, "Evidence for a wavier jet stream in response to rapid arctic warming," *Environmental Research Letters*, vol. 10, p. 014005, jan 2015.

[35] W. Janach, "The physics of jet stream meandering," *Advances in Systems Science and Applications*, vol. 15, 09 2015.

[36] M. P. Baldwin and D. W. Thompson, “A critical comparison of stratosphere–troposphere coupling indices,” *Quarterly Journal of the Royal Meteorological Society*, vol. 135, no. 644, pp. 1661–1672, 2009.

[37] S. H. Lee, J. C. Furtado, and A. J. Charlton-Perez, “Wintertime north american weather regimes and the arctic stratospheric polar vortex,” *Geophysical Research Letters*, vol. 46, no. 24, pp. 14892–14900, 2019.

[38] C. Cassou, “Euro-atlantic regimes and their teleconnections,” 2010 2010.

[39] G. Heinemann and C. Claud, “Report of a workshop on theoretical and observational studies of polar lows” of the european geophysical society polar lows working group,” *Bulletin of the American Meteorological Society*, vol. 78, no. 11, pp. 2643 – 2658, 1997.

[40] M. Moreno-Ibáñez, R. Laprise, and P. Gachon, “Recent advances in polar low research: current knowledge, challenges and future perspectives,” *Tellus A: Dynamic Meteorology and Oceanography*, vol. 73, no. 1, pp. 1–31, 2021.

[41] C. S. Martin Indreiten, “The longyearbyen fatal avalanche accident 19th december 2015, svalbard - lessons learned from avalanche rescue inside a settlement,” 2016.

[42] S. Wickström, M. O. Jonassen, T. Vihma, and P. Uotila, “Trends in cyclones in the high-latitude north atlantic during 1979–2016,” *Quarterly Journal of the Royal Meteorological Society*, vol. 146, no. 727, pp. 762–779, 2020.

[43] P.-E. Mallet, C. Claud, C. Cassou, G. Noer, and K. Kodera, “Polar lows over the nordic and labrador seas: Synoptic circulation patterns and associations with north atlantic-europe wintertime weather regimes,” *Journal of Geophysical Research: Atmospheres*, vol. 118, no. 6, pp. 2455–2472, 2013.

[44] P. Chylek, C. K. Folland, G. Lesins, M. K. Dubey, and M. Wang, “Arctic air temperature change amplification and the atlantic multidecadal oscillation,” *Geophysical Research Letters*, vol. 36, no. 14, 2009.

[45] H. Jeong, H.-S. Park, M. F. Stuecker, and S.-W. Yeh, “Distinct impacts of major el nino events on arctic temperatures due to differences in eastern tropical pacific sea surface temperatures,” *Science Advances*, vol. 8, no. 4, p. eabl8278, 2022.

[46] S. o. California, “25 years after deadly 1997 new year’s floods, here’s how california is more prepared.” `https://water.ca.gov/News/Blog/2022/January/1997-New-Years-Floods`.

[47] Wikipedia contributors, “Atmospheric river — Wikipedia, the free encyclopedia,” 2023.

[48] L. Li, F. Cannon, M. R. Mazloff, A. C. Subramanian, A. M. Wilson, and F. M. Ralph, "Impact of atmospheric rivers on arctic sea ice variations," *EGUsphere*, vol. 2022, pp. 1–21, 2022.

[49] C. Viceto, I. V. Gorodetskaya, A. Rinke, M. Maturilli, A. Rocha, and S. Crewell, "Atmospheric rivers and associated precipitation patterns during the acloud and pascal campaigns near svalbard (may–june 2017): case studies using observations, reanalyses, and a regional climate model," *Atmospheric Chemistry and Physics*, vol. 22, no. 1, pp. 441–463, 2022.

[50] B. B. Hansen, K. Isaksen, R. E. Benestad, J. Kohler, Åshild Ø Pedersen, L. E. Loe, S. J. Coulson, J. O. Larsen, and Øystein Varpe, "Warmer and wetter winters: characteristics and implications of an extreme weather event in the high arctic," *Environmental Research Letters*, vol. 9, p. 114021, nov 2014.

[51] D. Pascual and M. Johansson, "Increasing impacts of extreme winter warming events on permafrost," *Weather and Climate Extremes*, vol. 36, p. 100450, 2022.

[52] D. Vikhamar-Schuler, K. Isaksen, J. E. Haugen, H. Tømmervik, B. Luks, T. V. Schuler, and J. W. Bjerke, "Changes in winter warming events in the nordic arctic region," *Journal of Climate*, vol. 29, no. 17, pp. 6223 – 6244, 2016.

[53] G. W. K. Moore, "The december 2015 north pole warming event and the increasing occurrence of such events," *Scientific Reports*, vol. 6, no. 1, p. 39084, 2016.

[54] A. Dobler, J. Lutz, O. Landgren, and J. E. Haugen, "Circulation specific precipitation patterns over svalbard and projected future changes," *Atmosphere*, vol. 11, p. 1378, Dec 2020.

[55] M. Müller, T. Kelder, and C. Palerme, "Decline of sea-ice in the greenland sea intensifies extreme precipitation over svalbard," *Weather and Climate Extremes*, vol. 36, p. 100437, 2022.

[56] "Gruvebadet cnr laboratory." `https://www.isp.cnr.it/index.php/it/infrastrutture/osservatori/gruvebadet`.

[57] F. Scoto, G. Pappaccogli, M. Mazzola, A. Donateo, R. Salzano, M. Monzali, F. de Blasi, C. Larose, J.-C. Gallet, S. Decesari, and A. Spolaor, "Automated observation of physical snowpack properties in ny-Ålesund," *Frontiers in Earth Science*, vol. 11, 2023.

[58] M. Tiuri, A. Sihvola, E. Nyfors, and M. Hallikaiken, "The complex dielectric constant of snow at microwave frequencies," *IEEE Journal of Oceanic Engineering*, vol. 9, no. 5, pp. 377–382, 1984.

[59] Sensorex, "Understanding the resistivity of water." `https://sensorex.com/2020/12/29/resistivity-of-water/`, May 2022.

[60] Wikipedia contributors, “Ion chromatography — Wikipedia, the free encyclopedia,” 2023.

[61] O. C. R. Program, “Ion chromatography.” `https://research.cbc.osu.edu/reel/research-modules/environmental-chemistry/instrumentation/instrument-calibration/ion-chromatography-theory/#:~:text=Ion%20Chromatography%20is%20a%20method,cation%20column%2C%20which%20attracts%20cations`.

[62] “Climate reanalysis.” `https://climate.copernicus.eu/climate-reanalysis`.

[63] “Climate data guide.” `https://climatedataguide.ucar.edu/climate-data/era-15`, Jan 1979.

[64] H. Setchell, “Ecmwf reanalysis - 40 years.” `https://www.ecmwf.int/en/forecasts/dataset/ecmwf-reanalysis-40-years`, Nov 2022.

[65] J. A. P. Leon, “Use of era5 reanalysis to initialise re-forecasts proves beneficial.” `https://www.ecmwf.int/en/newsletter/161/meteorology/use-era5-reanalysis-initialise-re-forecasts-proves-beneficial`, Nov 2022.

[66] A. Guillory, “Era5.” `https://www.ecmwf.int/en/forecasts/datasets/reanalysis-datasets/era5`, Aug 2022.

[67] B. Guan and D. E. Waliser, “Detection of atmospheric rivers: Evaluation and application of an algorithm for global studies,” *Journal of Geophysical Research: Atmospheres*, vol. 120, no. 24, pp. 12514–12535, 2015.

[68] Ecmwf, “Copernicus arctic regional reanalysis (carra): Added value to the era5 global reanalysis.” `https://confluence.ecmwf.int/display/CKB/Copernicus+Arctic+Regional+Reanalysis+%28CARRA%29%3A+Added+value+to+the+ERA5+global+reanalysis`.

[69] Copernicus, “Carra reanalysis.” `https://climate.copernicus.eu/copernicus-arctic-regional-reanalysis-service`.

[70] “Hysplit model informations.” `https://www.arl.noaa.gov/hysplit/`.

[71] M. Maturilli, “Ceilometer cloud base height from station Ny-Ålesund (2017-08 et seq),” 2022.

[72] Vaisala, “Cv-51 technical sheet.” `https://www.eurelettronicaicas.com/files/prodotti/cl51-datasheet-b210861en.pdf`.

[73] N. Klimaservicesenter, “Norsk klimaservicesenter website.” `https://seklima.met.no/`.

[74] R. Neuber, J. Ström, and C. Hübner, “Atmospheric research in ny-Ålesund – a flagship programme,” 03 2011.

[75] F. Technologies, “Ft702lm technical sheet.” `https://fttechnologies.com/wp-content/uploads/2018/10/FT702LM-Data-Sheet.pdf`.

[76] C. Scientific, “Hmp45c technical sheet.” `https://s.campbellsci.com/documents/af/manuals/hmp45c.pdf`.

[77] K. Ebell, S. Schnitt, and P. Krobot, “Precipitation amount of Pluvio rain gauge at AWIPEV, Ny-Ålesund (2019),” PANGAEA, 2023. In: Ebell, K et al. (2023): Precipitation amount of Pluvio rain gauge at AWIPEV, Ny-Ålesund (2017-2021). PANGAEA, https://doi.pangaea.de/10.1594/PANGAEA.957612 (DOI registration in progress).

[78] Vaisala, “Ott pluvio2 400 technical sheet.” `https://www.otthydromet.com/en/p-ott-pluvio-l-400-rh-weighing-rain-gauge-400-cm750-mm-heated-rim/70.040.021.9.0`.

[79] “Climate change tower data portal.” `https://metadata.iadc.cnr.it/geonetwork/srv/api/records/e4872959-4cf2-48df-8195-e8065411be49`.

[80] CNR, “Climate change tower integrated project.” `https://bo.isp.cnr.it/main/CCTower/`.

[81] A. G. A. G. Experiment, “Advanced global atmospheric gases experiment - zeppelin, ny-Ålesund.” `https://agage.mit.edu/stations/zeppelin-ny-%C3%A5lesund`.

[82] Wikipedia contributors, “Zeppelin observatoriet — Wikipedia, den frie encyklopedi,” 2021.

[83] C. Pedersen, “Zeppelin webcamera time series,” 2013.

[84] NASA, “Modis about webpage.” `https://modis.gsfc.nasa.gov/about/`.

[85] W. J. J. van Pelt, J. Oerlemans, C. H. Reijmer, V. A. Pohjola, R. Pettersson, and J. H. van Angelen, “Simulating melt, runoff and refreezing on nordenskiöldbreen, svalbard, using a coupled snow and energy balance model,” *The Cryosphere*, vol. 6, no. 3, pp. 641–659, 2012.

[86] W. van Pelt, V. Pohjola, R. Pettersson, S. Marchenko, J. Kohler, B. Luks, J. O. Hagen, T. V. Schuler, T. Dunse, B. Noël, and C. Reijmer, “A long-term dataset of climatic mass balance, snow conditions, and runoff in svalbard (1957–2018),” *The Cryosphere*, vol. 13, no. 9, pp. 2259–2280, 2019.

[87] W. Greuell and T. Konzelmann, “Numerical modelling of the energy balance and the englacial temperature of the greenland ice sheet. calculations for the eth-camp location (west greenland, 1155 m a.s.l.),” *Global and Planetary Change*, vol. 9, no. 1, pp. 91–114, 1994. Greenland ice margin experiment (GIMEx).

[88] “Nora reanalysis.” `https://marine.met.no/node/19`, journal=MET Norway, author=MET Norway - Oseanografi og Maritim Meteorologi.

[89] N. M. Library and Archive, “Water in the atmosphere.” `https://web.archive.org/web/20120114162401/http://www.metoffice.gov.uk/media/pdf/4/1/No._03_-_Water_in_the_Atmosphere.pdf`.

[90] N. W. Service, “Beaufort wind scale.” `https://www.weather.gov/mfl/beaufort#:~:text=One%20of%20the%20first%20scales,to%20a%20force%20of%2012.f`.

[91] S. H., Y. X., K. M. A. O., A. B., B. A., B. E., B. J., B. J. E., D. P., H. S., H. M., H. A., H. J., J. A., K. M. A., K. H., L. M. P., L. M., M. T., N. E. P., N. K. P., O. E., P. B., P. A. C., R. R., S. P., S. R., S. E., T. S., V. T., and W. Z. Q., “Arctic regional reanalysis on single levels from 1991 to present,” *Copernicus Climate Change Service (C3S) Climate Data Store (CDS).*

[92] N. Oceanic and A. Administration, “What is an atmospheric river?.” `https://scijinks.gov/atmospheric-river/`.

[93] S. N. Behera, M. Sharma, V. P. Aneja, and R. Balasubramanian, “Ammonia in the atmosphere: a review on emission sources, atmospheric chemistry and deposition on terrestrial bodies,” *Environ. Sci. Pollut. Res. Int.*, vol. 20, pp. 8092–8131, Nov. 2013.

[94] A. Ooki, M. Uematsu, K. Miura, and S. Nakae, “Sources of sodium in atmospheric fine particles,” *Atmospheric Environment*, vol. 36, no. 27, pp. 4367–4374, 2002.

[95] H. Wang and Q. Zhang, “Research advances in identifying sulfate contamination sources of water environment by using stable isotopes,” *Int. J. Environ. Res. Public Health*, vol. 16, p. 1914, May 2019.

[96] “So2 sources.” `https://www.epa.gov/so2-pollution/sulfur-dioxide-basics`.

[97] “Calcium sources.” `https://naei.beis.gov.uk/overview/pollutants?pollutant_id=84`.

[98] X. Wang, D. J. Jacob, S. D. Eastham, M. P. Sulprizio, L. Zhu, Q. Chen, B. Alexander, T. Sherwen, M. J. Evans, B. H. Lee, J. D. Haskins, F. D. Lopez-Hilfiker, J. A. Thornton, G. L. Huey, and H. Liao, “The role of chlorine in global tropospheric chemistry,” *Atmospheric Chemistry and Physics*, vol. 19, no. 6, pp. 3981–4003, 2019.

[99] “Magnesium sources.” `https://naei.beis.gov.uk/overview/pollutants?pollutant_id=117`.

[100] "No3 sources." `http://ecosystems.mbl.edu/Research/Clue/air.html#:~:text=Atmospheric%20N2%20is%20converted,the%20atmosphere%20during%20plant%20decay`.

[101] J. Yu, C. Yan, Y. Liu, X. Li, T. Zhou, and M. Zheng, "Potassium: A tracer for biomass burning in beijing?," *Aerosol and Air Quality Research*, vol. 18, no. 9, pp. 2447–2459, 2018.

[102] S. C. Wofsy, M. B. McElroy, and Y. L. Yung, "The chemistry of atmospheric bromine," *Geophysical Research Letters*, vol. 2, no. 6, pp. 215–218, 1975.

[103] E. Sanhueza and M. O. Andreae, "Emission of formic and acetic acids from tropical savanna soils," *Geophysical Research Letters*, vol. 18, no. 9, pp. 1707–1710, 1991.

[104] H. Zhang, O. Kupiainen-Määttä, X. Zhang, V. Molinero, Y. Zhang, and Z. Li, "The enhancement mechanism of glycolic acid on the formation of atmospheric sulfuric acid–ammonia molecular clusters," *The Journal of Chemical Physics*, vol. 146, 05 2017. 184308.

[105] P. K. Martinelango, P. K. Dasgupta, and R. S. Al-Horr, "Atmospheric production of oxalic acid/oxalate and nitric acid/nitrate in the tampa bay airshed: Parallel pathways," *Atmospheric Environment*, vol. 41, no. 20, pp. 4258–4269, 2007. (BRACE).

[106] S. Becagli, A. Amore, L. Caiazzo, T. D. Iorio, A. d. Sarra, L. Lazzara, C. Marchese, D. Meloni, G. Mori, G. Muscari, C. Nuccio, G. Pace, M. Severi, and R. Traversi, "Biogenic aerosol in the arctic from eight years of msa data from ny Ålesund (svalbard islands) and thule (greenland)," *Atmosphere*, vol. 10, no. 7, 2019.

[107] F. T. Mackenzie, A. C. Duxbury, and R. H. Byrne, *seawater*. Apr. 2023.

[108] A. Spolaor, C. Varin, X. Pedeli, J.-M. Christille, T. Kirchgeorg, F. Giardi, D. Cappelletti, C. Turetta, W. Cairns, A. Gambaro, A. Bernagozzi, J. Gallet, M. Björkman, and E. Barbaro, "Source, timing and dynamics of ionic species mobility in the svalbard annual snowpack," *Science of The Total Environment*, vol. 751, p. 141640, 08 2020.

[109] T. K. K., "Oceans," *Prentice-Hall*, 1968.

[110] D. M. Murphy, D. S. Thomson, and A. M. Middlebrook, "Bromine, iodine, and chlorine in single aerosol particles at cape grim," *Geophysical Research Letters*, vol. 24, no. 24, pp. 3197–3200, 1997.

[111] M. Maturilli, A. Herber, and G. König-Langlo, "Climatology and time series of surface meteorology in ny-Ålesund, svalbard," *Earth System Science Data*, vol. 5, no. 1, pp. 155–163, 2013.

[112] A. A. Kokhanovsky, “Light penetration in snow layers,” *Journal of Quantitative Spectroscopy and Radiative Transfer*, vol. 278, p. 108040, 2022.

[113] T. Ozeki and E. Akitaya, “Energy balance and formation of sun crust in snow,” *Annals of Glaciology*, vol. 26, p. 35–38, 1998.

[114] T. Yamanouchi, “Arctic warming by cloud radiation enhanced by moist air intrusion observed at ny-Ålesund, svalbard,” *Polar Science*, vol. 21, pp. 110–116, 2019. ISAR-5/ Fifth International Symposium on Arctic Research.

[115] S. Colbeck, “Grain clusters in wet snow,” *Journal of Colloid and Interface Science*, vol. 72, no. 3, pp. 371–384, 1979.

[116] W. J. Wiscombe and S. G. Warren, “A model for the spectral albedo of snow. i: Pure snow,” *Journal of Atmospheric Sciences*, vol. 37, no. 12, pp. 2712 – 2733, 1980.

[117] A. R, K. N, V. S, D. T, F. JA, S. J, F. G, V. T, and C. A, “Wind amplifies the polar sea ice retreat,” *ENVIRONMENTAL RESEARCH LETTERS*, vol. 15, no. 12, p. 124022, 2020.